

Probing Time-Dependent Electron Interactions in Double-Rydberg Wave packets

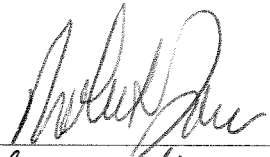
Xiangdong Zhang
Handan, Hebei, China

B.S. Hebei University, May 1999
M.S. Shanghai Institute of Optics and Fine Mechanics, May 2002

A Dissertation presented to the Graduate Faculty
of the University of Virginia in Candidacy for the Degree of
Doctor of Philosophy

Department of Physics

University of Virginia
May 2008



Xiangdong Zhang

Thomas F. Gallagher

Richard N. Zare

Abstract

This dissertation has described a series of experiments leading to the first direct measurement of time-dependent energy exchange in double Rydberg wave packets (DRWs). Several preliminary experiments paved the way for the primary measurements. The first experiment characterized the field dependence of HCP ionization of ionic Rydberg states. The HCP ionization probability of $Ba^+ ng^+$ ions and Ba $6snd$ Rydberg states with approximately the same binding energies were compared and found to be essentially identical within experiment noise, which reasonably agrees with the prediction of impulsive ionization model and classical trajectory Monte-Carlo (CTMC) simulation. The second experiment explored the time-dependent evolution of Rydberg ion wave packets via HCP ionization and a method for determining the quantum states of these wave packets was demonstrated. Finally, HCP aided double ionization was used as a probe of time-dependent energy exchange in DRWs both in the laboratory and in numerical CTMC simulations. Experimentally, energy exchange between the two wave packets is observed almost at the instant of the excitation ionic wave packets. However, the rate at which autoionization occurs depends on the relative initial positions and velocities of the two wave packets. Following autoionization, the evolution of remaining “ionic” wave packet is reflected in modulations in the HCP aided double ionization yield. This feature is more visible in the CTMC simulations than in the experimental results.

Contents

1	Introduction	1
1.1	Introduction	1
1.2	Two-electron atoms	1
1.3	Rydberg atoms	5
1.4	Wave packets	6
1.5	Structure of Dissertation	8
2	Experimental Apparatus	9
2.1	Introduction	9
2.2	Femtosecond Ti:sapphire laser system	9
2.2.1	Oscillator	11
2.2.2	Stretcher and compressor	12
2.2.3	Regenerative and multipass amplifier	14
2.2.4	Single shot autocorrelator	17
2.3	Optical parametric amplifier	19
2.4	Dye lasers	20
2.5	Atom source, vacuum system and detector	23
2.5.1	Atom source	23
2.5.2	Vacuum system	24
2.5.3	Detection and data acquisition	24
3	Half-Cycle Pulse Ionization of Ba⁺ Rydberg Ions	26
3.1	Introduction	26
3.2	Half cycle pulses	27
3.3	HCP Ionization of Ba ⁺ Rydberg Ions	28
3.3.1	Experimental procedure	30
3.3.2	Results and discussion	33
	Impulsive ionization	33
	Experimental results	35
	Discussion	38
3.4	Summary	40

4	Measurement of the Quantum State of Ionic Wave Packets using HCP	42
4.1	Introduction	42
4.2	Experimental procedure	43
4.3	Results and discussion	44
4.3.1	Complex phase-retrieval method	48
4.4	Summary	53
5	Time-Resolved Energy Exchange Between Electrons in Double Rydberg Wave Packets	55
5.1	Introduction	55
5.2	Experimental procedure	57
5.3	Results and discussion	62
5.3.1	Characterization of $5dnd$ autoionizing wave packets	62
	Two channel quantum defect theory calculation	66
5.3.2	Doubly excited Rydberg wave packets	68
5.3.3	Classical simulation	77
	Initial conditions	80
	Simulation results	85
5.4	Summary	95
6	Conclusion	98
6.1	HCP ionization of ionic Rydberg states	98
6.2	Ionic Rydberg wave packets	99
6.3	Time-dependent energy exchange of DRW	99
6.4	Future directions	100
A	Runge-lenz vector	103

List of Tables

1.1	Some properties of Rydberg atoms	6
3.1	Measured:predicted impulse ratios for ionization of ng^+ Rydberg ions with 20% and 50% probability.	39

List of Figures

2.1	Schematic scheme of chirped pulse amplification [20]	10
2.2	Basic layout of Oscillator [22].	12
2.3	Schematic diagram of Stretcher. RM1 and RM2 are retroreflection mirrors, which diffract light off grating four times.	13
2.4	Schematic setup of compressor [26].	14
2.5	Regenerative amplifier [27].	16
2.6	Multipass amplifier [29].	16
2.7	Schematic of optical isolation between the oscillator and amplifiers.	17
2.8	The single shot autocorrelator [27].	18
2.9	Optical parametric amplifier setup diagram.	21
2.10	Hansch style dye laser	22
2.11	Littman style dye laser	22
2.12	Top view of the schematic diagram of the vacuum chamber.	25
3.1	Diagram of HCP generation [53]. An ultrashort laser pulse promotes the electrons of biased wafer from valance band to conduction band. The carriers accelerate under the biased field creating the Terahertz radiation. The incident angle of the laser θ_0 is adjusted close to 90° in the experiment.	29
3.2	Schematic electric field strength of HCP as a function of time generated from photoconductive emitters with ultrashort pulses. [34,55]	29
3.3	The diagram of experimental set up.	31
3.4	Excitation scheme for both 6snd neutral Rydberg states and ng^+ ionic Rydberg states.	32
3.5	Measured HCP ionization probability as a function of GaAs biasfield (bottom scale) and impulse (top scale) for $6s30d$ (green), $6s33d$ (red), and $6s36d$ (black) initial states.	36
3.6	Comparison of measured HCP ionization probability vs. GaAs bias field curves for pairs of neutral (dashed lines) and ionic (solid lines) Rydberg states that have approximately the same binding energy.	37
4.1	Laser excitation scheme for producing an ionic ng^+ Rydberg wave packet.	43

4.2	Double ionization signal as a function of delay between HCP probe and the laser excitation of an ionic wave packet with an average principal quantum number, $n \sim 38$. The ionization probability here is $< 50\%$	45
4.3	A schematic diagram of fraction of wave packet is ionized [56].	46
4.4	Double ionization signal of ionic wave packet for different HCP strengths.	47
4.5	Discrete Fourier Transform of data shown in Fig.4.2.	50
4.6	Discrete Fourier Transform of data shown.	51
4.7	Measured amplitudes and phases of constituent eigenstates in a ng^+ ionic radial wave packet in Barium for low HCP strength(blue cross) and high HCP strength(red circle).	52
4.8	Density plots of recovered time-dependent probability distribution for the ng^+ ionic wave packet described by Fig.4.7 in both coordinate and momentum space. Dark denotes high probability regions.	54
5.1	Schematic of the experimental setup and the time sequence of laser excitations, HCP, and field ionization pulse. All the laser pulses and HCP are pointed from the same side. The angle between the HCP and the excitation lasers is $\sim 40^\circ$. The 2mm diameter extraction hole and the angle results in a time resolution, ~ 0.8 psec for the experiments. This is comparable the the duration of HCP or the excitation lasers. Therefore, the time resolution of the experiment is ~ 1 psec. The time t_1 between L2 and L3+L4, is adjusted to control the relative phase of the wave packets. A field pulse with a $50ns$ rise time pushes single/double charged ions into the detector several 10's of nanoseconds after the lasers and HCP.	58
5.2	Laser excitation scheme of double Rydberg wave packets. The related ionic states are plotted side by side. The green curved arrows show the possible autoionization paths from double excited states to nearby ionic states or continua.	59
5.3	Survival probability of $5d25d$ autoionizing wave packet.	65
5.4	Double ionization signals for two different delays between two wave packets excitation.	69
5.5	Schematic diagram of HCP energy transfer with respect to the double and field ionization limits.	70
5.6	The normalized double ionization signal of $38g25d$ wave packets by scanning HCPs	72
5.7	The normalized double ionization signal of $38g23d$ wave packets by scanning HCPs	73
5.8	The normalized double ionization background signal after of $38g23d$ wave packet.	75

5.9	Schematic diagram of initial condition of two electrons. Two cones indicate the possible angular momentum vectors L_1 and L_2 with total $M_z = 0$	79
5.10	The angular momentum distribution of final ionic states after autoionization for $38g25d$ wave packets with the time delay between two electronic wave packets from 0.1 psec to 2.9 psec in absence of HCP. . .	84
5.11	Simulated trajectories of two electrons with a neutral wave packet, $n = 25$, and the ionic wave packet, $N = 38$. The right column is the radial distance of the “ionic” electron as a function of time with respect to the excitation of the neutral wave packets. Analogous plots for the first electron are shown on the left. From top to bottom, the time delay between the excitation of the two electronic wave packets decreases from $1.3 \tau_1$ to 0 psec with a step size of $0.25 \tau_1$. The maximum radial distance is 5000 a.u for each plot. Darker regions indicate overlapping trajectories and, therefore, higher probability.	86
5.12	Simulated trajectories of two electrons simulation with a neutral wave packet, $n = 23$, and the ionic wave packet, $N = 38$. The right column is the radial distance of the “ionic” electron as a function of time with respect the excitation of the neutral wave packets. Analogous plots for the first electron are shown on the left. From top to bottom, the time delay between the excitation of the two electronic wave packets decreases from $1.7\tau_1$ to 0 with a step size of $0.3\tau_1$. The maximum radial distance is 5000 a.u for each plot. Darker regions indicate the overlapping trajectories and, therefore, higher probability.	87
5.13	Simulated final ionic state distribution following autoionization of the $38g25d$ and $38g23d$ wave packet configurations without HCP. The warmer color denotes higher probability. The dark line indicates the ionization threshold determined by the 2400V/cm clearing pulse (assuming diabatic field ionization [15]). The x-axis is the time delay between the excitation of the two wave packets in units of the Kepler period, τ_1 , of first wave packet.	90

5.14	Time-dependent variation σ_{ee} (left plot in each pair) and the expectation values of radial position of two electrons (right plot in each pair) as a function time for 38g25d(a)(b) and 38g23d(c)(d), where $\sigma_{ee} = \sqrt{\frac{\sum_N (V_{ee}^2 - 1/r_0^2)}{N}}$. Each curve corresponds to the specific launch time of HCP indicated by vertical dash line. The y axis varies from 0 to 400 cm^{-1} for each left plot. The radial distance varies from 0 to 15000 a.u. for each right plot. The vertical line indicates the instant that the double Rydberg wave packets are exposed to the HCP. In the radial position plots, the blue solid line is for the outer electron which sees a $-1/r$ potential, and the black dashed line is for the inner electron which experiences a $-2/r$ potential.	92
5.15	Density plots for unnormalized (a,c) and normalized (b,d) HCP double ionization probability of 38g25d and 38g23d wave packets from classical simulation. Zero delay corresponds to the excitation of the first wave packet.	94
5.16	The calculated normalized double ionization signal of $Ngnd$ double Rydberg wave packets, where $n \sim 25$ and $N \sim 38$, as a function of delay t_2 with respect to the ionic wave packet excitation. Each data set corresponds to a different time delay, t_1 , in terms of the Kepler period of the first wave packet. The simulated data are integrated over (230 fsec) time bins as in the experiment.	96
A.1	Schematic diagram of Runge-Lenz vector at four different points on a ellipse orbit(Adapted from Ref. [78]).	104

Acknowledgments

I am indebt with many people during the course for finishing my doctoral degree when I sit back to look through these years.

The first thanks should goes to Professor Robert Jones, who give me the opportunities working in the ultrafast laser and atomic physics lab. The experiments described in this thesis are the most difficult task I met. I can not finish this work without Professor Jones helping the survival techniques in the lab, guiding me through analyzing the data and pushing me moving forward.

Thanks are also need to given to my lab mates, Dr. Thibault Vogt, Dr. Jeremy Murray-Krezan, Dr. Lung Ko, Mary Kutteruf, Dan Pinkham, Brett Sickmiller. I have to mention that Jeremy's valuable tips varying from setting up Dye lasers, working with the "magic" Half-cycle pulse and inviting my wife and me over his house for holidays. It is great pleasure to have Dr. Thibault around in my last year, who give me valuable discussions not only on physics problem, but also on different cultures.

I have to bring up my friends to thank them accompanying with me more than five years in UVA. Xiaodong Zhang, Wei Jiang, Yaogang Lian, Zhibin Lin, Xiaoruo Xie and Songba Ye shared their time with me for party, hiking and fighting the homework in the first two years.

Thanks should be addressed to faculties and staffs of department. Professor Gal-

lagher and his students, Professor Pfister, Professor Sackett etc bring me the support both in the research and in the courses. Chris, Tammie, Suzie . . . , in Physics department who provide such a nice support system in department for me to be able to finish graduate study.

Last, I give my appreciation to my family. My parents are very supportive and encourage me in my very steps in my life. It is great gift to have my wife, Jianing, around while I am trying finish the degree. Her academical inspiration and encouragement are always beside me when I need them to go through the most difficult time in my life.



Dedicated to my wife Jianing.

Chapter 1

Introduction

1.1 Introduction

Ever since 1803 when chemist John Dalton proposed that everything is composed of many small pieces, called atoms, the effort to understand atoms has been one of the driving forces of physics. Current research in atomic physics focuses on isolated atomic systems or on groups of atoms. Studies of atoms with two valence electrons are an active research area because not only can it provide a more complete understanding of the relationship between quantum and classical descriptions of physical phenomena at a basic level, but also it can benefit research of more complex quantum systems, such as molecules, multielectron systems.

1.2 Two-electron atoms

The hydrogen atom, the simplest element, can be solved analytically in both quantum and classical theories. An additional electron makes Helium, the simplest two-electron atom, a complex three-body system, which has no known general solution

in either classical or quantum theory [1]. The complexities of such relatively simple multielectron system stem mainly from the correlation between two electrons, $\frac{1}{r_{12}}$ in the Hamiltonian of Helium

$$H = \frac{\vec{p}_1^2}{2} - \frac{2}{r_1} + \frac{\vec{p}_2^2}{2} - \frac{2}{r_2} + \frac{1}{r_{12}}, \quad (1.1)$$

where \vec{r}_1 and \vec{r}_2 are the positions of the first and second electrons from the nucleus, $r_{12} = |\vec{r}_1 - \vec{r}_2|$ is the mutual separation between two electrons; and \vec{p}_1 and \vec{p}_2 represent the momentum of each electron. Atomic units are used here and throughout this dissertation unless otherwise specified. In this dissertation, two-electron atoms refer to atoms that have two valence electrons, particularly alkaline-earth atoms.

In the classical picture, there are numerous possibilities of two electrons moving in different directions and speeds after they collide with each other. Depending on the initial configuration of two electrons, the motion of two electrons can show periodical features [2, 4, 5] or is chaotic. In quantum mechanics, the correlation between two electrons makes the Schrodinger equation unseparable. Therefore, the spectrum of Helium, the simplest two-electron atom, becomes much more complex than Hydrogen because of this strong correlation between the two electrons. The spectrum is particularly complicated while approaching the classical double ionization limit. This results in the complicated dynamics of such a 3-body system [1]. Reference [1] gives nice review on the theoretical and experimental investigation on the two-electron atoms. It is worth highlighting the discovery of the electron correlation in Helium spectrum by Madden and Codling [6], which brought people's attention on the correlated two-electron dynamics.

In the case that one electron is in the ground state or low excited state and the other electron is in a highly excited state, the two-electron atom system resembles

Hydrogen due to the large separation of the two electrons. A number of experiments have been carried out to investigate the two-electron system with such configuration in various aspects by frequency spectroscopy, including electron-electron correlation on the principle quantum number of excited states of electrons and the angular momentum of the Rydberg electron, relative electron positions, and core polarization effect of the inner electron [7, 8]. The perturbation of the time evolution of a Rydberg electronic wave packet due to the correlation between two electrons was also investigated [10]. The multichannel quantum defect theory (MQDT) [9] was applied to help the understanding of two-electron problem together with experimental data. Other perturbation theories [1] were developed to gain insights of this problem, because the mutual repulsive force between the two electrons can be considered as the perturbation in this case.

The radial extend of the outer Rydberg electron is much larger than the other valence electron in the above case, however, the radial extends of two electrons are comparable in the configurations that two electrons are in the ground state or are both in highly excited states. The study of electronic dynamics in the former case is one of purposes of the frontier attosecond research. In the later case, two-electron systems can only exist a short time because their total energy is greater than the ionization limit of atoms where one electron goes into lower bound state by releasing a free electron. This is called “autoionization”. The more highly excited are two Rydberg electrons approaching the double ionization limit, the higher the density of eigenstates is. Therefore, the usage of the frequency spectroscopy is prevented in this regime [49]. This leaves research opportunities available in this regime, particularly under the double ionization limit. Recent advances in ultrashort laser, electro-optic technology and the controllable wave packet [11] provide a playground to study the

time-dependent properties of the two-electron problems near the double ionization limit. An apparent benefit is that the study of double Rydberg atoms provides a similar system to attosecond research [16] on a large time scale [12]. The analogy between the configuration interactions of the two-electron system and the coupling of different modes in molecules enable the possible carrying over the techniques and understanding of the two-electron system to molecular systems [13]. Furthermore, because the experiments are performed under the double ionization limit, the connection between quantum mechanics and classical mechanics can be further explored.

The first time domain experiment under the double ionization limit was conducted by using a series of short laser pulses to prepare the doubly excited electronic wave packets with controlled energies [49]. That experiment was focused on the final products after autoionization to infer the dynamics of the two-electron atom. The experimental results suggest that the energy exchanged between two electrons does not occur gradually. Instead, the radius where two electrons meet is an important parameter to determine the redistribution of energy. However, the direct time-dependent measurement is not available until now. In this dissertation, we present an effort to use a sub-picosecond, unipolar electric field pulse, i.e. half-cycle pulse (HCP), to directly probe the evolution of double Rydberg wave packets (DRW) in order to provide a “real-time” view of energy exchange between two electrons within the same atom. In the following sections of this chapter, Rydberg atoms and wave packets will be briefly discussed. Finally, the outline of this dissertation will be stated.

1.3 Rydberg atoms

In the 19th century, the physicist, Johannes Rydberg, found out the formula to describe the spectrum of Hydrogen and Hydrogen-like atoms using Rydberg constant and the wave numbers of a series number [14]. The energy levels of the Hydrogen atom can be described as

$$E_n = -\frac{1}{2n^2} \quad (1.2)$$

in quantum theory. The Hydrogen-like atoms, alkali or alkaline-earth atoms, can be explained

$$E_n = -\frac{1}{2(n - \delta_l)^2} \quad (1.3)$$

by quantum defect theory [15]. Where δ_l is the quantum defect, which is different for different momentum, l . Rydberg atoms are atoms in excited states with high principal quantum number n , where n is greater than 10.

A comprehensive overview of experimental and theoretical studies of Rydberg atoms have been given in Reference [15]. Some exaggerated properties of Rydberg atoms, as highlighted in table 1.1 with values for $n = 30$, make them good samples to study the physics of atoms. The first benefit of Rydberg atoms is the easy manipulation by relative small electromagnetic fields. This originates from the property that the binding energy of Rydberg atoms decreases as $1/n^2$ and their orbital radii increases as n^2 . Classically, an electron in a pure Coulomb potential with the energy $E = -1/2n^2$ will orbit the core at a period of $\tau = 2\pi n^3$. Correspondingly, the radial Rydberg wave packet with the energy splitting of constituent eigenstates about n^{-3} will have similar periodical feature, which is suitable for time-dependent study using available ultrashort laser pulses. Furthermore, the alkaline Rydberg atoms can not

only be described quantum mechanically—by adapting the Hydrogen wave function and considering the screening of ion by the other electrons as perturbation—but also be treated classically as planetary problem because of their large orbit radii.

Alkaline atoms are superior to Hydrogen in most experiments studying Rydberg atoms, because it is easier to promote the alkaline atoms into Rydberg states, by using lasers within visible spectrum region through one/two photon transitions. Due to the same reasons, the atomic sample used throughout this dissertation will be Barium (Ba) instead of the Helium atom.

Table 1.1: Some properties of Rydberg atoms

Property	n dependence	n=30
Binding energy	$1/n^2$	$122cm^{-1}$
Orbital radius	n^2	$1800a_0$
Kepler period	n^3	4.1psec
Field ionization limit	$1/n^4$	400V/cm

1.4 Wave packets

The macroscopic world has more in common with classical physics than quantum physics, thus physicists make it a priority to link these two. The correspondence principle in the limit of large quantum numbers provides one connection. Wave packets, the coherent superposition of wave functions in quantum mechanics first recognized by Schrodinger [17] connect both regime by the similarity between oscillating time-dependent probability and their classical counterpart electrons evolution as a function of time [18].

A wave packet is usually a non-stationary, spatially localized quantum state in experimental atomic physics, which is the superposition of many stationary states (eigenstates), mathematically described as [57]

$$\Psi(t) = \sum_j C_j(t) \psi_j e^{-i(E_j t + \phi_j)} \quad (1.4)$$

where $C_j(t)$ is the amplitude of a constituent eigenstate ψ_j . E_j and ϕ_j are the energy and constant phase of each eigenstate, separately. Therefore, the time-dependent probability distribution can be written as

$$P(t) = \sum_{j,k} C_j C_k \psi_j \psi_k e^{-i[(E_k - E_j)t + (\phi_k - \phi_j)]}. \quad (1.5)$$

If there is no external interaction, the amplitude of each eigenstate is unchanged as time elapses, but its phase evolves at different rate corresponding to its energy, E_j . As a result, the probability distribution of wave packets changes as constituent states evolve in and out of phases. Various information will be encoded into the time-dependent amplitudes when wave packets interact with the external world. In atomic physics, there are many time-dependent problems, such as atoms/particles collision, electron correlations within atoms or the atomic response to electric fields [11]. Monitoring the evolution of wave packets can give important insights into these complicated problems.

There are many types of wave packets and various techniques to produce them. One of the most common wave packets produced in atomic physics labs is the radial wave packet [11], which is the wave packet used in the experiments described in this dissertation. A short laser pulse can coherently transfer atoms from the ground state or an intermediate state into several final states within the laser bandwidth, creating electronic wave packets in atoms in which electron oscillates in the radial coordinate of the spherical coordinate system but invariant in the other two angular coordinates. Upon the laser excitation, the wave packet is initially localized near the ion core

of atom where the expectation value of radial operator, \hat{r} , is small. After the laser pulse, the wave packet moves outward and is reflected back by the Coulomb potential barrier forming a periodical radial motion. The period of such motion, $\tau_k = 2\pi n^3$, where n^{-3} is the average energy level splitting of constituent states, is identical to the period of a classical electron with the same energy, $E = -1/2n^2$. The radial wave packet corresponds to an ensemble of classical electrons traveling in similar classical orbits with the same phase but different angular orientations in space. The electrons are initially localized at the inner turning points of their orbits. Half a Kepler period later, the electrons reach the outer turning points of their respective orbits. More discussion will be found in chapter 4, especially the characters of ionic radial wave packets.

1.5 Structure of Dissertation

This dissertation is organized to describe three related experiments in series. After introducing the experimental apparatus in chapter 2, the concept and the laboratory realization of a half-cycle pulse (HCP) and its interaction with a Rydberg ion are described in chapter 3. The time-dependent double ionization of ionic radial wave packets measurement using the HCP as a time-sensitive probe is presented of chapter 4, which provides a method to characterize the quantum states in ionic wave packet. In chapter 5, double Rydberg wave packets (DRW) will be prepared with controlled initial energy and relative positions. The time-dependent energy exchange between two electrons in such a system is monitored by recording the double ionization probability while scanning the HCP relative to the production of DRW. Finally, the conclusion and outlook are given in chapter 6.

Chapter 2

Experimental Apparatus

2.1 Introduction

Proper apparatus play an important role in the experiments presented in this dissertation. Since the experiments involve time domain spectroscopy, which requires short laser pulses. The femtosecond Ti: Sapphire laser system is introduced at the beginning of this chapter, followed by descriptions of optical parametric amplifiers and dye lasers that are used to excite atom samples into desired states. Finally the atom source, the vacuum system and the detection method are presented in some detail. The generation of short terahertz radiation and some related issues will be discussed in a later chapter.

2.2 Femtosecond Ti:sapphire laser system

The primary laser used in the experiments discussed in this dissertation is a ~ 100 femtosecond Ti: Sapphire system, which is based on the chirped pulse amplification(CPA) [19] technique. The CPA is a technique which is commonly used for

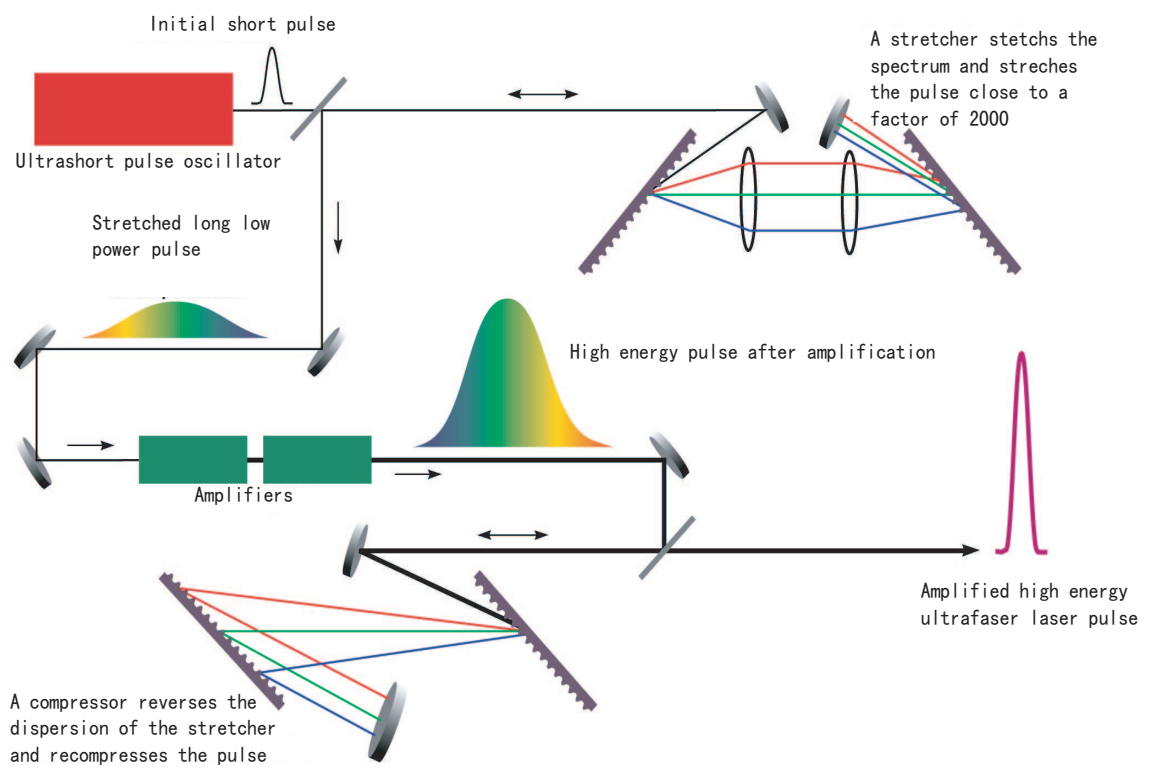


Figure 2.1: Schematic scheme of chirped pulse amplification [20]

amplifying ultrashort laser pulses. In CPA, the laser pulse is stretched out temporally prior to amplification, then is compressed back to something close to its initial duration. This technique avoids high peak intensity in the amplifiers dramatically reducing non-linear effect, such as self-phase modulation, stimulated raman scattering, and self-focusing, and greatly extends the peak powers that are attainable without damaging the gain medium. Fig. 2.1 [20] shows the schematic setup of the Ti:Sapphire laser system similar to that used in the laboratory. The ultra short pulse generated from an oscillator is expanded in time by a stretcher prior to introducing it into regenerative and multipass amplifiers. The amplified pulse is finally sent to a compressor to restore it close to its original duration. In this section, we will describe each component separately and introduce a device, the single short autocorrelator, to characterize an ultra short laser pulse.

2.2.1 Oscillator

The oscillator used in this project is a ~ 30 fsec, 800nm MTS Mini Ti:Sapphire mode-locked laser from Kapteyn-Murnane Laboratories Inc. The Ti: Sapphire crystal has a broad optical gain bandwidth (700nm-1000nm). Therefore, when the crystal absorbs ~ 4.0 W 532nm cw-laser light from a Nd:YVO4 laser (Spectra-Physics Millennia Vs), there are on the order of 10^5 possible longitude modes in the oscillator cavity. When a sudden perturbation is applied to the prism P2, the optical pulse produced by the disturbance is preferentially amplified. A non-linear process, called optical Kerr-lens, occurs while the pulse intensity increases. Because of this process, an intense pulse creates a positive lens, which focuses itself inside crystal, effectively creating a fast saturable absorber. In frequency domain, this process makes longitudinal modes in phase. These modes then constructively interfere with one another, producing

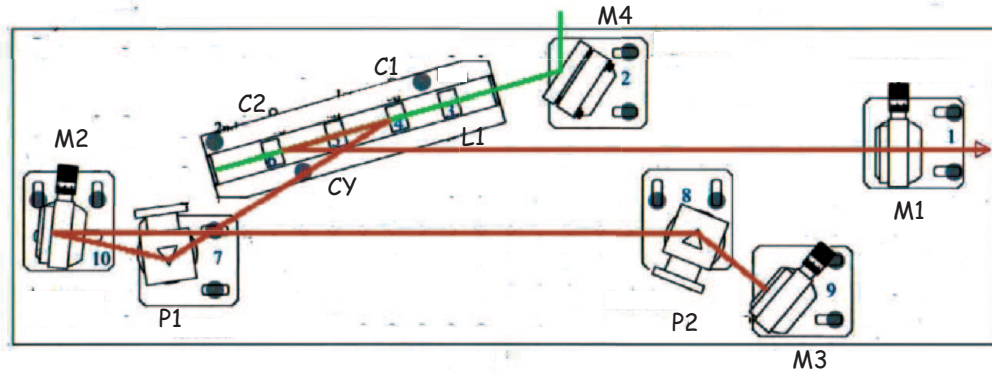


Figure 2.2: Basic layout of Oscillator [22]. M1, M2, M3, C1 and C2 form X shape laser cavity. M2 folds the laser cavity. M4 and L1 direct and focus pump light to crystal. P1 and P2 are prisms.

a short pulse. Furthermore, the Kerr-lens effect can induce self-phase modulation, which broadens the effective frequency spectrum which constructively interfere with other frequencies making the laser pulse even shorter [21]. However, as the laser pulse passes through various optical components, each frequency experiences a different index of refraction. Therefore, they travel at different velocities. This phenomena is known as group velocity dispersion (GVD). If left uncompensated, GVD would prevent stable circulation of short pulses in cavity. A pair of negative GVD prisms is introduced to reduce such effect.

2.2.2 Stretcher and compressor

Before sending the laser pulse from the oscillator into the amplifier, a stretcher expands the laser pulse in time to limit the peak power to avoid damaging the optical components in the laser system. Moreover, the alteration of the spatial beam profile as

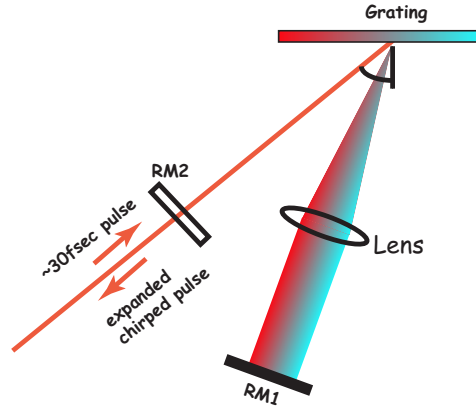


Figure 2.3: Schematic diagram of the Stretcher. RM1 and RM2 are retroreflection mirrors, which diffract light off grating four times. The output chirped pulse is temporally expand about a factor of 2000 [23].

well as the temporal profile of the pulse due to the non-linear effects can be prevented. Fig 2.3 is a schematic diagram of the stretcher. The short pulse enters the stretcher 2mm above RM2 and is diffracted off the grating. Each frequency component of light is diffracted at a different angle, passes through the lens and reflects back to grating by mirror RM1. During this process, the redder frequency travels a shorter distance than the blue portion of laser spectrum. As a result, the laser pulse is chirped and expanded in time [24]. The retroreflection mirror RM2 causes the laser pulse to experience such process once more, which eliminates the spatial chirp introduced in the first pass as well. The expanded chirped pulse exits the stretcher slightly above the input beam.

After the laser pulse is amplified as described in the next section, a compressor is used to undo the chirped pulse introduced by the stretcher. Fig 2.4 shows the schematic setup of the compressor used. It works in a similar way as the stretcher except that the red portion of laser spectrum experiences a longer path than blue part [25]. As a consequence, the incident angle at grating has to be set the same as the one in stretcher. However, in practice, the compressor undergoes fine adjustment

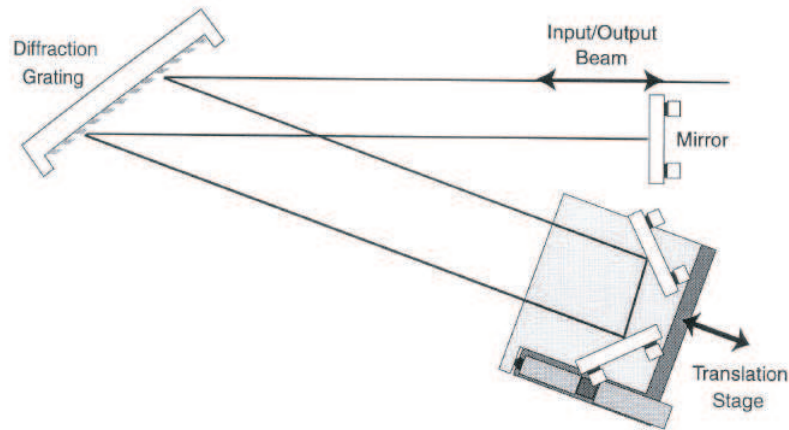


Figure 2.4: Schematic setup of the compressor [26]. The amplifier laser pulse diffracts from the grating four times using a retroreflection mirror and two mirrors mounted on a translation stage, which provides fine tuning of the group velocity dispersion.

of both the incident angle and distance between grating and translation stage in order to compensate the non-linear dispersion from optical components in amplifiers. But, this compressor can not compensate all dispersion, especially the higher order dispersion. Furthermore, amplifiers do not equally amplify each frequency component in the seed light, which effectively reduces the bandwidth of the amplified laser pulse. As a result, when the laser pulse comes out the compressor, its duration is restored to ~ 100 fsec instead of its origin 30 fsec.

2.2.3 Regenerative and multipass amplifier

Prior to sending the laser pulse into the compressor to restore the short duration, it goes through two stages of amplification in a regenerative and a multipass amplifier. The regenerative amplifier (regen) is shown in Fig. 2.5, and is a laser cavity by itself. The expanded chirped laser pulse with vertical polarization, referred to as the seed pulse, enters the regen by reflection from the thin film polarizer TP1. TP1

reflects vertically polarized light and transmits horizontally polarized light . The polarization of laser pulse is then rotated 90° after it passes the Pockels cell PC1 with high voltage applied, reflected by mirror M1 and passes PC1 again. It becomes horizontally polarized laser pulse, which can travel through the TP1. The voltage on PC1 is then turned off in order to prevent another laser pulse from entering the regen. The horizontally polarized laser pulse extract the optical energies stored in the Ti:Sapphire crystal pumped by the 532nm laser light from a Spectra-Physics Quanta Ray GCR Nd:YAG laser. The amplified laser pulse goes through M3, TP2, PC2 and is reflected back by the mirror M2. After approximately twenty round trips inside regen, the laser pulse, which gives a factor 4×10^6 amplification, is switched out the regen from TP2 when a high voltage is applied on Pockels cell PC2 to rotate the laser polarization from horizontal to vertical polarization, which is realized by laser pulse pass PC2, M2 and PC2 in sequence.

The amplified laser pulse from the regen is then sent into the multipass amplifier (Fig. 2.6), which is the second stage of amplification. In the multipass amplifier, the laser pulse passes through a second Nd: YAG pumped Ti: Sapphire crystal three times, resulting in up to a factor of 10 additional amplification. A typical energy of laser pulse is $\sim 30mJ$ after two amplifiers. A telescope expands the beam size of the amplified pulse before it is sent into the compressor in order to reduce the spatial and temporal distortions of amplified pulse due to the nonlinear effects . This prevents damaging the grating inside the compressor as well.

A high power optical feedback from amplifiers can damage or disrupt the operation of oscillator. A optical faraday isolator, a wave plate (optical rotator) and a polarizer are introduced to reduce this feedback. The faraday optical isolators (based on the Faraday effect) rotated the polarization of the seed pulse 45° clockwise from

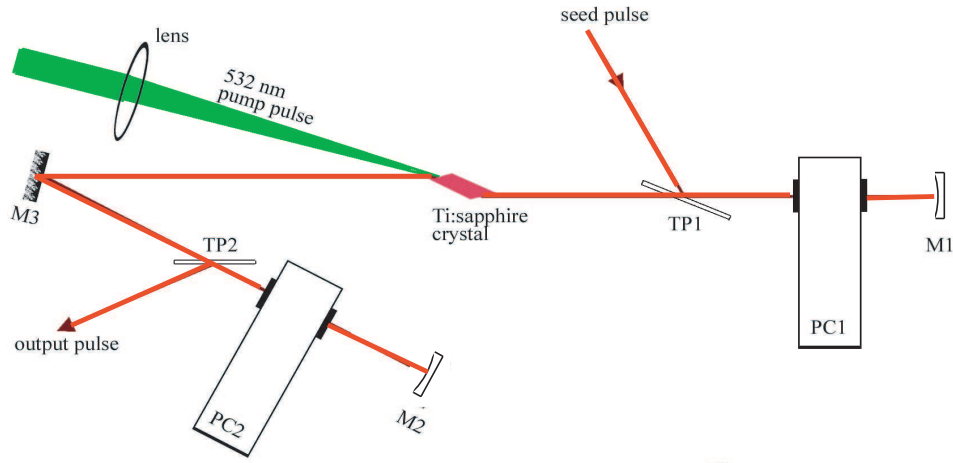


Figure 2.5: Regenerative amplifier [27]. TP1 and TP2 are thin film polarizers. PC1 and PC2 are Pockels cells which control the time that a seed pulse is switched in or out the regen cavity. M1, M2 and M3 are reflection mirrors forming the regen cavity.

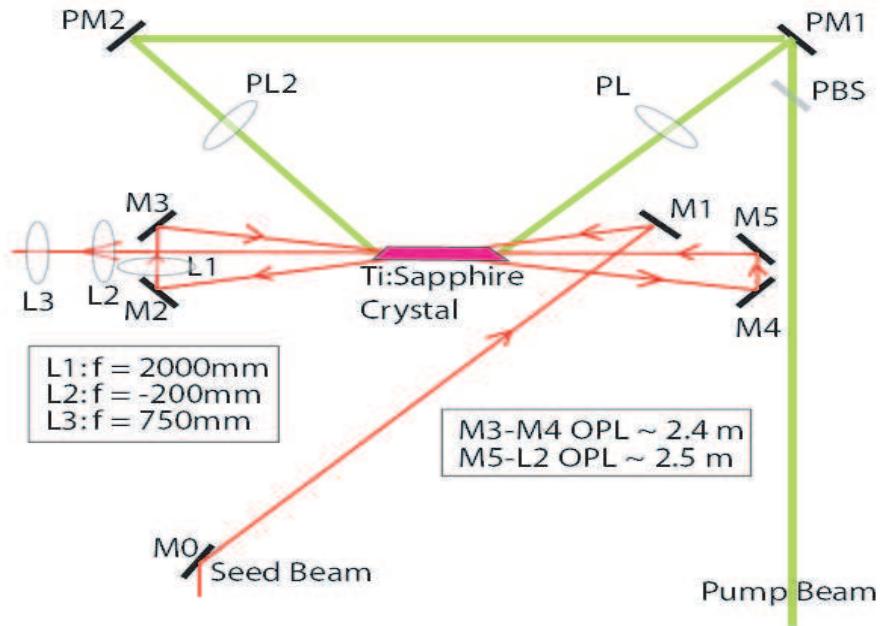


Figure 2.6: Multipass amplifier [29].

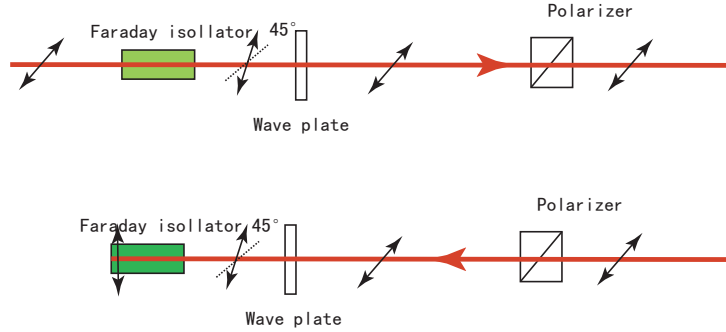


Figure 2.7: Schematic of optical isolation between the oscillator and amplifiers.

horizontal. Then it is restored back horizontal after the wave plate before entering stretcher, which depends on the birefringence of crystal. The feedback of amplified pulse is horizontal polarized before the wave plate. Its polarization is turned clockwise 45° after the wave plate and additional 45° by the faraday isolator. Finally, the vertical polarized feedback pulse is blocked by the isolator with the polarizer built in the faraday isolator.

2.2.4 Single shot autocorrelator

It is difficult to characterize the femtosecond laser pulse because of the slow response time of electronic detectors. However, this can be overcome by using the autocorrelation method [28]. We use a single-shot autocorrelator design in which two identical femtosecond laser pulses cross in a BBO frequency doubling crystal at an angle, 2ϕ . The distribution of doubled light energy detected by a CCD camera array is proportional to the intensity autocorrelation of the pulses. The intensity autocorrelation of the pulse is defined as

$$I_{2nd}(\tau) = \int I_{1st}(t)I_{1st}(t + \tau)dt. \quad (2.1)$$

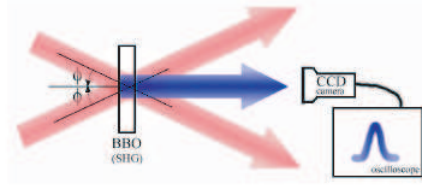


Figure 2.8: The single shot autocorrelator [27]. Two identical ultra short laser pulses intersect at a BBO crystal producing second harmonic light whose intensity profile encodes the temporal shape of the ultra short laser pulse.

If we define $x=0$ at the position where the center of two laser pulses arrive simultaneously, then at the position x from the origin, the maximum double light intensity occurs with two intercepted laser pulse with time difference $\tau = 2xn \sin(\phi)/c$, where n is index of refraction; c is the speed of light. Therefore, the temporal information of the short laser pulse is mapped into the spatial plane in terms of the intensity of the second harmonic light.

In order to calibrate the single shot autocorrelator, a glass slide with known optical length is inserted in the path of one laser pulse. The spatial translation of the second harmonic's intensity profile is calibrated to be the time $t = (n_0 - 1)d/c$, where n_0 is index of refraction of the glass slide; d is the thickness of the glass slide. From this correspondence, the full width half maximum of the short laser pulse can be obtained by

$$\Delta t = \Delta t_{2nd}/1.55, \quad (2.2)$$

where Δt_{2nd} is the FWHM of autocorrelation signal, the factor 1.55 is derived by assuming a $sech^2(t)$ shape of the laser pulse.

2.3 Optical parametric amplifier

In order to produce a sub-picosecond laser pulse with tunable wavelength, an Optical Parametric Amplifier (OPA) is used. The OPA is based on a parametric nonlinear interaction, which using a non-linear crystal coherently converts a light with frequency ω_p into two different frequencies, ω_s and ω_i , where $\omega_p = \omega_s + \omega_i$.

There are two OPAs set up in a similar way as shown in Fig. 2.9. A small fraction ($< 1\%$) of the amplified 780nm laser pulse is focused into a quartz plate producing a spectrally “white light” pulse. This light is used to “seed” the OPA. Approximately $2mJ$ of amplified Ti: Sapphire laser pulse goes through a BBO (Beta Barium Borate) doubling crystal C1 generating 390nm light. This doubled light and seed light are collimated and then overlapped spatially and temporally on another BBO crystal(C3). The specific frequencies of ω_s and ω_i are selected by the phase matching condition, which is set by angle tuning of the crystal with respect to the incident light. The amplified light is then reflected back by a blazed grating to be amplified by the 390nm light produced from the other $\sim 6mJ$ amplified 780nm laser light. A grating rather than a reflection mirror is used in the OPA in order to limit the bandwidth of output laser light for our specific Rydberg experiments. The grating is orientated in a way that it disperses the light in the phase-matching plane of the OPA crystal C3. Due to the polarity of the angular dispersion, the +, - diffraction orders of preamplified light behave differently while being amplified by the crystal. With one orientation (i.e. + or - angle relative to normal incidence) of the diffraction grating, the angularly dispersed preamplified light will improve phase-matching over a range of frequencies, broadening the spectrum of the output light, which in principle can enable the production of shorter pulses. On the other hand, with the other orientation, the angular dispersion will have the opposite sign, and phase matching is

limited to a more select range of frequencies narrowing the spectrum of light, which is usefully for limiting the dispersion in the Rydberg wave packets experiments.

2.4 Dye lasers

Another type of tunable lasers used in experiments is a dye laser. The dye laser uses an organic dye as a lasing medium, usually in a liquid solution. The gain bandwidth of most laser dyes greatly exceeds that of most gaseous and solid state lasing media. The wide bandwidth makes them particularly suitable for tunable lasers and pulsed lasers. Moreover, the same dye laser setup can be used for generating different frequency laser lights by simply changing laser dyes. The dye lasers used in laboratory are usually home-made in two different styles, H \ddot{a} nsch style (Fig.2.10) [31] and Littman style (Fig. 2.11) [32]. The organic dye circulates through a quartz cell mounted on the axis of an optical resonator. The third/second harmonic of Nd:YAG laser is focused on the dye cell by a cylindrical lens creating a population inversion. The resulting fluorescence propagates inside the cavity and certain modes begin lase when the gain of the light exceeds the lose in the cavity. A typical bandwidth of pulsed dye laser is about 5-10nm without any dispersion components inside the resonant cavity [33]. By placing a dispersive component, a grating, the frequencies of fluorescence are spread out. The frequencies aligned with the cavity can lase. Therefore, the line-width of output laser light is reduced. Moreover, the turnable gating in the H \ddot{a} nsch style or the mirror as in the Littman style can select specific frequencies that resonate with the cavity. Consequently, The wavelength of laser pulse can be adjusted for different laser excitations in experiments.

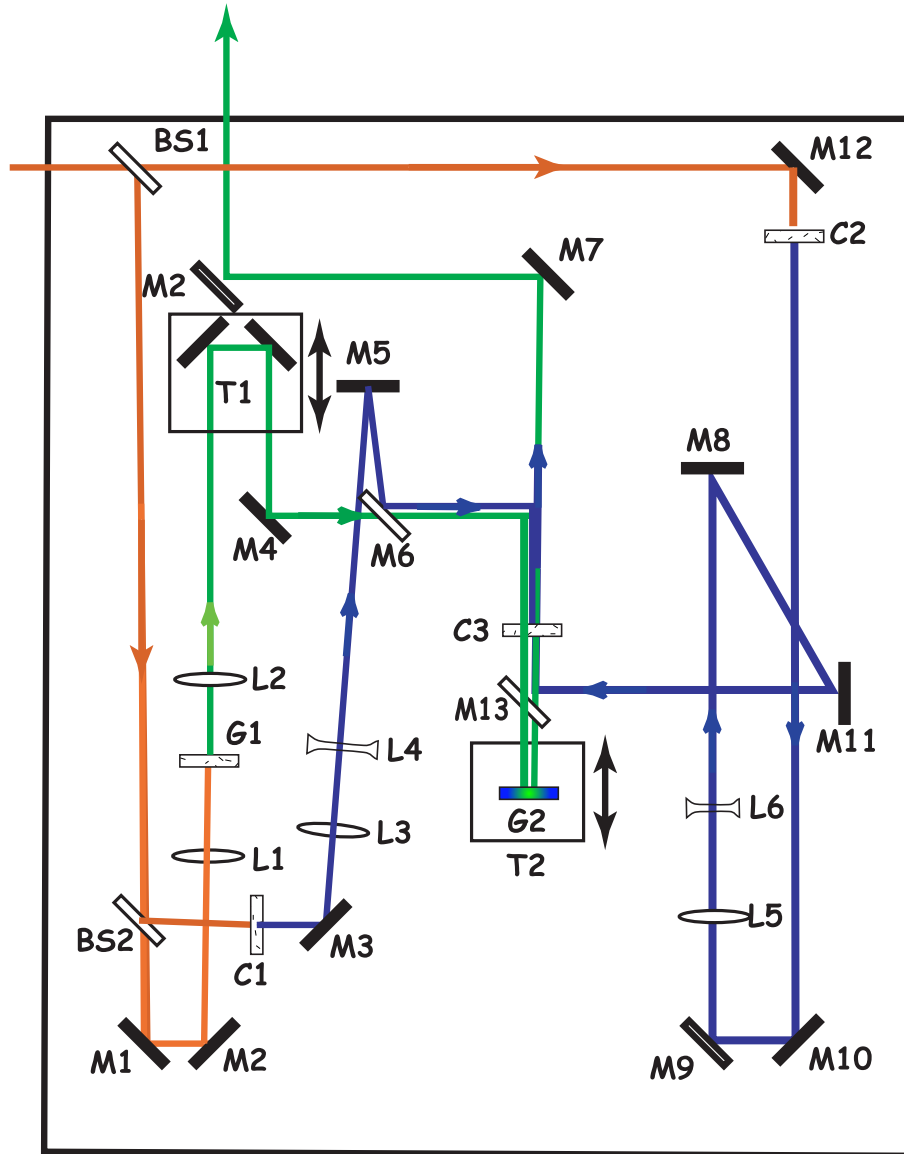


Figure 2.9: Optical parametric amplifier setup diagram. The input is ~ 100 fsec 780nm laser light. A tunable laser(450-700nm) is produced from OPA. C1, C2 and C3 are 1 mm BBO (Beta Barium Borate) crystals or a 1 cm thick KDP(Potassium Dihydrogen Phosphate) crystal. BS1 and BS2 are beam splitters. L1-L6 form telescopes to collimate beams. M1-M12 are either metal coated mirrors or dielectric coated mirrors. G1 is a quartz plate and G2 is a blazed grating. T1 and T2 are translation stages to adjust the relative delay between laser pulses.

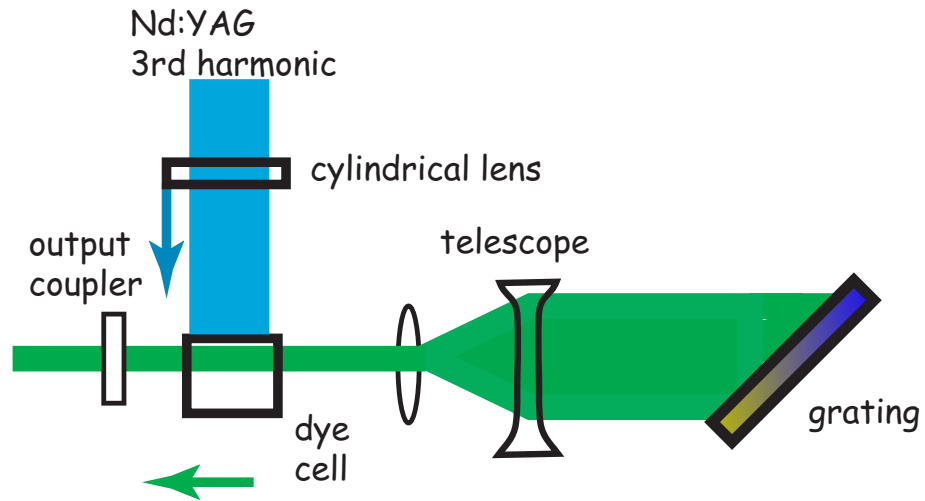


Figure 2.10: Hansch style dye laser

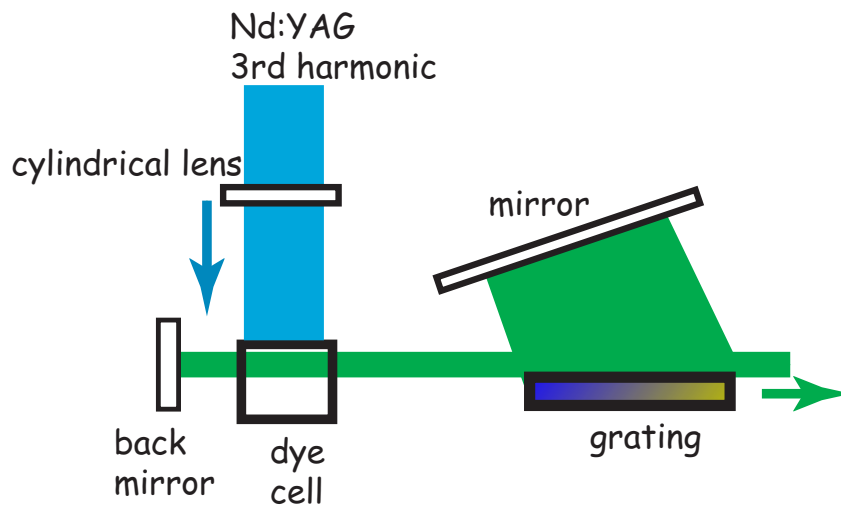


Figure 2.11: Littman style dye laser

2.5 Atom source, vacuum system and detector

The laser pulses eventually interact with atom samples that are isolated from air inside a vacuum chamber. The electrons/ions resulted from the laser-atom interaction are collected by Microchannel detector and recorded.

2.5.1 Atom source

The Ba atoms are used for all experiments described in this dissertation. Ba is chosen over other elements with two valence electrons because of the availability of lasers for multi-step excitation of double Rydberg wave packets.

An effusive beam of ground state Ba atoms is produced by resistively heating a stainless steel tube with a 1mm hole in the side. The 6" long, 3/8" diameter stainless steel tube is filled to the 1mm hole with Ba solid. The filled tube, the so-called "oven", is clamped inside the chamber with the exit hole pointing toward the interaction region where lasers and the atom beam meet. The two ends of the oven tube are connected to an AC high current supply. The current supply consists of a set of 120V to 6V AC transformers and a Variac AC voltage regulator which is used to control the current. As a current flows through the oven, the tube is heated up so that Ba atoms are vaporized, leave the oven through the exit hole, and move toward the interaction region. A water cooled copper shield placed between the oven and interaction region prevents optical components and detector from being coated by the effusive atomic beam.

2.5.2 Vacuum system

The experiments are performed inside a chamber with a background pressure $\sim 10^{-6}$ torr. The aluminum chamber is 45 cm in diameter and 30 cm high with eight cylindrical flanges allowing laser beams, electrical pulses and cooling water to enter the chamber (Fig. 2.12). A Varian VHS-6 water-cooled diffusion pump and a Welch model 1376 mechanical roughing pump are used in series to continually pump the chamber. The pressure inside the vacuum chamber is monitored with a model 571 Bayard-Alpert Type Standard Range Ionization Gauge Tube, model 531 thermocouple gauge tubes and a model 843 ionization gauge controller from Varian.

2.5.3 Detection and data acquisition

The laser-atom interaction region is located between two parallel $2'' \times 2''$ aluminum plates vertically separated by 1.25cm. A voltage pulse applied on the lower plate pushes the electrons or ions produced by laser-atom interaction through the 2mm hole in the top plate. These charged particles are detected with a pair of microchannel plates (MCPs). MCPs detect charged particles by creating an avalanche of electrons whenever an ion or an electron hits the surface of the plate. The surge of electrons is proportional to the number of electrons or ions hitting the microchannel plates under normal work conditions. A pair of microchannel plates enhance the magnification of the signal by a factor of about 10^6 . The electrons from MCPs are collected on a metal plate and the resulted current is measured and displayed in an oscilloscope (LeCroy 9350A) . A computer program, DC written by Dr. T.J. Bensky, is used to transfer the signal to a personal computer through a GPIB interface.

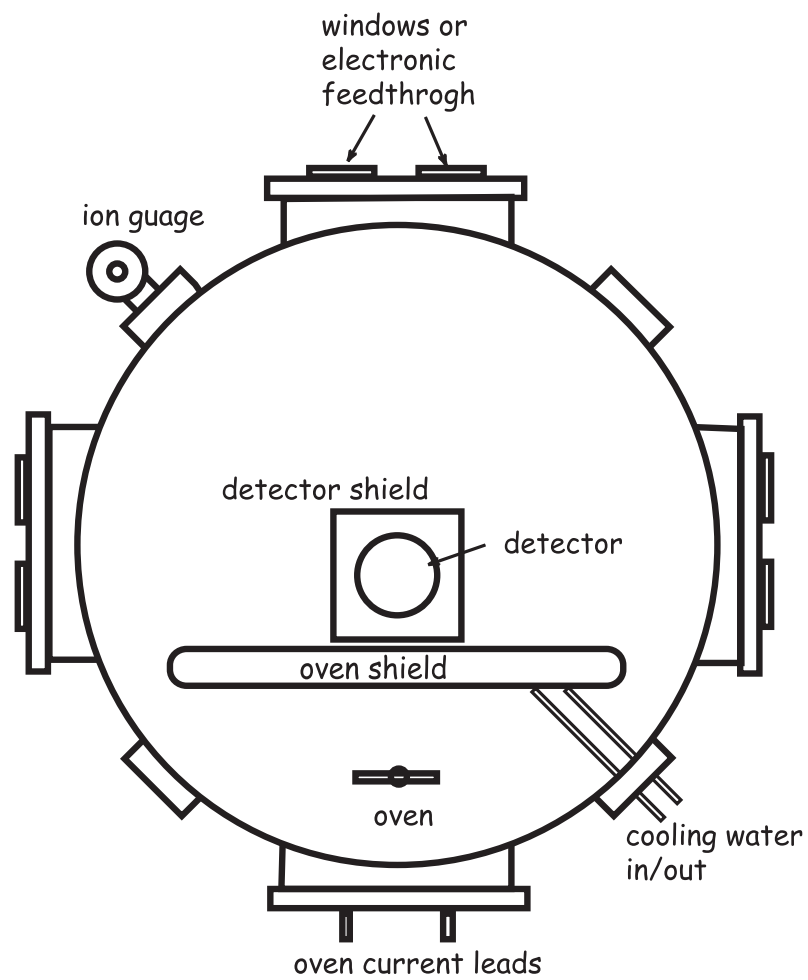


Figure 2.12: Top view of the schematic diagram of the vacuum chamber.

Chapter 3

Half-Cycle Pulse Ionization of Ba^+ Rydberg Ions

3.1 Introduction

Terahertz radiation lies between infrared and microwave in the electromagnetic spectrum. The interaction between strong Terahertz radiation and weakly bound Rydberg atoms can be exploited to perform quantum control experiments and/or for probing electronic dynamics. The first experiments exploring impulsive ionization of Rydberg atoms by very brief, nearly unipolar electric field pulses [34] were performed a little over a decade ago [35]. Immediately following that initial work, a host of theoretical [36–39] and experimental [40–43] studies further characterized the interaction of Rydberg atoms with these half-cycle pulses (HCPs), particularly in the short-pulse regime where the HCP duration is less than the classical Kepler period of the Rydberg electron. More recently, HCPs have been used as tools to manipulate and view Rydberg electron dynamics [44–47, 51], but to the best of our knowledge, only neu-

tral atoms with single Rydberg electron have been considered to date. However, new experiments [49] investigating electron interactions in double-Rydberg wavepackets (DRW) beg the question: Can HCPs be used to control and probe correlated two-electron dynamics as well? We suspect that the answer to this question is yes, but the nature of the HCP interaction with DRWs and the singly-excited Rydberg ions that are formed following their autoionization must first be verified. In an initial step toward this goal, the impulsive HCP ionization of Rydberg ions is presented in this chapter.

3.2 Half cycle pulses

There are two different commonly used approaches to generate terahertz radiation, Optical rectification [52] and Optically gate antenna [34]. The terahertz radiation used in experiments discussed in this dissertation is produced using the photoconductive antenna. A biased Gallium Arsenide (GaAs) semiconducting wafer is illuminated by an ultra-short laser pulse. The photons in the laser pulse have sufficient energy to promote electrons from the valence band into the conduction band, creating electron-hole pairs. These carriers are accelerated by an applied electric field across the wafer surface, resulting in a surface current, $J(t)$. The change in the current produces THz radiation. The magnitude of radiated electric field is proportional to the acceleration of carriers, and, therefore, to the time derivative of the surface current.

$$F_{thz}(t) \propto \frac{\partial J(t)}{\partial t} \quad (3.1)$$

The surface current depends on the incident laser and bias electric field applied to the wafer. When illuminated with sufficient laser fluence, $40\mu J/cm^2$ for GaAs, the

generated electric field strength is proportional to the bias field. Thus, the bias field provides a convenient control knob for adjusting the THz strength. In addition, the polarity of generated THz field can be controlled by switching the polarity of the bias field.

Fig. 3.1 shows a schematic of the photoconductive antenna used in our experiments. An undoped, (100) oriented GaAs semiconducting wafer is connected to a high voltage supply using silver paint electrodes. A thin layer of Norland Optical Adhesive 88 is applied to the outer surface of the electrodes to prevent sparking on the surface, which can damage the wafer and produce unwanted noise in terahertz radiation. The time-dependence of a typical terahertz electric field generated by such a device is characterized by a narrow sharp maximum followed by a long, much lower amplitude opposite polarity tail (as shown in Fig. 3.2). The main lobe of the pulse has a full width at half maximum < 1 picosecond. Whereas the duration of the weak tail is 10's to hundreds of picoseconds. Ionization dynamics are governed by the main lobe provided the relevant time scale, the Kepler period of Rydberg electron, is longer than 1 psec but much shorter than the duration of tail [43]. Accordingly, atomic physicists commonly refer such terahertz pulses as unipolar or “half-cycle” pulse as the pulse contains roughly half of an optical cycle of the THz field.

3.3 HCP Ionization of Ba⁺ Rydberg Ions

In an initial step toward using the HCP in DRW experiments, we investigated the impulsive HCP ionization of Rydberg ions. Laser-excited Ba⁺ Rydberg ions are exposed to 0.8 psec HCPs and the production of doubly-charged ions is measured as a function of the peak HCP field. The impulse delivered to the Rydberg ions is cali-

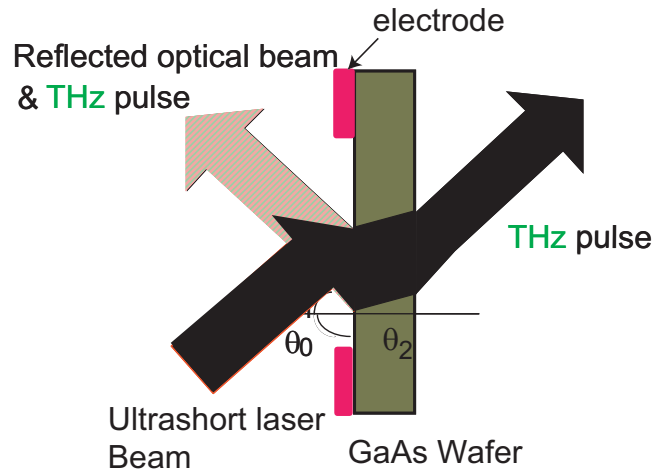


Figure 3.1: Diagram of HCP generation [53]. An ultrashort laser pulse promotes the electrons of biased wafer from valance band to conduction band. The carriers accelerate under the biased field creating the Terahertz radiation. The incident angle of the laser θ_0 is adjusted close to 90° in the experiment.

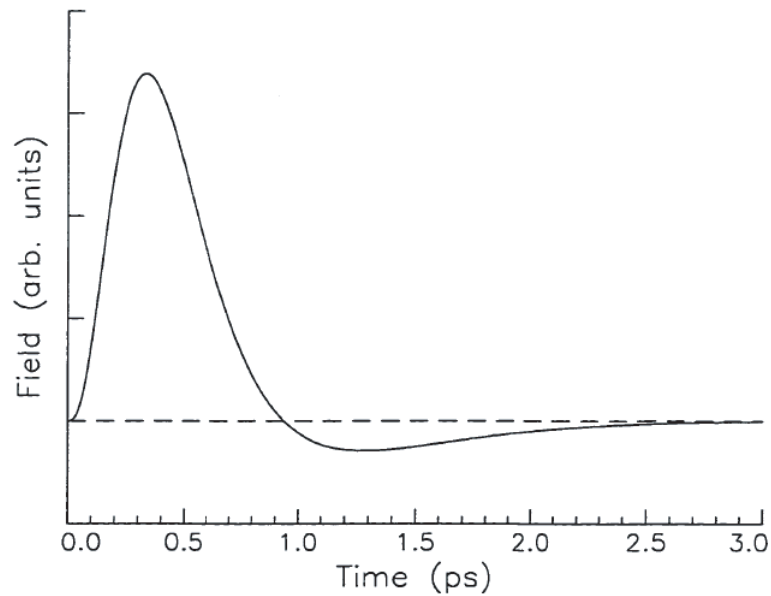


Figure 3.2: Schematic electric field strength of HCP as a function of time generated from photoconductive emitters with ultrashort pulses. [34, 55]

brated by measuring analogous HCP ionization yields for neutral Ba Rydberg atoms that are produced in the same interaction volume. As noted early, HCP ionization of neutral Rydberg atoms has been well characterized in the impulsive short-pulse regime [40–43]. We find that Rydberg ions and neutral Rydberg atoms with the same binding energy have approximately the same ionization vs. HCP impulse curves. These observations are in agreement with both an analytical impulsive ionization model and classical trajectory Monte Carlo (CTMC) simulations.

3.3.1 Experimental procedure

The experiments proceed similarly to others that have been described in detail elsewhere [35, 40]. Rydberg ions or neutral Rydberg atoms are produced via pulsed laser excitation of a thermal beam of ground-state Ba atoms in a vacuum chamber with a background pressure of 1×10^{-6} Torr. The atoms/ions are then exposed to a 0.8 psec HCP that is created by illuminating, in vacuum, a biased $1.5\text{cm} \times 1.5\text{cm} \times 0.05\text{cm}$ GaAs wafer with a 100 fsec, 780 nm laser pulse from an amplified Ti:Sapphire laser [34]. The peak HCP field is linearly polarized parallel to the wafer bias field and has a magnitude that is proportional to the bias voltage. The HCP radiation is collected and directed into the laser/atom interaction region using a gold coated off-axis paraboloid with a 10 cm focal length. The atoms interact with the lasers and HCP between two parallel aluminum plates separated by 1.25cm. Approximately 10 nsec after the HCP, a small pulsed voltage, 30-60V applied to the lower field-plate, pushes any positive ions in the interaction region through a 0.2cm diameter hole in the upper field-plate, toward a microchannel plate (MCP) detector. Singly and doubly charged ions are distinguished by time-of-flight to the detector. The number of singly or doubly charged ions created by HCP ionization of neutral or

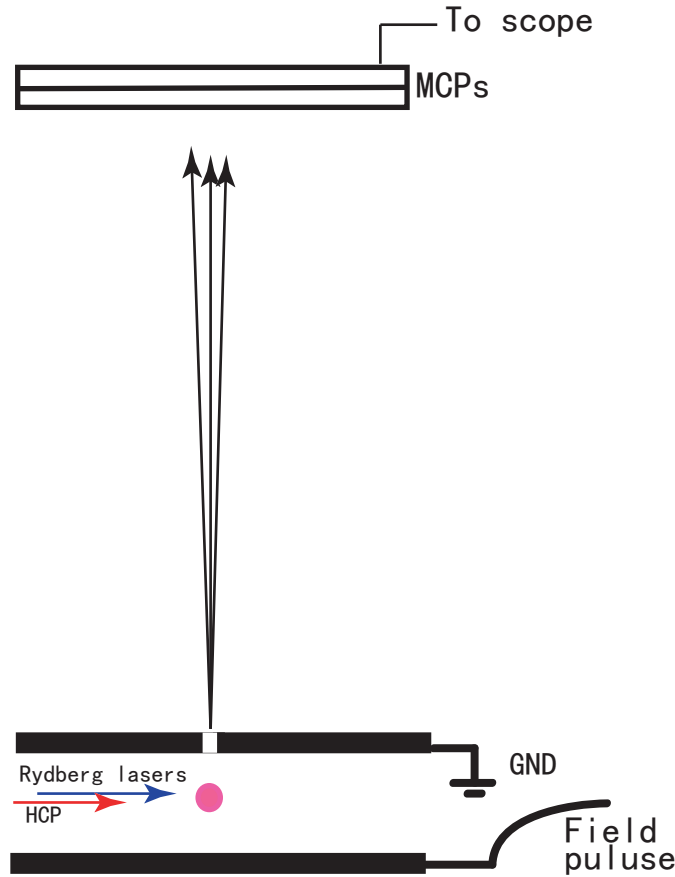


Figure 3.3: The diagram of experimental set up. Rydberg lasers are laser pulses that excite Ba atoms from ground states either into $6snd$ neutral Rydberg states or ng^+ ionic Rydberg states. After these lasers, a HCP with variable strength ionizes the Ba atom sample. A positive field ionization pulse pushes remaining particles into MCP detector.

ionic Rydberg states, respectively, is recorded as a function of peak HCP field as the bias voltage on the GaAs wafer is continuously scanned. The two laser excitation schemes are shown in Fig. 3.4 Neutral $6snd$ Rydberg atoms are produced using two tunable, 5 nsec dye-laser pulses (553.7 nm and 420 nm, $\sim 100 \mu\text{J}/\text{pulse}$) which sequentially excite $6s^2$ ground-state atoms through an intermediate $6s6p^1P_1$ level to a selected $6snd$ Rydberg state with $15 < n < 45$. Ba ng^+ Rydberg ions are created in a three-step, four-photon excitation. First, a 350 nm pulse stimulates two-photon

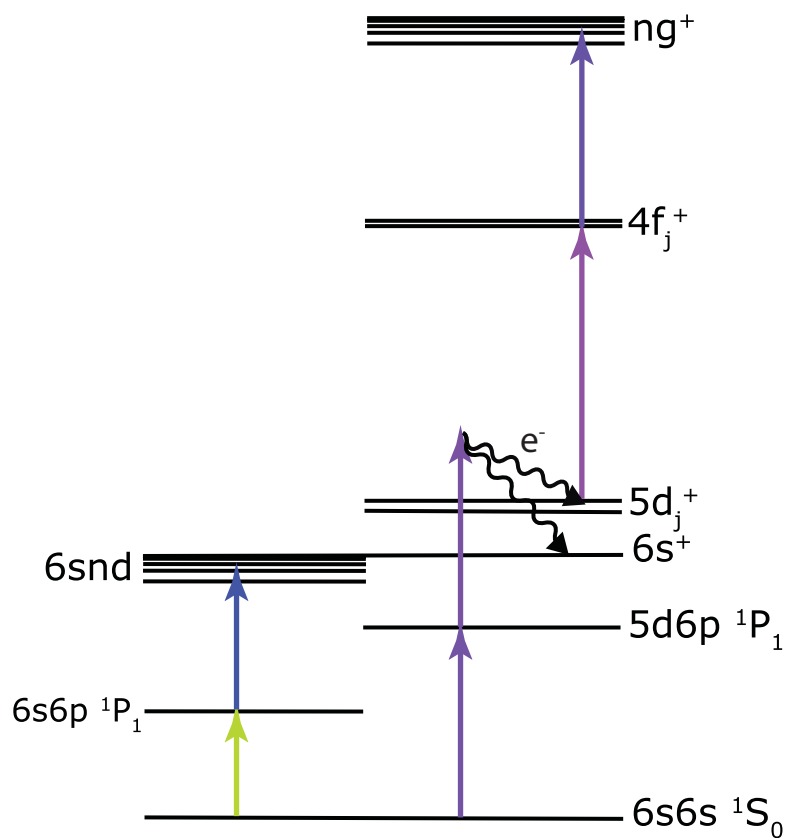


Figure 3.4: Excitation scheme for both $6snd$ neutral Rydberg states and ng^+ ionic Rydberg states.

resonance-enhanced ionization, through an intermediate $5d6p\ ^1P_1$ level, into the $6s^+$ and $5d_j^+$ continua. The 5 nsec, 350 nm, $\sim 50\ \mu\text{J}$ laser pulse is generated by frequency mixing, in a potassium dihydrogen phosphate (KDP) crystal, the output of a 522 nm pulsed dye laser with the 1064 nm fundamental of the Nd:YAG (YAG denotes Yttrium Aluminum Garnet) pump. A 300 fsec, 233 nm, $\sim 3\ \mu\text{J}$ pulse then excites $5d_{5/2}^+$ ions to the $4f_{7/2}^+$ level. This second laser pulse is generated by frequency mixing the 200 fsec 582 nm output of an optical parametric amplifier (OPA) with the 150 fsec, 390 nm OPA pump. The 390 nm pump is produced by frequency doubling a portion of the 100 fsec 780 nm Ti:Sapphire output in a 1 mm thick Beta Barium Borate (BBO) crystal. Lastly, a tunable, 5 nsec, 313 nm, $20\ \mu\text{J}$ laser pulse generated by frequency doubling (in KDP) the output of a 626 nm dye laser is used to excite Ba⁺ $4f_{7/2}$ ions into ng^+ Rydberg states. All lasers fire at a 15 Hz repetition rate, are linearly polarized in the same (vertical) direction, and are focussed into the atomic beam using a single 350 mm fused silica lens.

3.3.2 Results and discussion

Before presenting the experimental results, a brief overview of impulsive HCP ionization is given below.

Impulsive ionization

In the short pulse regime, where the duration of HCP is much less than the classical Kepler period of Rydberg electron,

$$\tau_{HCP} \ll \tau_K = 2\pi \frac{n^{*3}}{Z^2}, \quad (3.2)$$

where n^* is the effective principle quantum number, Z is the number of charges, τ_k is the classical Kepler period, the ionization of a Rydberg electron can be described by impulsive kick model [45]. The HCP gives the Rydberg electron a momentum kick or impulse

$$\vec{A} = - \int \vec{F}_{HCP}(t) dt \quad (3.3)$$

where $\vec{F}_{HCP}(t)$ is the time-dependent HCP field [38, 39, 45]. Consider a Rydberg electron with energy

$$E_0 = \frac{\vec{p}_0^2}{2} + V = -\frac{Z^2}{2n^{*2}} \quad (3.4)$$

, where \vec{p}_0 is the momentum of electron and V is the potential energy of the electron before the HCP. The Rydberg electron is then exposed to the HCP and the total energy of the electron becomes

$$E = \frac{(\vec{p}_0 + \vec{A})^2}{2} + V. \quad (3.5)$$

Since the electron does not move during the HCP under the impulsive approximation, its potential energy does not change during the HCP. Therefore, the total change in electron's energy change is

$$\Delta E = \vec{p}_0 \cdot \vec{A} + \frac{\vec{A}^2}{2}. \quad (3.6)$$

Ionization requires that this change is greater than the initial binding energy of the electron,

$$\Delta E > |E_0|. \quad (3.7)$$

Without loss of generality, we assume the HCP field is applied in the \hat{z} direction. We can then rewrite equation 3.7 in terms of the initial z-component of the momentum

of the electron

$$p_z > \frac{1}{A}(|E_0| - \frac{1}{2}A^2) \quad (3.8)$$

So ionization occurs when p_z is greater than a critical value

$$p_c = \frac{1}{A}(|E_0| - \frac{1}{2}A^2). \quad (3.9)$$

Quantum mechanically, the probability that the Rydberg atom is ionized by an impulse, A_z , is equal to the probability that $p_z > p_c$ at the instant of the pulse. Thus, in the short-pulse limit, the ionization yield v.s. impulse (or HCP field strength) can be obtained by integrating the electronic momentum-space probability distribution along the kick direction [45], i.e.

$$P(p_c) = \int_{p_c}^{\infty} \Psi(p)\Psi^*(p)dp. \quad (3.10)$$

Experimental results

In order to compare the HCP ionization of Rydberg ions with that of neutral Rydberg atoms, the ionization of Ba Rydberg ions/atoms with similar binding energy are measured in the same apparatus. Single ionization yields vs. GaAs bias-field for three different neutral Rydberg states, $6s30d$, $6s33d$, and $6s36d$ are displayed in Figure 3.5. Figure 3.6 presents the double ionization yields of $54g^+$ and $66g^+$ Rydberg ions along with the $6s30d$ and $6s36d$ curves showed in Fig.3.5. Both the single and double ionization data sets show the similar threshold behavior that has been observed for single ionization [35, 36, 38–40, 42] except that the signal to noise ratio in the double ionization measurements is significantly worse than the single ionization measurements. The ionization curves for the $6s36d$ and $66g^+$ states are

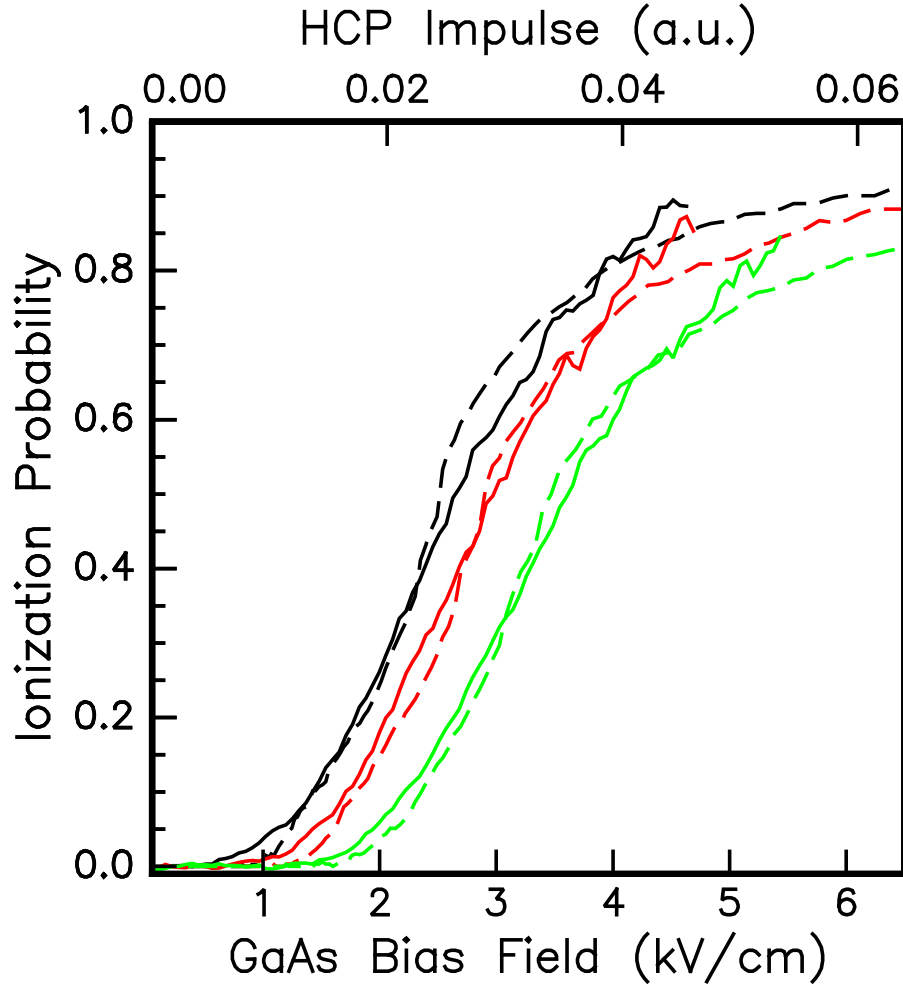


Figure 3.5: Measured HCP ionization probability as a function of GaAs bias field (bottom scale) and impulse (top scale) for $6s30d$ (green), $6s33d$ (red), and $6s36d$ (black) initial states. Solid Lines and Lower Horizontal scale: Measured HCP ionization probability vs. GaAs bias field for $6s30d$ (green), $6s33d$ (red), and $6s36d$ (black) initial states. Dashed Lines and Upper Horizontal Scale: HCP ionization probability vs. impulse curves for the same three initial states obtained from the numerical Classical Trajectory Monte Carlo (CTMC) simulation described in the text. Absolute ionization probability scales for the data are estimated by comparing fully saturated HCP ionization signal levels from higher-lying Rydberg states with signal levels obtained from standard, long-pulse field ionization. These initial estimates have been adjusted using a single multiplicative scale factor, 0.91, to achieve the best fit of experiment to the simulation.

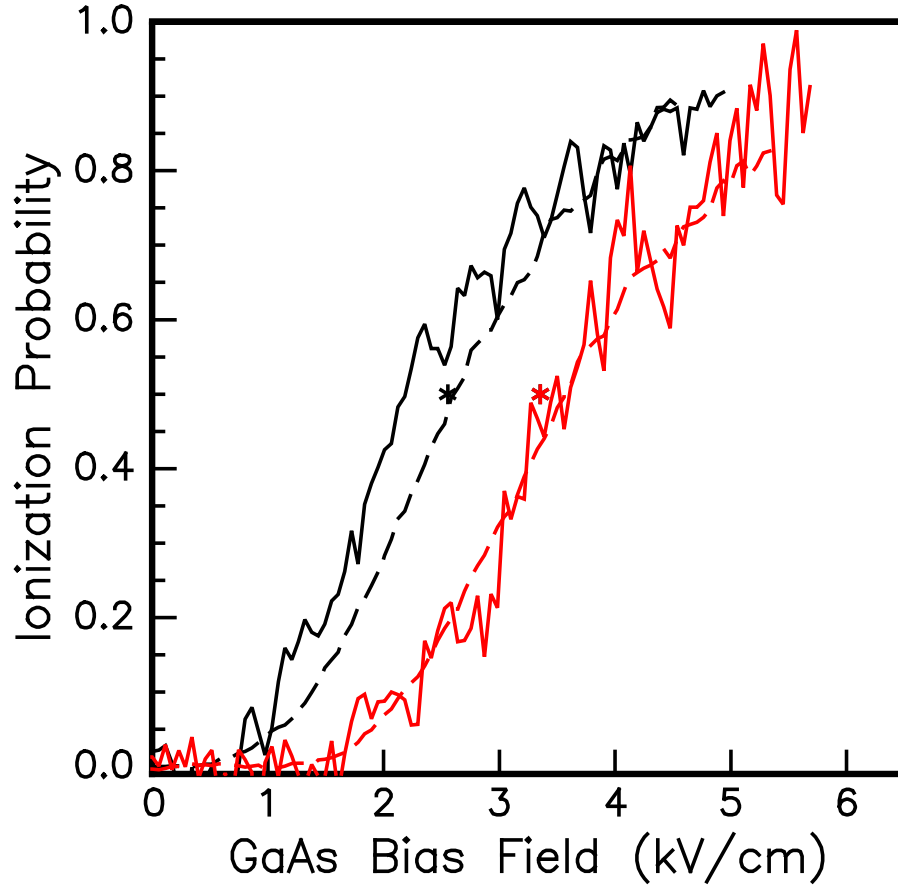


Figure 3.6: Comparison of measured HCP ionization probability vs. GaAs bias field curves for pairs of neutral (dashed lines) and ionic (solid lines) Rydberg states that have approximately the same binding energy. The $6s30d$ and $54g^+$ initial states are shown in red while the $6s36d$ and $66g^+$ levels are shown in black. The effective principal quantum numbers of the ionic states are approximately twice that of their neutral companions. The asterisks mark the predicted 50% ionization fields obtained from the impulsive ionization model described in the text and the impulse to bias field calibration derived from Fig. 3.5. Absolute ionization probability scales for the ion data are estimated by comparing saturated HCP ionization signal levels from higher lying Rydberg states with signal levels obtained from standard, long-pulse field ionization. These initial estimates have been adjusted using a single multiplicative scale factor, 0.89, to achieve the best match between the ionic and neutral data.

very similar and those for the $6s30d$ and $54g^+$ levels are essentially identical. This feature is related to the fact that the Rydberg levels in each neutral/ion pair have nearly the same binding energies, $E_0 = -\frac{Z^2}{2n^{*2}}$, where $n^* = n - \delta$ is the effective principal quantum number, δ is the quantum defect, and Z is the charge of the ion core. $\delta \simeq 2.7$ and 0.02 , for the $6snd$ and ng^+ series, respectively.

Discussion

For $l \ll n$, the momentum distributions of Rydberg states have rapid modulations. The momentum distributions averaged over rapid node-structure modulations are independent of n^* , l , and Z when plotted vs. scaled momentum, $p' = p_0\eta$, where $\eta = n^*/Z$. Thus, species characterized by the same value of η have equal probabilities that $p_0 > p_c$ for a given impulse, A . Consequently, in the low- l limit, the HCP ionization yield vs. impulse curves should be the same for ions with $Z = 2$, $n^* = 2N$ and neutral atoms with $Z = 1$, $n^* = N$. As shown in Fig. 3.6, our measurements support this prediction.

The momentum distributions of any bound Rydberg state is symmetric about $p = 0$ along any axis regardless of the value of angular momentum. Therefore, according Eqn. 3.10, the ionization probability is always 50% for a critical momentum $p_c = 0$ along the kick axis. The corresponding impulse $A_{1/2}$ is then

$$A_{1/2} = \sqrt{2E_0} = 1/\eta, \quad (3.11)$$

obtained by setting $p_c = 0$ in Eq. 3.9, which only depends on the parameter η . In Fig. 3.6, the corresponding Rydberg ionic states and neutral states pairs have similar η ($Z = 2$, $n^* = 2N$ and $Z = 1$, $n^* = N$). The same impulse that doubly-ionizes a Rydberg ion with 50% probability, will also ionize a neutral Rydberg atom with same

Table 3.1: Measured: predicted impulse ratios for ionization of ng^+ Rydberg ions with 20% and 50% probability. The three columns correspond to predictions obtained from i) HCP ionization measurements of neutral atoms with the same effective binding energy; ii) the impulse model; and iii) the CTMC simulation. Statistical errors in the ratios, due primarily to the relatively poor signal to noise ratio in the double ionization measurements, are roughly 5% .

	% Ion.	Neutral Expt.	Impulse model	CTMC
$54g^+$	20%	0.84	-	0.86
	50%	0.88	0.91	0.93
$60g^+$	20%	0.86	-	0.84
	50%	0.87	0.89	0.91
$66g^+$	20%	1.03	-	1.11
	50%	0.97	1.04	1.06

η in the similar way. The data shows the reasonable agreement in this argument.

In the experiments, the single/double ions are detected using a field ionization pulse which pushes them onto the MCP detector. Very high-lying Rydberg states produced by the HCP may be ionized by this extraction field, F_{ex} . Therefore, the field pulse effectively lowers the continuum to a binding energy $E_c = \frac{3}{2}\sqrt{ZF_{ex}}$. If diabatic field ionization in the rapid, ~ 50 nsec rising time of the extraction pulse is assumed [15]. Direct comparison between the experimental data and the predictions of the impulsive ionization model (see Figs. 3.5 and 3.6 and Table 3.1) requires that we replace E_0 in the expressions for p_c and $A_{1/2}$ with an effective binding energy, $E' = E_0 + E_c$. In the experiment, $F = 48$ V/cm for neutral ($Z=1$) Rydberg atoms and $F = 24$ V/cm for Rydberg ions ($Z=2$) so that $E_c \simeq 32\text{cm}^{-1}$ in both cases.

Our data are also compared to the results of Classical Trajectory Monte Carlo (CTMC) simulations which have been described in detail previously [35,40,45,46,55]. Briefly, the Rydberg states are prepared as an ensemble of classical particles with the

same energy and angular momentum. The electrons in the ensemble are distributed with different positions and momenta in a pure Coulomb potential, $-Z/r$. The motion of electrons before, during and after exposure to a 0.8 psec (FWHM) Gaussian HCP are tracked by numerically integrating the classical equations of motion. For a given HCP field, the ionization probability is determined by the fraction of electrons in the CTMC ensemble whose energies (following the HCP) are greater than the effective ionization threshold, $-E_c \simeq -32cm^{-1}$. Previous investigations with neutral Rydberg atoms have shown that experimental HCP fields (or impulses) can be calibrated using CTMC simulations [41,42]. Thus, the constant factor between the upper and lower field scales in Fig. 3.5, 0.0098 (a.u.)/(kV/cm), is used to calibrate the HCP impulse delivered to Rydberg ions for a given bias field. This calibration factor is used in Fig. 3.6 and in Table 3.1 to compare the measured double ionization yields with results of the impulsive ionization model and the CTMC simulation. However, it is worth emphasizing that no calibration factor is required to directly compare the single and double ionization data (see Fig. 3.6).

3.4 Summary

In this chapter, HCP ionization of Rydberg ions has been explored for the first time. The measured double ionization yields for Ba ng^+ ions are found to be in reasonable agreement with the predictions of an impulsive ionization model and CTMC simulations. We note that the classical Kepler period can be written, $\tau_K = 2\pi Z\eta^3$. Thus, τ_K increases in proportion to Z , and the impulse approximation should improve with increasing ion charge for fixed η . Therefore, the understandings of HCP ionization for Rydberg atoms can be applied to the investigation of Rydberg ions,

particularly to our double Rydberg wave packets experiments, when the duration of the HCP is less than the Kepler period of Rydberg wave packets.

Chapter 4

Measurement of the Quantum State of Ionic Wave Packets using HCP

4.1 Introduction

Wave packets are non-stationary, spatially localized quantum systems in atomic physics [11]. They connect quantum mechanics and classical mechanics and can help us to deepen our understanding of quantum physics. The unique time-dependent properties of wave packets make them a preferred candidate for studying time-dependent interactions in atomic physics including collisions between atoms or charged particles, the collisions between electrons within multielectron atoms or the response of electrons to a laser field [11]. The understanding of these problems can be obtained by monitoring the evolution of wave packets. To reach our goal of viewing time-dependent energy exchange in doubly excited wave packets, we must first be able to

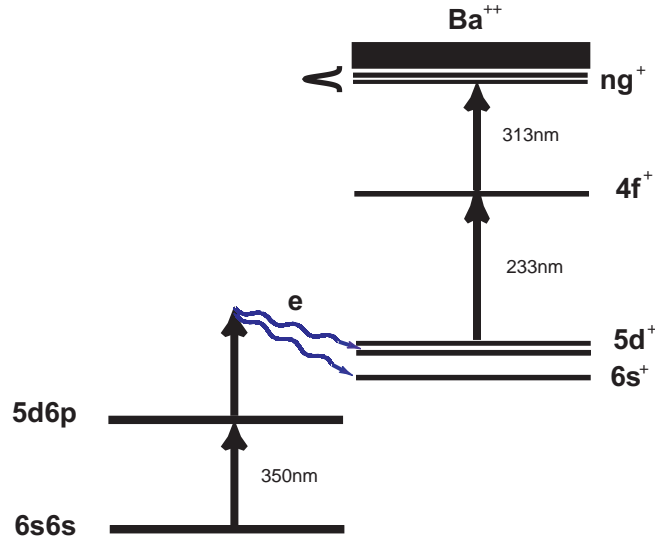


Figure 4.1: Laser excitation scheme for producing an ionic ng^+ Rydberg wave packet.

characterize the wave packets launched into Ba^+ and Ba^{++} potential, respectively. Following the investigation of the impulsive ionization of ionic Rydberg states in the previous chapter, we examine the evolution of ionic wave packets using HCP as a probe.

4.2 Experimental procedure

The experiments described here use a nearly identical set up as that detailed in the previous chapter (Fig. 3.3). The only notable difference is the use of a short pulse laser to excite a coherent superposition of, rather than single, ng^+ eigenstates. Specifically, a ~ 500 fsec, 313nm pulse is used to excite Ba^+ $4f_{7/2}$ ions into ng^+ Rydberg wave packets. This laser pulse is generated by frequency mixing the 200 fsec ~ 524 nm pulses from an OPA with the 100 fsec 780 nm Ti: Sapphire output in a 1 mm thick BBO crystal. Then, the wave packet is exposed to HCP. The double ions are collected by a 2400V/cm field pulse about 50ns after the HCP. The double

ionization is recorded as a function of time delay between HCP and the excitation of the ionic wave packet.

4.3 Results and discussion

The double ionization signal as a function of delay between the HCP pulse and the launch of the ionic wave packet is shown in Fig. 4.2. As we discussed in the previous chapter, the HCP acts as a momentum kick on the atoms under the impulsive approximation. The ionization yield is the integral of the electronic momentum-space probability distribution along the kick direction [45], i.e.

$$P(p_c) = \int_{p_c}^{\infty} \Psi(p)\Psi^*(p)dp, \quad (4.1)$$

where p_c is the critical momentum along the kick direction that is required for ionization. As defined in chapter 3, p_c is determined by HCP strength, A , and the electron binding energy.

As a wave packet evolves, its momentum distribution changes as well (Fig 4.3). For a specific HCP impulse, \vec{A} , and time, t , the HCP ionization probability reflects the probability that the wave packet has a momentum greater than the critical momentum, p_c , at that instant.

The wave packet double ionization signal versus time delay between the HCP and the excitation laser pulses in Fig 4.2 reveals the motion of the wave packet. This particular wave packet has a Kepler orbit time of ~ 2.3 psec and the HCP ionization probability is less than 50%. As indicated in Fig. 4.3, for weak kicks, p_c is large and the HCP ionization probability is significant only if the wave packet is very close to the ion core where it has a large momentum. At early times, before the wave

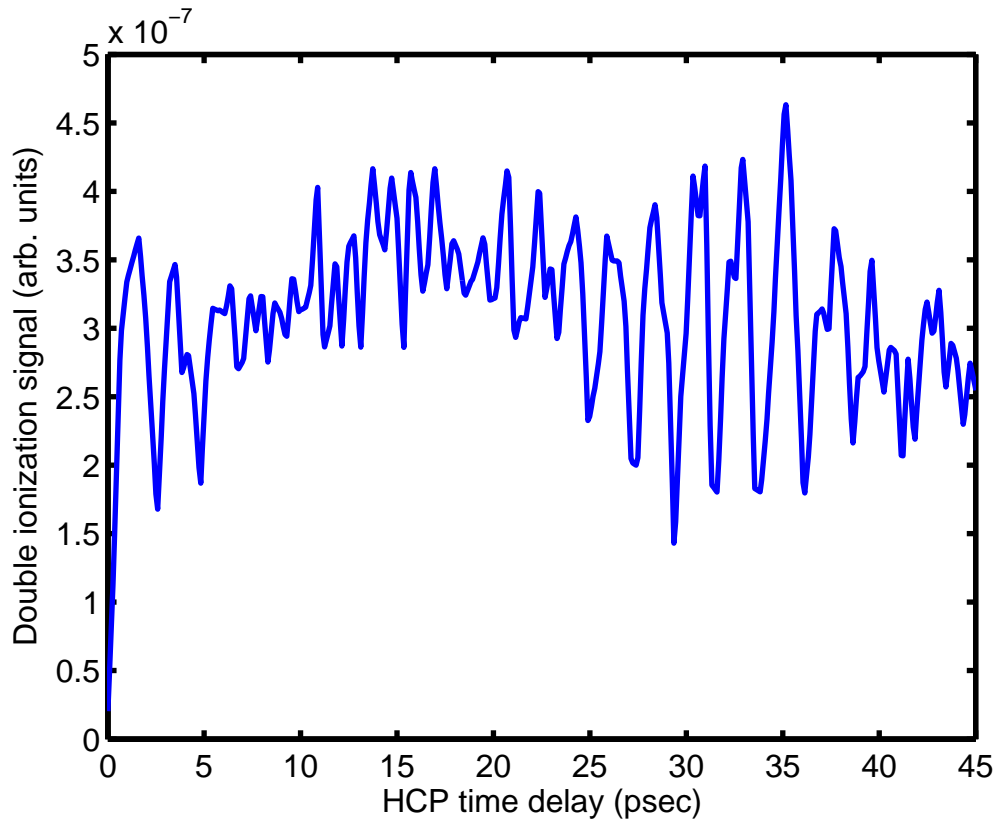


Figure 4.2: Double ionization signal as a function of delay between HCP probe and the laser excitation of an ionic wave packet with an average principal quantum number, $n \sim 38$. The ionization probability here is $< 50\%$.

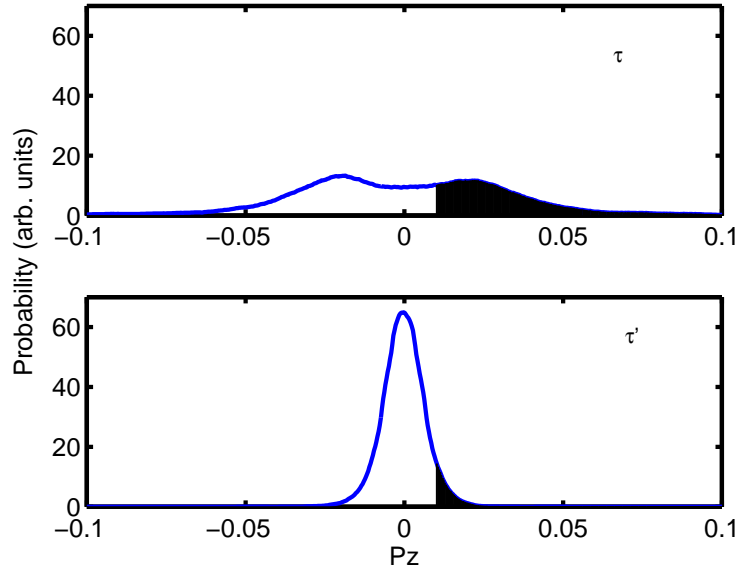


Figure 4.3: A schematic diagram of the fraction of wave packet is ionized [56]. Here, $p_c = 0.01$ and shaded region represents the fraction of ionization probabilities at two different time (a) τ and (b) τ' , where $\tau' > \tau$.

packet is created, there is no double ionization. Double ionization becomes possible when the exciting pulse and the HCP arrive at interaction region simultaneously. This signal then increases to a maximum and begins to decrease, suggesting that the momentum of wave packet decreases as it moves away from the core region. In the quantum picture, the wave packet is initially localized near the core, where it has a broad momentum distribution. Thus, as indicated in 4.3, the ionization probability of the wave packet is significant. As the wave packet moves toward the outer turning point of its classical orbit, the momentum distribution narrows. Thus, the ionization probability of the wave packet decreases. After about 2.3 psec, i.e. one classical Kepler period later, the wave packet returns to the core, resulting in a high ionization probability. Due to the anharmonic Rydberg energy level structure, the wave packet disperses in about two periods. The double ionization signal damps as the wave

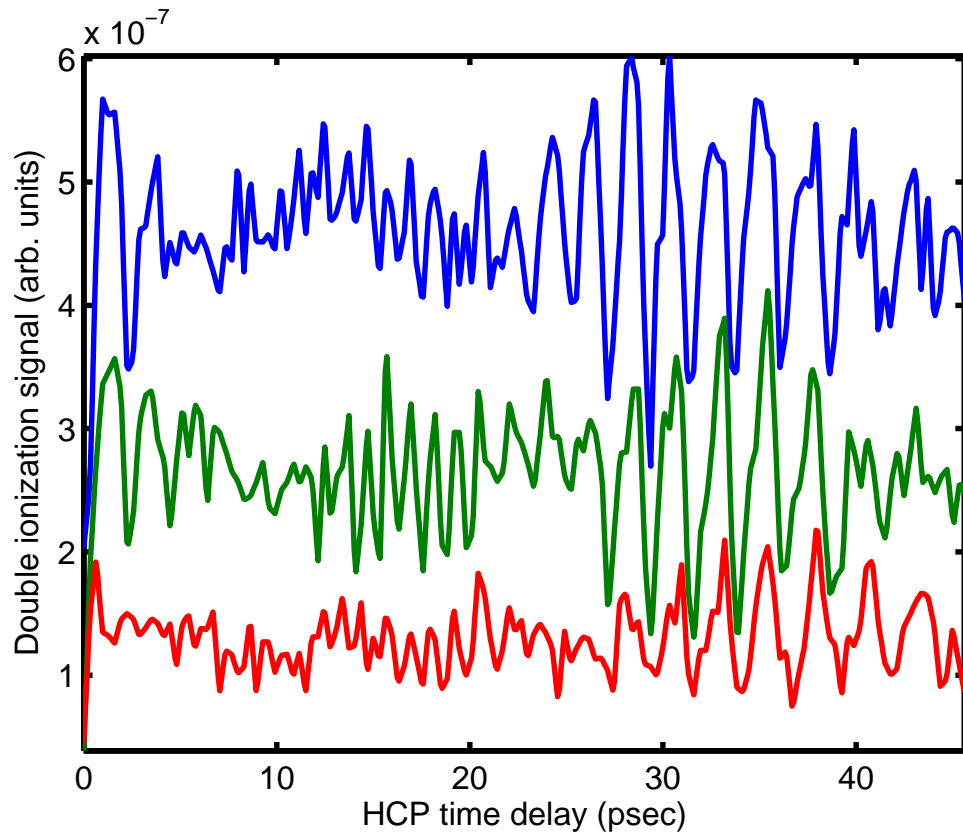


Figure 4.4: Double ionization signal of ionic wave packet for different HCP strengths. The HCP strength increases from red to green to blue. The blue curve is shifted up by 2×10^{-7} in order to be distinguished from the green one.

packet disperses and reappears as the wave packet revives after about 22 psec [58,59]. During this integer revival, the constituent states of the wave packet are in phase again.

If the HCP kick is too weak to detect the lower constituent n states, the measured characteristics of the wave packet do not represent that of the actual ionic wave packet. This will hinder the understanding of the double wave packet experiments. Therefore, we measured the double ionization probabilities of the same ionic wave packets using different HCP strengths. Fig. 4.4 shows the double ionization signals for three different HCP kick strengths. The HCP ionization probabilities are less than 50% for the three measurements. The limitation of applicable high voltages across the wafter prevents us from measuring the double ionization probabilities $> 50\%$. A clear phase shift in the signal modulations can be seen. This is the consequence of the different critical momenta, p_c , for different \vec{A} (Eqn. 3.9). As the strength of the HCP increases, the signal contributed by lower Rydberg states increases. This leads to a slight decrease in the wave packet period represented as shifts in Fig. 4.4.

4.3.1 Complex phase-retrieval method

From the double ionization probabilities, the constituent states and their relative phase information can be obtained by a complex phase-retrieval method [57]. The wave packet is the superposition of many real eigenstates $\psi_j(\vec{p})$ with energies E_j and constant phases ϕ_j . In the momentum space and in the absence of any external interactions [57],

$$\Psi(\vec{p}, t) = \sum_j C_j \psi_j(\vec{p}) e^{-i(E_j t + \phi_j)} \quad (4.2)$$

where the C_j are the real, time-independent amplitudes. The time-dependent probability distribution is then

$$P(\vec{p}, t) = |\Psi(\vec{p}, t)|^2 = \sum_{j,k} C_j C_k \psi_j(\vec{p}) \psi_k(\vec{p}) e^{-i[(E_k - E_j)t + (\phi_k - \phi_j)]}. \quad (4.3)$$

The Fourier transform, $S(\vec{p}, \Delta E)$, of this time-dependent probability, $P(\vec{p}, t)$, can be used to extract the amplitudes of each eigenstates, C_j , and the phase difference $\Delta\phi_{kj} = (\phi_k - \phi_j)$ between any two constituent eigenstates [57], where $\Delta E = E_k - E_j$. The amplitudes of states can be obtained by utilizing the proportionality of the ratio of any two amplitudes of two eigenstates, $\frac{C_j C_i}{C_i C_k} = \frac{C_j}{C_k}$, with that of corresponding amplitudes of fourier transform $\frac{S(\vec{p}, \Delta E_{ji})}{S(\vec{p}, \Delta E_{ik})}$ and the normalization $\sum_k |C_k|^2 = 1$. Fig. 4.6 shows the Fourier transform of the double ionization probabilities for a range of HCP kicks from weak(1) to strong(8). The weak HCP kick can not detect the low n states in the ionic wave packet. By increasing the strength of HCP, the contribution of the low n states to the double ionization probability emerges. As noted above, this results in the phase shift observed in the double ionization yields shown in Fig 4.4.

The average phase and amplitudes of the constituent eigenstates in the $38g^+$ ionic radial wave packet can be extracted from the Fourier transform of measured time-dependent probability distribution (Fig. 4.6). In Fig. 4.7, the extracted information is separated into to low and high HCP kicks. The blue color denotes the lower HCP kick, specifically the data sets of 3 and 4 in Fig. 4.6. The red color corresponds to the highest two HCP kicks in the experiment. We group them separately as a check of the independence of the recovered amplitudes and phases on the HCP amplitudes. The difference of the HCP strength in each group is insignificant compared to that between low/high HCP kicks groups. The error bars in Fig. 4.7 represent the standard

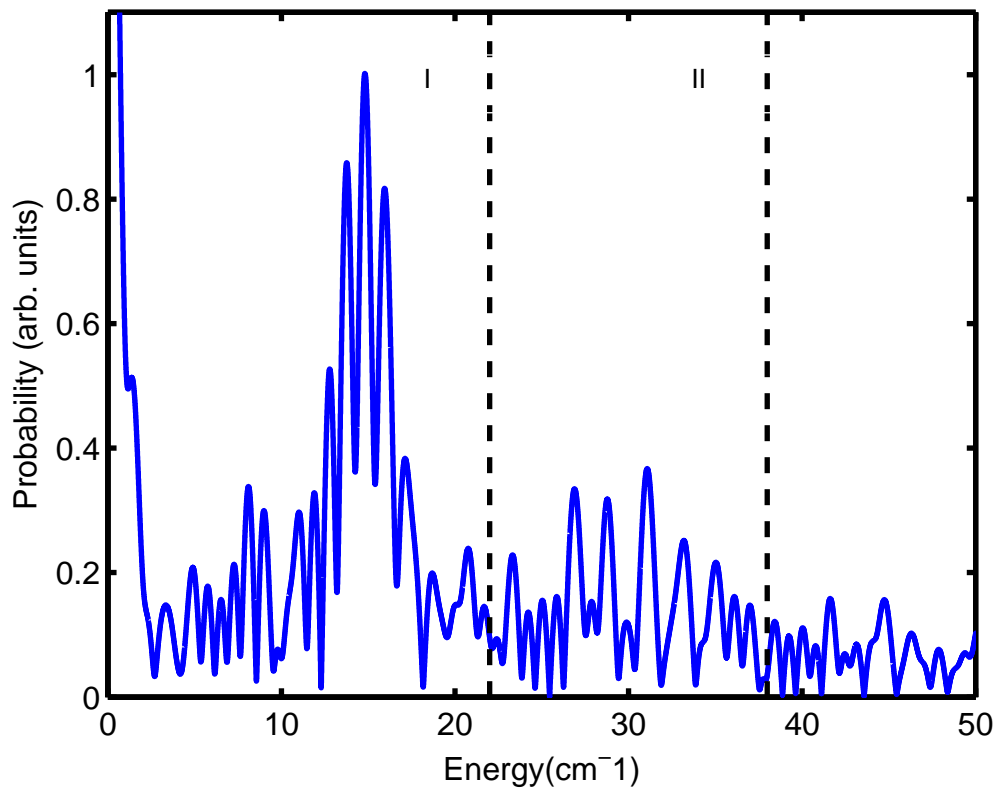


Figure 4.5: Discrete Fourier Transform of data shown in Fig.4.2. The vertical dashed lines separate regions I, II, which indicates energy splitting between ng^+ levels with $\Delta n = 1, 2$, respectively.

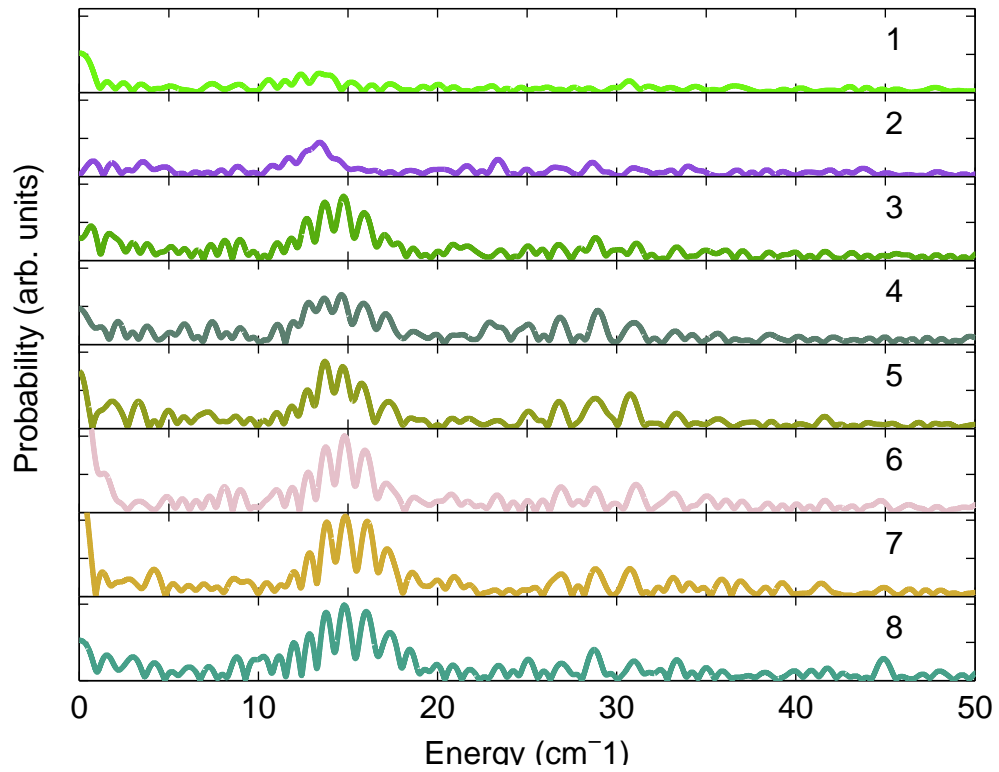


Figure 4.6: Discrete Fourier Transform of double ionization probabilities using different HCP kicks. The strength of the HCP kicks increases from top to bottom, but all the double ionization probabilities are less than 50%.

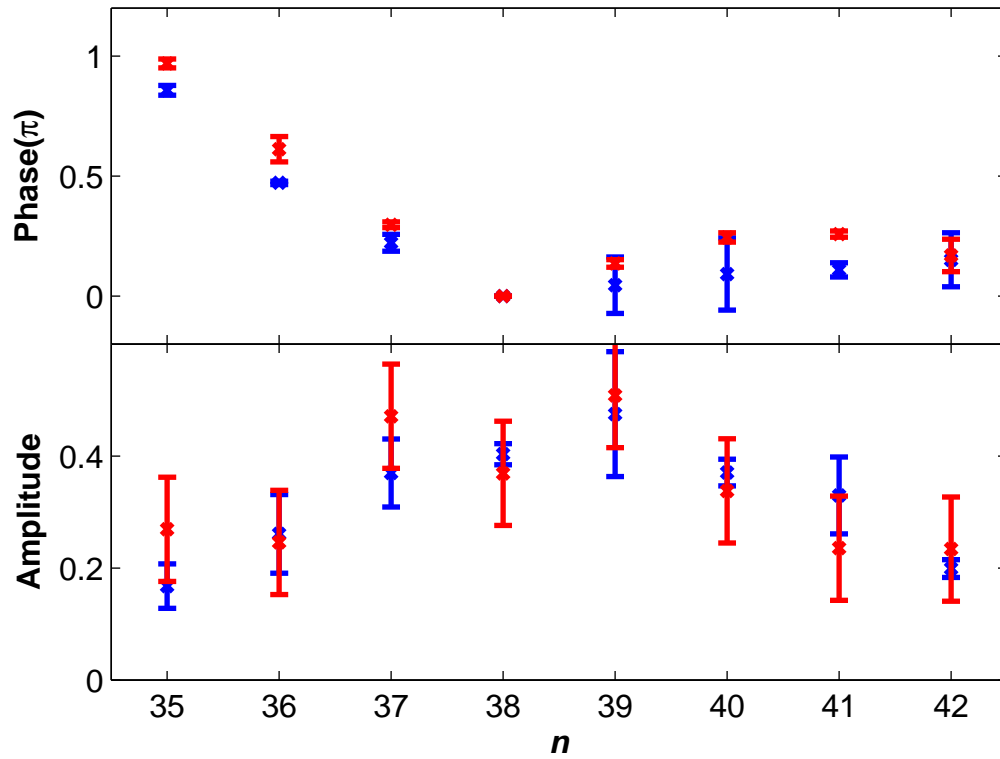


Figure 4.7: Measured amplitudes and phases of constituent eigenstates in a ng^+ ionic radial wave packet in Barium for low HCP strength (blue cross) and high HCP strength (red circle). Both amplitudes and phases were obtained from the Fourier transform of probability distribution measured by HCP. Since only the phase difference can be extracted, we define the phase of the $38g^+$ eigenstate to be zero.

error of the mean for two different data sets in each group. As shown in Fig. 4.6, the same constituent states are observed in both cases, and the amplitudes obtained from the complex phase-retrieval method are almost identical within measurement. The observed phase variation across the constituent states is the expected results of the frequencies chirp of the excitation laser due to its passage through various optical elements on route to the experiment.

Once the phases and amplitudes of constituent eigenstates are determined through the complex phase-retrieval method, they can be used to reconstruct the evolution of ionic wave packets. The recovered ionic wave packet distributions in coordinate and momentum space are shown in Fig 4.8. The time evolution of these distributions is consistent with the signal variation in Fig 4.2.

4.4 Summary

In this chapter, we have demonstrated for the first time that the time-dependent probability distribution of the ng^+ ionic wave packets can be measured by using HCP ionization. The collapse and revival characteristics of ionic wave packets are observed. Finally, the quantum states of ionic wave packets are determined by the complex phase-retrieval method. Accurate characterization of these ionic wave packets is critical for probing double Rydberg wave packets as described in next chapter.

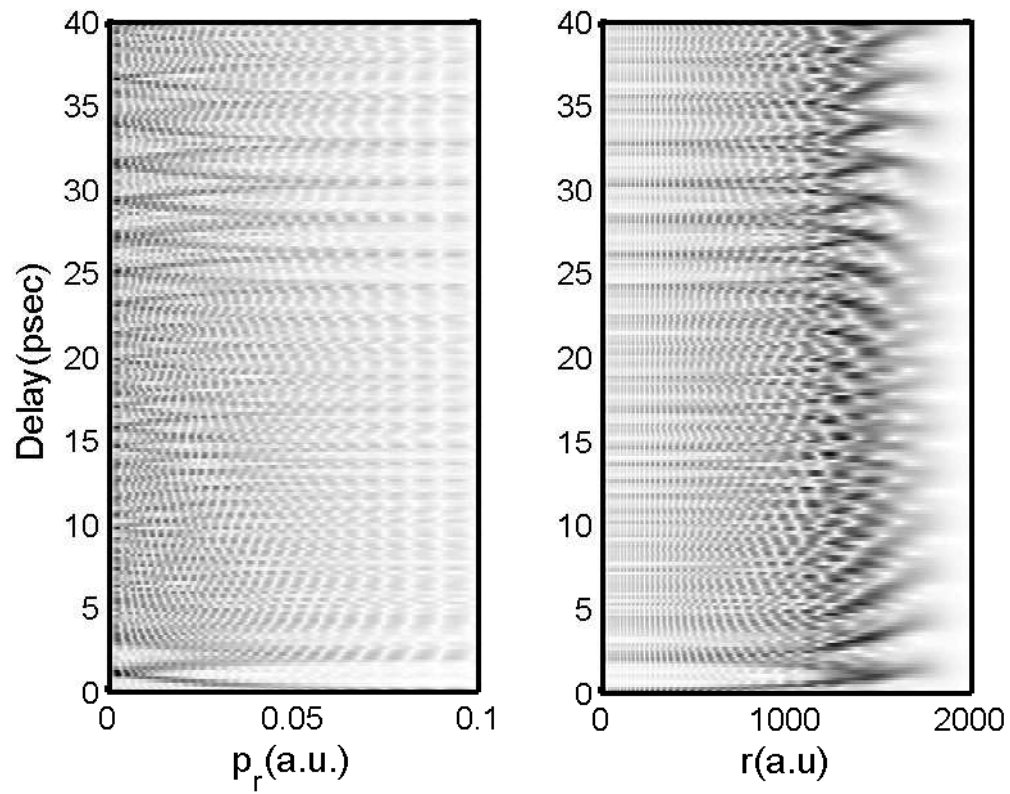


Figure 4.8: Density plots of recovered time-dependent probability distribution for the ng^+ ionic wave packet described by Fig.4.7 in both coordinate and momentum space. Dark denotes high probability regions.

Chapter 5

Time-Resolved Energy Exchange Between Electrons in Double Rydberg Wave Packets

5.1 Introduction

The interaction between electrons in two-electron atoms results in complex dynamics reflected by a rich excitation spectrum. There are various arrangements of the two electrons in such atoms, and these are commonly referred to as configurations. For example, one electron can be in the ground state while the other electron is in an excited state. This situation is similar to a one electron atom even though there are two valence electrons. Another possibility is that both electrons are in highly excited states. In this case, many configurations are accessible to the two electrons, and transitions between configurations result in interesting dynamics.

Many theoretical works have been conducted to investigate the two-electron sys-

tems using both classical and quantum theories [1,66]. Experimentalists are also trying to study various aspects of two-electron atom systems [7, 8, 10, 49, 50]. However, most previous experiments were focused on relatively simple configurations, where one electron is in a high Rydberg state while the other one is in the ground state or a low excited state. Furthermore, the majority of these experiments utilized frequency resolved spectroscopy at energies well below the double ionization limit. Here, there are typically only a handful of coupled configurations and the energy levels can be resolved spectroscopically. A few time-dependent experiments have focused on the perturbation of the evolution of neutral wave packets due to the excitation of a second tightly bound electron [10].

A few experiments have utilized frequency domain spectroscopy to search for evidence of long-lived doubly excited states near the double ionization threshold [8]. However, these failed to identify any structure at energies where, in an independent particle picture, the two electrons would occupy orbits of comparable size. With the advance of well controlled sub-picosecond lasers, electronic wave packets with controlled probability distributions can be produced in highly-excited Rydberg atoms [11]. Thus, it is possible using wave packets to investigate time-dependent electronic dynamics within a two-electron atom near the double ionization limit, where the traditional frequency spectroscopy becomes useless due to the high density of energy levels. Many theoretical investigations place the electrons in specific configurations, then study the stability of these configurations [66,67]. Similarly, with controlled wave packets, we can now perform experiments where electrons are placed in well-defined initial configurations, and attempt to watch the change of configurations over time in laboratory. Recently, the first time domain experiment near the double ionization limit was conducted using a series of short laser pulses to produce double electronic

wave packets where the initial positions, energies and angular momenta of the two-electrons were precisely controlled [49, 50]. That experiment used the distribution of final ionic states following the autoionization of double Rydberg wave packets to infer the two-electron dynamics. The measurements indicated that energy exchange between two electrons does not occur gradually. Instead, nearly instant ionization occurs when the electrons collide with sufficient momenta so that one is knocked off the atom. The radius where the two electrons meet is an important parameter in determining the energy exchange and the distribution of final ionic states [49]. However, prior to the work reported here, no direct time-dependent measurement of electron correlation near the double ionization limit had been conducted.

The sub-picosecond, unipolar HCP, as described in chapter 3, can provide a time-sensitive probe to investigate the two-electron dynamics in more detail. Following the discussion of the impulsive ionization of ionic states and the characterization of ionic wave packets by HCP in the previous two chapters, we now describe an experiment to investigate the time-dependent exchange of energy between double Rydberg wave packets using HCPs.

5.2 Experimental procedure

This experiment is performed using the same basic setup described in the previous chapters (Fig. 5.1). The excitation scheme for producing double Rydberg wave packets is shown in Fig. 5.2. Instead of using resonant two-photon ionization of Ba atoms to produce Ba^+ ions (as described in chapter 3 and chapter 4), we first excite one valence electron into a wave packet.

The two laser pulses excite Ba atoms from the $6s^2$ ground state through $5d6p\ ^1P_1$

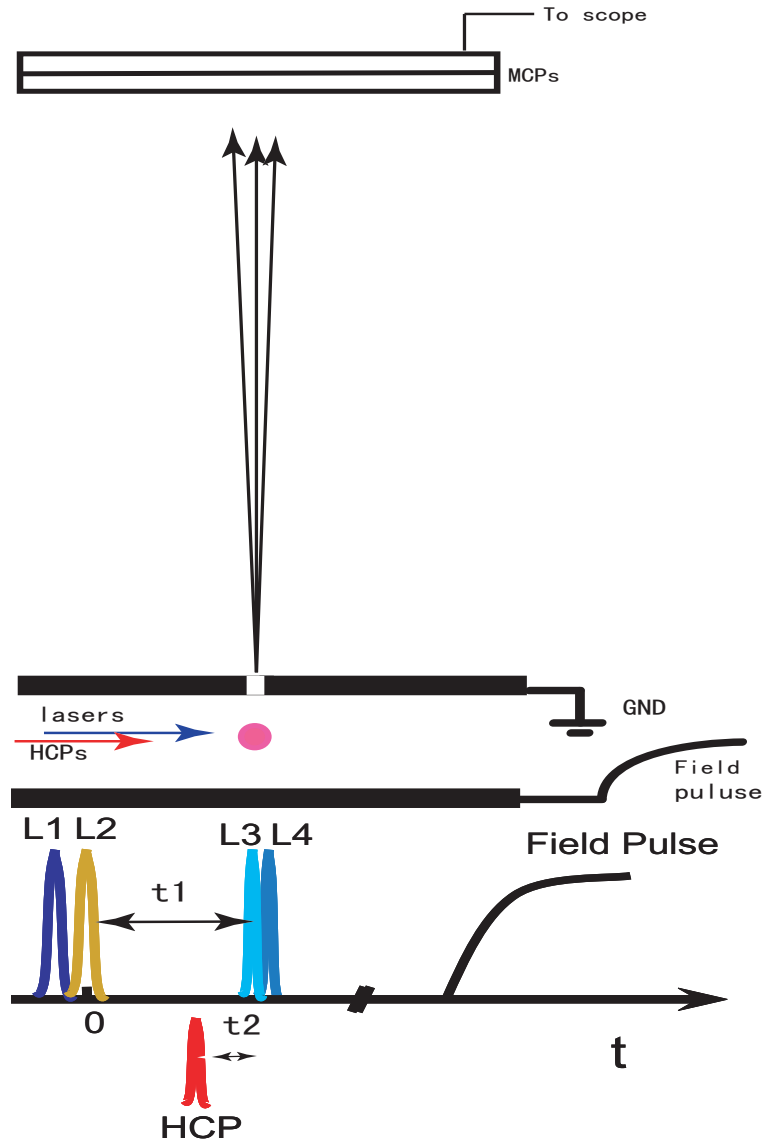


Figure 5.1: Schematic of the experimental setup and the time sequence of laser excitations, HCP, and field ionization pulse. All the laser pulses and HCP are pointed from the same side. The angle between the HCP and the excitation lasers is $\sim 40^\circ$. The 2mm diameter extraction hole and the angle results in a time resolution, ~ 0.8 psec for the experiments. This is comparable to the duration of HCP or the excitation lasers. Therefore, the time resolution of the experiment is ~ 1 psec. The time t_1 between L2 and L3+L4, is adjusted to control the relative phase of the wave packets. A field pulse with a $50ns$ rise time pushes single/double charged ions into the detector several 10's of nanoseconds after the lasers and HCP.

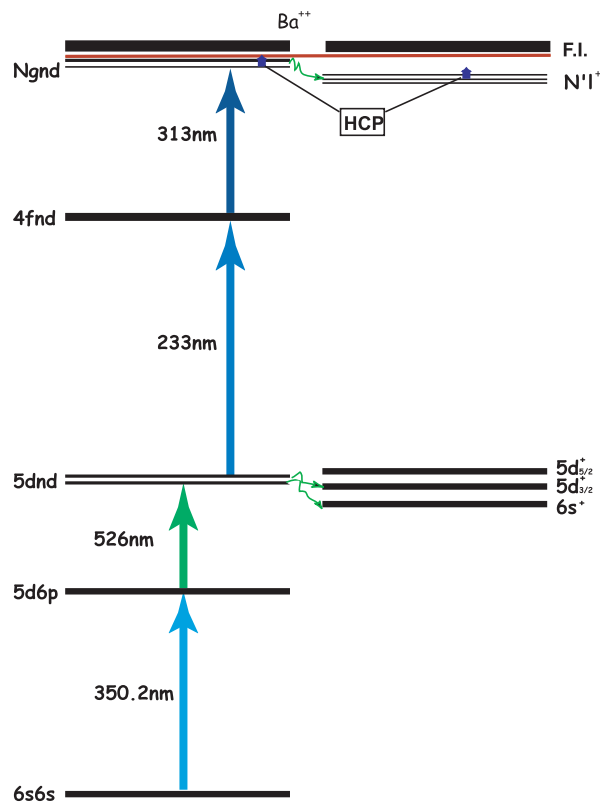


Figure 5.2: Laser excitation scheme of double Rydberg wave packets. The related ionic states are plotted side by side. The green curved arrows show the possible autoionization paths from double excited states to nearby ionic states or continua.

level, forming a $5d_{5/2}nd$ wave packet. First, a 350 nm dye laser pulse promotes Ba atoms from the $6s^2$ ground state into an intermediate $5d6p\ ^1P_1$ level. Then a sub-picosecond laser pulse from an OPA tuned to ~ 526 nm creates a $5d_{5/2}nd$ wave packet with average principal quantum number $n \sim 25$, maximum orbital radius $R_1 \approx 66nm$, and classical Kepler period $\tau_1 \approx 2.3psec$. This is referred to as the “neutral” wave packet. At some time later, another two-step laser excitation promotes the inner valence electron, creating a second, “ionic”, wave packet via the isolated core excitation (ICE) method [68]. These two laser pulses are identical to those used to excite Ng^+ ionic wave packets as described in previous chapter, where $N \approx 38$, the maximum radius $R_2 \approx 76nm$ and classical Kepler period $\tau_1 \approx 2.1psec$. The delay between L3 and L4 is fixed in the experiment while the delay between L2 and L3 is controlled using a translation stage. We vary the time delay between the excitation of two wave packets to control the initial relative radial position of the two wave packets.

The double $Ngnd$ Rydberg wave packets can decay via autoionization into a range of $N'l^+$ Rydberg states. Prior to autoionization, the electrons may exchange energy and angular momenta as the wave packets evolve. We expect that the rate at which these processes occur depends on the relative positions of the electrons and the nucleus. Our goal is to monitor this evolution through HCP double ionization. At some time after L2, the atoms are exposed to a HCP whose duration is about 0.6 psec [34]. A $\sim 2400V/cm$ clearing field pulse applied to the interaction region approximately 50 nsec after the HCP pushes single and double ions to the microchannel plate detector. This clearing pulse ionizes highly excited Ba^+ Rydberg states to Ba^{++} . The minimum values of N' for which electrons can be ionized to Ba^{++} are $N' \simeq 32$ or $N' \simeq 37$ for adiabatic and diabatic field ionization respectively [15].

We note that the field pulse has sufficient magnitude to ionize both the $n \approx 25$ neutral wave packet as well as the $N \approx 38$ ionic wave packet. Thus, in the absence of any time dependent interaction between the electrons, the double Rydberg wave packets would be converted to Ba^{++} ions with 100% efficiency. However, because of electron-electron interactions, if the wave packets are left to evolve without further external influence, we observe very little double ionization signal at any delay between the two wave packets. This is because autoionization occurs prior to the clearing pulse. During autoionization, one electron typically becomes sufficiently bound in the Ba^{++} potential such that the ion clearing pulse is no longer sufficient to ionize it. For example, an $n \approx 25$ neutral electron is bound by $E_b = 175cm^{-1}$ and at least this much energy must be supplied by the second electron for autoionization to occur. Extracting this minimum energy from an $N \approx 38$ ionic wave packet reduces its principle quantum number to $N' \approx 30$ which is below threshold for adiabatic or diabatic field ionization.

Using a HCP, we can inject additional energy and momentum into the system before, during and after any interaction between the electrons. The effectiveness of the HCP in doubly ionizing the atoms directly, or in creating final ionic states that can be ionized by the clearing pulse depends on how much energy is exchanged between the electrons and whether these “collisions” occur before, during or after the HCP. Thus, the HCP provides a time resolved probe of the electron-electron interaction in the double Rydberg wave packet. The HCP strength is fixed at $\sim 7500V/cm$, which produces less than 50% direct ionization for both wave packets if there is no extracting pulse. The two-electron dynamics are monitored through the double ionization yields as the HCP delay, t_2 , relative to the excitation of the second wave packet, is scanned. The double ionization signal vs. t_2 is recorded for select values of t_1 to study the

effect of varying the initial positions and velocities of the two wave packets on the two-electron dynamics.

5.3 Results and discussion

We consider two distinct situations depending on whether the HCP arrives earlier or later than L3 and L4, i.e. the creation of the ionic wave packet. When the HCP arrives in the interaction region after the creation of both neutral and ionic wave packets, the double ionization signal reveals the correlated dynamics of the two electrons. However, if the excited atoms are exposed to the HCP before the ionic wave packet excitation, the double ionization signal reflects the evolution of the first wave packet.

5.3.1 Characterization of $5dnd$ autoionizing wave packets

The total energy of the two electrons in the $5d_{5/2}nd$ neutral wave packet is above the $6s^+$ and $5d_{3/2}^+$ ionization limits of neutral Ba atoms, but below the $5d_{5/2}^+$ ionization limit as illustrated in Fig. 5.2. Therefore, the two electrons can redistribute their energies by a collision process, autoionization. One electron provides energy to the other, resulting in a 0.1eV or 0.7eV free electron and a $6s^+$ or $5d_{3/2}^+$ ion respectively. This autoionization results in a maximum useful delay between the launch of the first and the second wave packets to less than two Kepler periods or so. Moreover, when investigating the changes in the double ionization yields as a function of launch delay for the second wave packet, it is necessary to account for the delay dependent variation in the first wave packet population.

In the previous chapter, we described a method for characterizing the ionic wave

packet used in the double Rydberg wave packet experiments. Viewing the HCP double ionization yield prior to the excitation of the ionic wave packet allows us to characterize the neutral wave packet as well. A momentum kick from the HCP can deliver energy to the $5d_{5/2}nd$ wave packet making the total electronic energy greater than the $5d_{5/2}^+$ ionization limit. For strong HCP kicks, the number of $5d_{5/2}^+$ ions produced by the HCP is proportional to the initial population of the $5d_{5/2}nd$ wave packet. Following the HCP, the 233 nm (L3) and 313nm (L4) lasers excite $5d_{5/2}^+$ ions through $4f_{7/2}^+$ intermediate state into Ng^+ ionic states. The 2400V/cm field pulse is then used to collect ions.

We note that for the HCP strengths used, the neutral $5d_{5/2}nd$ wave packet ionization probability is less than 100% and is time dependent due to the evolving momentum distribution of the wave packets. However, substantial energy exchange between the electron and HCP results in further excitation of the electron. Thus, even if the electron is still bound when the second wave packet is excited, autoionization of the double Rydberg wave packet should result in the population of Ba^+ ions that are further ionized by the clearing pulse. However, if autoionization of the $5d_{5/2}nd$ wave packet occurs prior to the HCP, no ionic excitation can occur and there is no Ba^{++} signal. Thus, the time-dependent double ionization signal is proportional to the survival probability of the $5d_{5/2}nd$ neutral wave packet as a function of time.

Fig. 5.3 shows the double ion yield from a $5d_{5/2}nd$ autoionizing wave packet, where the average effective principal quantum number of the wave packet is $n \sim 25$. Our measurement can be compared with the result of a two-channel quantum defect theory calculation [60–62]. Discrete steps with period about 2.3 psec are visible in the double ionization probability. The steps are due to the time-dependent autoionization rate as the Rydberg electron moves near and away from the excited ion-core.

The $5d_{5/2}nd$ autoionizing radial wave packet can be understood by considering two classical correlated electrons in $Z=+2$ Coulomb potential. The Hamiltonian of such a system can be described by

$$H = \frac{p_1^2}{2} - \frac{2}{r_1} + \frac{p_2^2}{2} - \frac{2}{r_2} + \frac{1}{r_{12}}, \quad (5.1)$$

where \vec{r}_1 and \vec{r}_2 are the positions of the first and second electrons from the nucleus; $r_{12} = |\vec{r}_1 - \vec{r}_2|$ is their mutual separation; and \vec{p}_1 and \vec{p}_2 represent the momenta of two electrons. For $5dnd$ wave packet, the extent of the outer electron's orbit is much greater than that of the inner electron. Therefore, the condition $r_1 > r_2$ is satisfied except during very brief periods when the wave packet approaches the nucleus [4, 5, 10, 63]. Thus, the interaction term $\frac{1}{r_{12}}$ may be expanded in a series

$$\begin{aligned} \frac{1}{r_{12}} &= \frac{1}{|\vec{r}_1 - \vec{r}_2|} \\ &= \sum_{k=0}^{\infty} \frac{r_2^k}{r_1^{k+1}} P_k(\cos \gamma) \\ &= \frac{1}{r_1} + \frac{r_2}{r_1^2} P_1(\cos \gamma) + \dots \end{aligned} \quad (5.2)$$

where γ is the angle between the position vectors of the two electrons. Considering only the first term in 5.2, the Hamiltonian is then

$$H = \frac{p_1^2}{2} - \frac{1}{r_1} + \frac{p_2^2}{2} - \frac{2}{r_2}, \quad (5.3)$$

which describes a two independent electron mode in which the “outer” nd Rydberg electron sees a $1/r$ Coulomb potential and the “inner” 5d electron experiences a $2/r$ potential. However, in classical terms, the second and higher terms of Eqn. 5.2

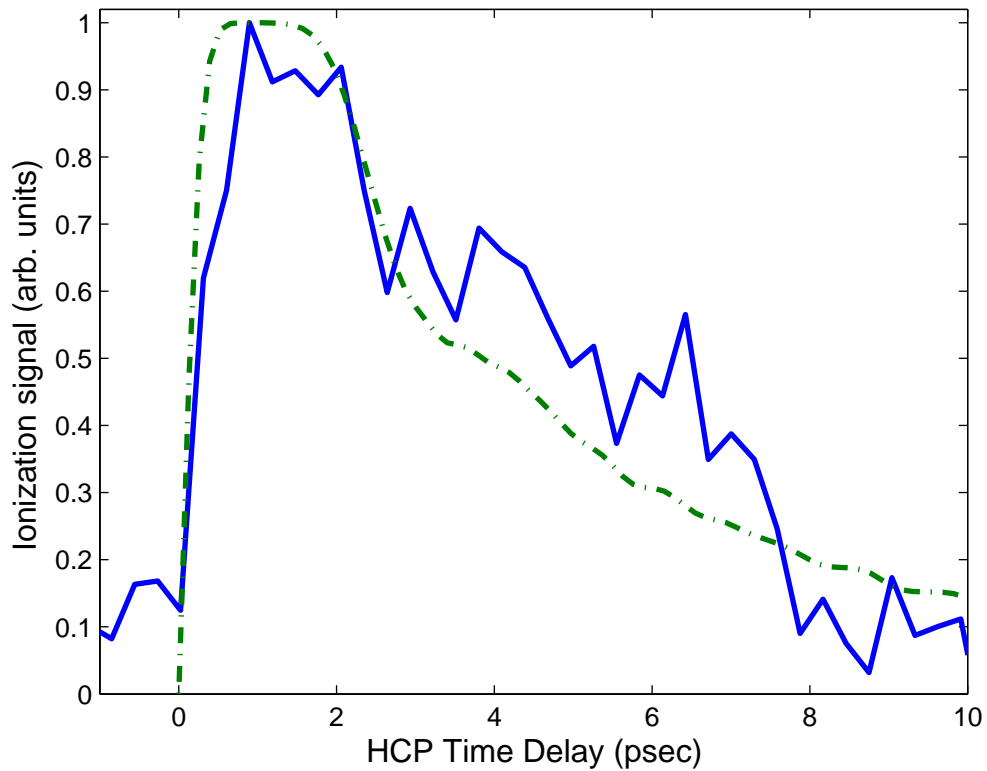


Figure 5.3: The survival probability of $5d25d$ autoionizing wave packet. The solid line is the normalized double ionization signal by HCP as a function of time delay between L2 and HCP. The dashed line is the result of a two-channel quantum defect theory calculation described in text. The calculation assumes that the wave packet consists of 6 coherently superimposed states in a Gaussian energy distribution with FWHM 50cm^{-1} centered about an average effective quantum number $n=25$.

become non-negligible when the radii of two electrons are comparable. Quantum mechanically, the interaction strength is a maximum at locations where the wave functions of the electrons have a larger spatial overlap. Because the $5d_{5/2}^+$ electron is bound tightly to the Ba^{++} core, $r_1 \approx r_2$ only when both electrons are near the core. Thus, the interaction of the two electrons due to these higher terms results in periodic energy exchange between the two electrons. The autoionization rate is the maximum at brief instances when the wave packet moves near the ion core and is negligibly small when the wave packet is at a large radius. Therefore, the population of $5_{5/2}dnd$ wave packets with respect to time shows step-like features as the Rydberg electron moves in and out from the ion core at its classical Kepler period.

The Rydberg electron in the $5dnd$ wave packet moves outward quickly after the excitation, such that the wave functions of the two electrons have less spatial overlap. The chance to exchange energy between the two electrons is small, resulting in a negligible autoionization rate and a nearly constant double ionization signal. When the Rydberg electron returns to the core, the electrons redistribute their energies due to the strong mutual repulsive force, releasing one electron into the continuum, and decreasing the population of the bound wave packet. The survival probability of $5d_{5/2}nd$ autoionizing wave packet has a step-like structure with step spacing equal to the Kepler period of the Rydberg electrons [10, 62, 63].

Two channel quantum defect theory calculation

An approximate, but more quantitative description of autoionization of the $5d_{5/2}nd$ wave packets can be obtained using two-channel quantum defect theory [60–62].

The spectral density of the $5d_{5/2}$ channel can be written as [60,61]

$$A(E) \propto \frac{1}{\sin \pi(n + \delta + i\gamma/2)}, \quad (5.4)$$

where n is the effective quantum number of $5d_{5/2}nd$ autoionizing state, δ is the quantum defect, γ is the scaled autoionization rate. After a laser pulse with spectral amplitude $F(E)$, the excitation amplitude of $5d_{5/2}nd$ autoionizing wave packet is

$$S(E) = A(E) \cdot F(E). \quad (5.5)$$

The time-dependent autoionization rate of the $5d_{5/2}nd$ wave packet is the square modulus of the Fourier transform of this excitation amplitude

$$r(t) = \left| \int S(E) e^{-iEt/\hbar} dE \right|^2. \quad (5.6)$$

The rate at which each atom is excited to $5d_{5/2}nd$ states is

$$r'(t) = \left| \int F(E) e^{-iEt/\hbar} dE \right|^2 \quad (5.7)$$

where we assume that $F(E)$ has been normalized such that

$$\int_0^\infty \left| \int F(E) e^{-iEt/\hbar} dE \right|^2 dt = 1 \quad (5.8)$$

In this case, the probability that an atom remains in the $5d_{5/2}nd$ autoionizing wave packet as a function of time is given by the time integral of the net rate into and out of the excited states

$$P(t) = \int_0^t R(t') dt', \quad (5.9)$$

where $R(t) = r'(t) - r(t)$.

To characterize the wave packet, the measured decay signal is compared with the calculated for a two-channel quantum defect theory which has been proven accurate of the wave packets of interest [62, 63]. In particular, previous work [27] indicates that $J=0$ states, which quantum defect, $\delta = 2.4$, and the scaled autoionization rate, $\gamma = 0.052$ are predominantly excited. We vary the center of the average and range of n -states in the wave packet to achieve the best agreement [62, 63]. A typical fit of the theory to the experiment is shown in Fig. 5.3. While the fit is fairly sensitive to the value of the average principle quantum number, it is insensitive to the range of n -states included in the wave packet [27]. Thus, we use the measured bandwidth of the excitation laser L2, $\Delta\nu \simeq 50\text{cm}^{-1}$, to determine the distribution of n -states about the average value.

5.3.2 Doubly excited Rydberg wave packets

As described in the previous section and the previous chapter, we are able to characterize both the neutral and ionic wave packets by examining the double ionization probability. If the HCP is directed into the laser-atom interaction region after both wave packets are excited, the delay dependent double ionization signal should reveal information regarding time-dependent two-electron interactions.

Fig. 5.4 shows two measurements with different delays, t_1 , between the excitation of the two wave packets. All other conditions are identical. In this figure, the time axis corresponds to the HCP delay following the excitation of the first wave packet. In the upper plot, the ionic wave packet is launched about 7.2 psec after the neutral wave

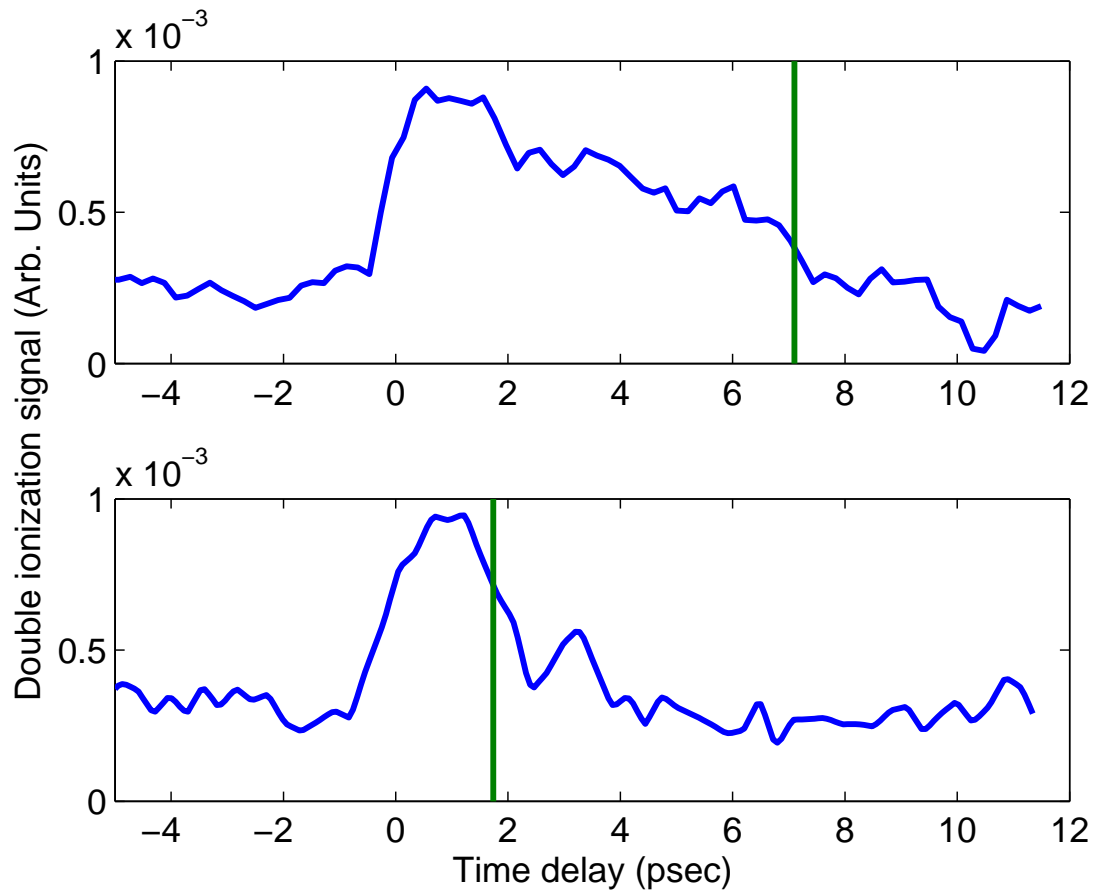


Figure 5.4: Double ionization signal as a function of HCP time delay with respect to the excitation of the first electronic wave packet. The first wave packet is excited at $t=0$, and the vertical lines indicate the time of the excitation of the second wave packet.

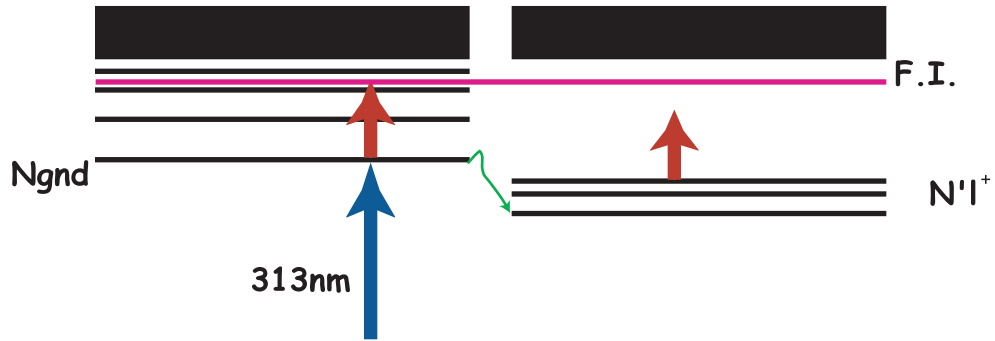


Figure 5.5: Schematic diagram of HCP energy transfer with respect to the double and field ionization limits.

packet, whereas the first wave packet is excited about 1.7 psec preceding the excitation of the second wave packet in the lower plot. As discussed in the previous section, the double ionization yield in upper plot corresponds to the survival probability of $5d_{5/2}nd$ neutral wave packet before the ionic wave packet is excited. In other words, the double ionization yield is proportional to the number of atoms remaining in the $5d_{5/2}nd$ states prior to the creation of the second wave packet.

In contrast, the lower plot shows that the excitation of the second wave packet significantly reduces the detected double ionization yields. This suggests that the excitation of the second wave packet quickly redistributes the energies between two electrons. This energy exchange results in the population of ionic Rydberg states of sufficiently low energy that cannot be ionized by the HCP and the clearing pulse combination (see the schematic HCP strength diagram 5.5). Apparently, HCP double ionization can be used to probe the time-dependent transfer of population either i) directly to ionic states which can not be ionized; or ii) into doubly excited configurations which then decay into ionic states that cannot be ionized.

Due to the autoionization of the $5d_{5/2}nd$ neutral wave packet, the number of atoms excited into the double Rydberg wave packets decreases as the excitation time of the

ionic wave packet is increased. In order to focus on the double Rydberg wave packet dynamics, we eliminate the t_1 -dependent variation in initial double Rydberg wave packet population by normalizing the double ionization signal to the $5d_{5/2}nd$ survival probability. As described in the previous section, this delay-dependent normalization is obtained by exciting the second wave packet long after (~ 7.2 psec) the excitation of the $5d_{5/2}nd$ wave packet. Any variation from unity in the normalized double ionization yield reflects the time-dependent energy exchange between the two wave packets. This construction implicitly assumes perfect isolated core excitation neglecting variations in the ionic wave packet excitation probability as a function of the wave packet excitation delay [64]. This approximation may break down if the ionic wave packet is excited during the brief periods when the neutral wave packet is near the core.

We emphasize that by varying the time delay between L2 and L3+L4, the initial relative positions and direction of radial motion of the two electrons can be adjusted. Alternatively, the energies and periods of the two wave packets can be tuned by changing the wavelengths of L2 and L4. The normalized experimental data for double Rydberg wave packets with $38g25d$ and $38g23d$ initial configurations are plotted in Fig. 5.6 and 5.7, respectively. In both cases, the normalized double ionization signal shows a clear decrease upon the excitation of the second wave packet. This decrease is the result of the interaction between the two electrons which is presumably maximized at times when the wave packets are spatially overlapped.

Following the initial drop in signal, the normalized data levels out at long times, with small modulations about a roughly constant background. This background levels shows a variation which is consistent with a predicted periodic modulation as a function of the time delay, t_1 , between the two wave packets. This modulation

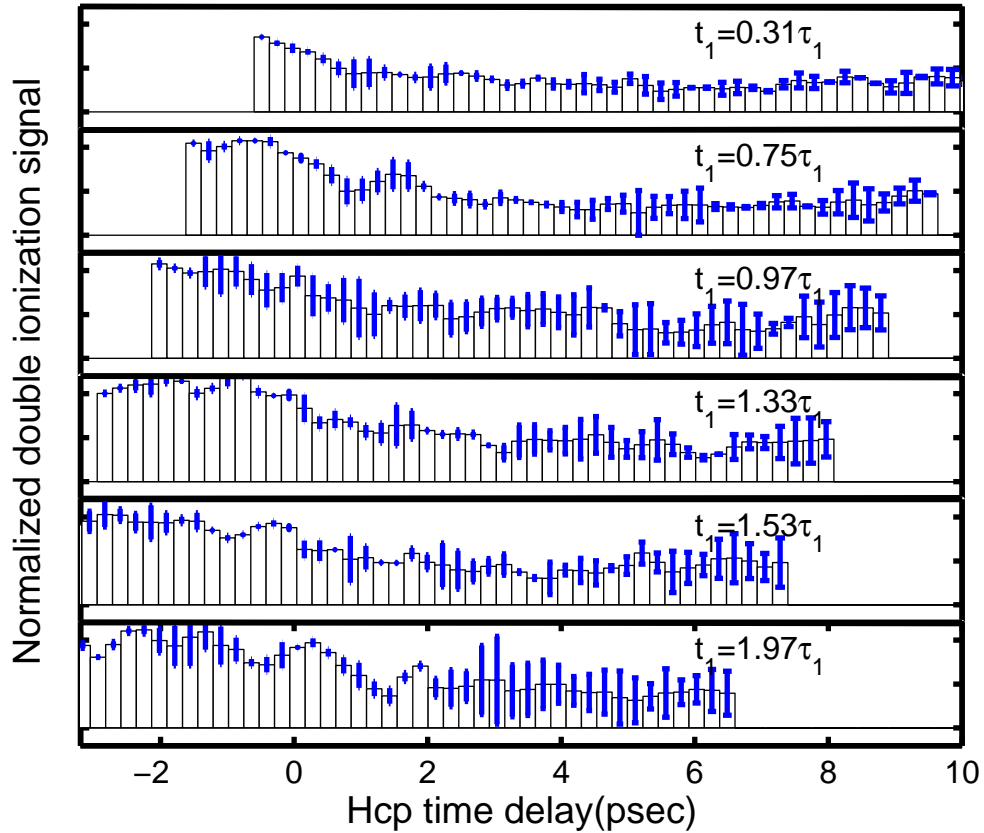


Figure 5.6: The normalized double ionization signal of N_{gnd} double Rydberg wave packets, where $n \sim 25$ and $N \sim 38$, as a function of delay, t_2 , with respect to the ionic wave packet excitation. Each data set corresponds to a different time delay, t_1 , between the excitation of the two wave packets in terms of the Kepler period of the first wave packet. The data are collected in a continuous delay scan and integrated over (230 fsec) time bins. These time bins are significantly smaller than the >1 psec combined temporal resolution of the lasers and HCP. The error bars represents the standard deviation of two separate data sets.

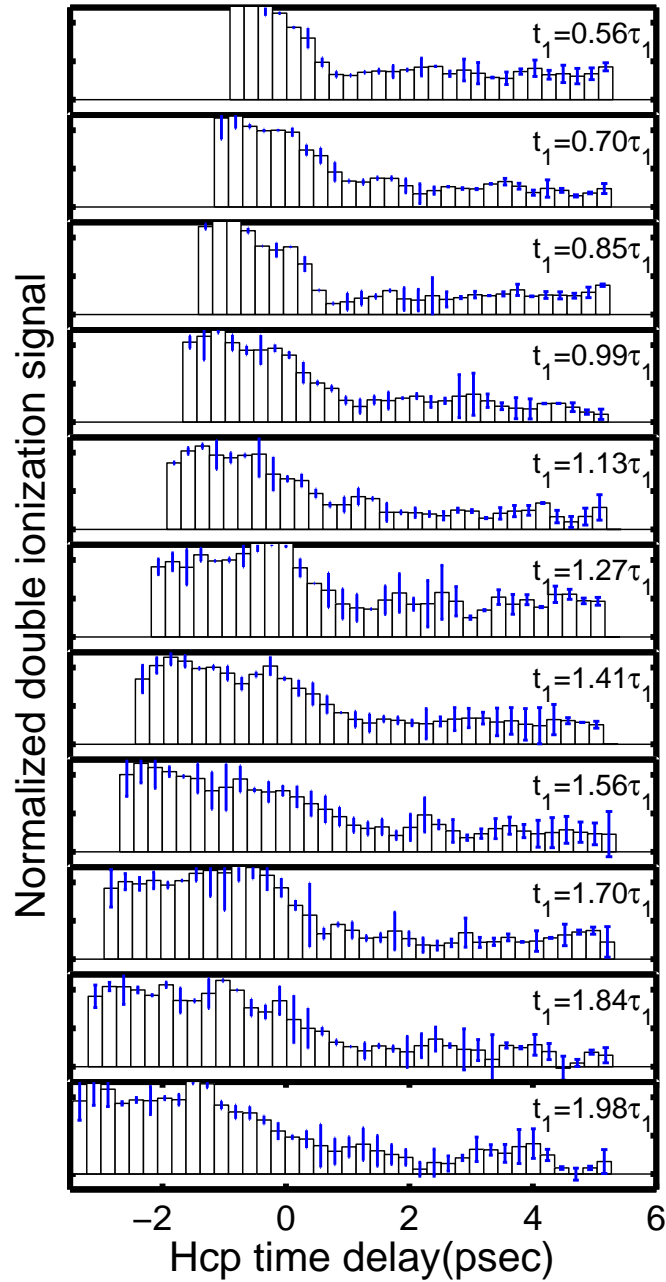


Figure 5.7: The normalized double ionization signal of $Ngnd$ double Rydberg wave packets, where $n \sim 23$ and $N \sim 38$, as a function of delay, t_2 , with respect to the ionic wave packet excitation. Other conditions are the same as described in Fig.5.6.

is more apparent in Fig. 5.7. For example, the background signal at large delays is significantly greater for $t_1 = 1.27\tau_1$ than for $t_1 = 0.99\tau_1$. Recall that the magnitude of the double ionization signal is a measure of the number of electrons which are bound to the Ba^{++} ion with an energy less than the field ionization limit in the clearing pulse. Given the long ($>10\text{nsec}$) delay of the clearing pulse, it is highly unlikely that any doubly-excited atoms survive to this detection time. Thus, the background signal records the fraction of the initial double Rydberg population that is unbound or weakly bound following the HCP and *all two electron interactions*.

To better investigate the background variation vs. t_1 , for each value of t_1 the double ionization signal is averaged over HCP delays $t_2 > 4$ psec. The average background level is well established by this delay and the signal levels at longer t_2 delays ($>20\text{psec}$) are essentially identical. This indicates that the primary electron-electron interactions have concluded within ~ 4 psec following the ionic wave packet excitation. The averaged background signal for two distinct data runs is plotted as a function of t_1 in Fig. 5.8. The signal is smaller for excitation delays near integer multiples of the Kepler period of the neutral wave packet. Apparently, more tightly bound ionic states are produced when the neutral wave packet is near the inner turning point of its orbit at the instant the second wave packet is excited. This observation is consistent with the intuitive idea that the energy exchange between the two electrons is the largest when the two electrons are near the ion core with large momenta, such that hard, violent collision may occur. Conversely, the double ionization signal is largest when the neutral wave packets is far from, and traveling away from the ion core when the second wave packet is excited. In this case, the first energy exchange between electrons occurs through gentle long range interactions. A quantitative investigation of the final ionic state distributions resulting from the autoionization of double Rydberg wave packets

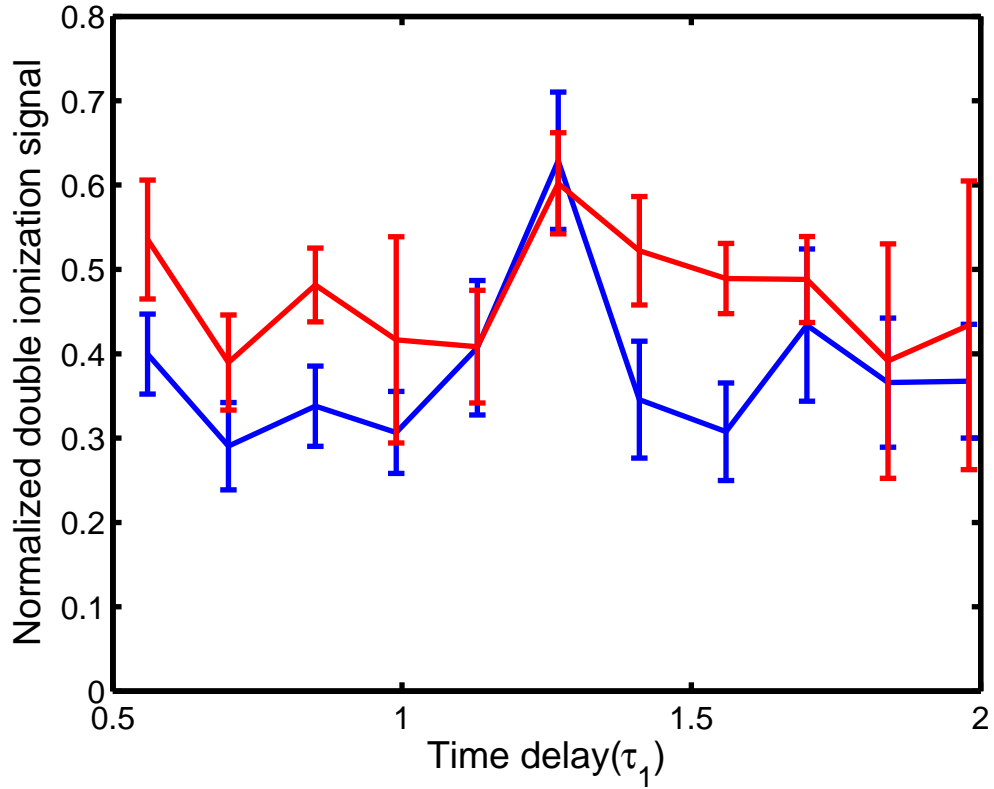


Figure 5.8: The normalized double ionization background signal of $38g23d$ double Rydberg wave packets as a function of delay t_1 between the launch of two wave packets in terms of the Kepler period, τ_1 , of the neutral wave packet. The error bar represents the standard deviation of data.

was previously performed by Pisharody [27, 49]. Our measurements are in qualitative agreement with predictions of that analysis. The data for the $38g25d$ configuration does not exhibit any clear background modulations. This can be attributed to two issues. First, autoionization of the $38g25d$ states results in the population of more weakly bound states than in the $38g23d$ case. In the former, it is likely that all, or most, of the final ionic states are ionized by the clearing pulse, except during a very short time interval when both electrons are near the nucleus. The coarse sampling of the wave packets delay time, t_1 , is insufficient to resolve a clear minima in the signal.

Second, the signal to noise ratio in the *38g25d* data set is poorer, making it more difficult to define the background signal for a given value of t_1 .

As noted above, the time-independent background signal provides a somewhat cruder version of the information that was offered from the first, and only other, double Rydberg wave packet experiments which were performed several years ago [49, 50]. However, the results presented here are unique in that they also provide the time-resolved information on the electron-electron interactions. Indeed, the data presented in Fig. 5.6 and 5.7 give the first direct view of time-dependent energy exchange between electrons in double Rydberg wave packets. This is the primary result of this dissertation.

The normalized double ionization yield data exhibit several robust HCP delay-dependent features that reflect different aspects of the double Rydberg dynamics. First, the excitation of the ionic wave packet is accompanied by a nearly immediate drop in the normalized electron signal. This initial signal decrease is observed for all the data sets, independent of distance of the neutral wave packet from the ion core at the time of ionization. Intuitively, we might expect a substantial change in the double ionization signal only after significant interaction between the two electrons. According to previous works [49] significant energy is exchanged between the wave packets only at times when their radii are comparable. For some wave packet delays, t_1 , the ionic wave packet must travel out to the maximum radius of the neutral wave packets, $R \approx 66\text{nm}$, before this interaction occurs. Thus, it is not unreasonable to assume that, for a range values of t_1 , that the decrease in the double ionization signal would not occur for some time after the ionic wave packet excitation. However, this time is not as long as one might initially expect. The ionic wave packet requires only ~ 0.8 psec to reach the outer turning point of the neutral wave packet. Given the

~ 1 psec time resolution of the experiment, this 0.8 psec transit delay may not be readily observable.

The second observation is that the slope of the initial signal decrease shows some variation as a function of t_1 . This indicates, not surprisingly, that i) the rate of energy exchange between the two electrons depends on their locations and relative radial velocity during their first interaction, and/or ii) that the interaction between electrons is not limited to a single, isolated event. Slow collisions and multiple collisions apparently do occur.

Third, after the initial drop in signal, the double ionization yield ceases to decrease monotonically, but instead, oscillates about a nearly constant background as described previously. The phase and amplitude of these oscillations depend on the time delay of the excitation of two wave packets. The classical simulations described below indicate that these modulations reflect the evolution of the momentum distribution of the ionic wave packet that is formed during autoionization. As described previously, the energy transfer from the HCP to the ionic wave packet depends critically on its momentum distribution at the time of kick.

5.3.3 Classical simulation

We utilize numerical simulations to guide our interpretation of the data beyond the qualitative features noted above. Multichannel quantum defect theory (MQDT) has been successfully applied to simulated time and frequency domain experiments in two-electron systems [7,63]. However, MQDT is valid only for atomic states where the Rydberg electron sees a Coulomb potential at large radial position. The three body Coulomb system explored in this experiment has two electrons in high-lying Rydberg states just below the double ionization limit of Ba. Neither electron is confined to a

small volume surrounding the Ba^{++} ion. The electron wave functions can overlap at very large distances from the nucleus, and no distinct Coulombic regions can be defined for either electron. Thus, MQDT is not applicable. In addition, direct time-dependent quantum simulations are very difficult because of the extremely high density of bound and continuum states in this energy regime [66]. Instead, due to the fact that we excite both electrons into high lying Rydberg wave packets, following Pisharody [27,49], we utilize a classical simulation in an attempt to better understand the experimental results.

As discussed in the previous chapters, the evolution of a singly excited radial wave packet can be described as a shell of probability density, radially breathing in and out in a Coulomb potential. This wave packet can be modeled as an ensemble of classical electrons with the nearly same energy and angular momentum moving together in a pure Coulomb potential. We use this classical concept to treat two spinless electrons interacting through their mutual Coulomb repulsion in a doubly charged Coulomb potential. The two electrons are launched from the nucleus with relative delays, energies and angular momenta defined in the experiments. Newton's equations of motion are used to track the evolution of the two electrons for some period of time. In order to simulate the HCP detection in the experiments, the electrons are exposed to a Gaussian field pulse with a ~ 0.6 psec full width at half maximum (FWHM) duration. Rectangular Cartesian coordinates are used and the polarizations of the lasers are fixed along the z-axis. As in experiment, calculations are performed for different wave packet and HCP delays.

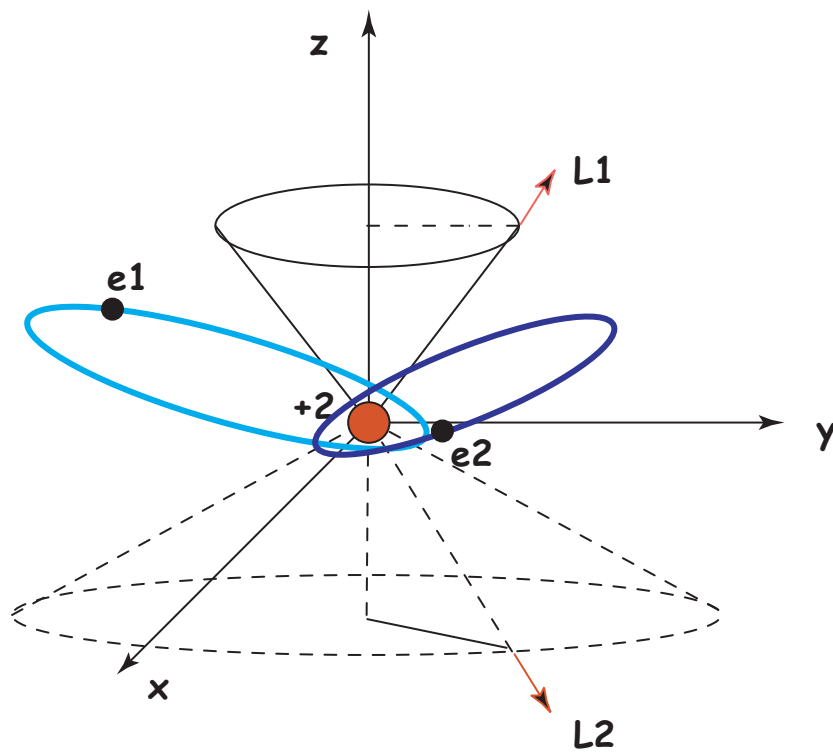


Figure 5.9: Schematic diagram of initial condition of two electrons. Two cones indicate the possible angular momentum vectors L_1 and L_2 with total $M_z = 0$.

Initial conditions

We select the initial conditions for the ensemble of electrons using the parameters from the experiments. The principal quantum number of the first electron, with energy E_1 , is

$$n = \sqrt{\frac{-1}{2E_1}}. \quad (5.10)$$

When the wave packet is excited, the electron is localized near the inner turning point of its elliptical orbit in a pure, singly-charged Coulomb potential. The first electron moves in the Coulomb potential for a time t_1 before the launch of the second electron. Kepler's equation [75],

$$\omega t_1 = \Psi - e \sin \Psi \quad (5.11)$$

is used to solve for the eccentric anomaly, Ψ , where $\omega = 1/n^3$ is the frequency of revolution and e the eccentricity of the orbit. Then, the orbital angle $\theta(t_1)$ at time t_1 can be calculated using [75]

$$\tan \frac{\theta}{2} = \tan \frac{\Psi}{2} \sqrt{\frac{1+e}{1-e}} \quad (5.12)$$

Prior to the launch of the second electron, the “initial” radius of the first electron is

$$r(\theta) = \frac{l_1^2}{1 + \sqrt{1 + 2E_1 l_1^2} \cos(\theta)} \quad (5.13)$$

, where l_1 is the angular momentum of the first electron. The “initial” velocity of the first electron can be found by

$$v_{x0}^{(1)} = \dot{r}(\theta) \cos \theta - \frac{l_1}{r(\theta)} \sin \theta \quad (5.14)$$

$$v_{y0}^{(1)} = \dot{r}(\theta) \sin \theta - \frac{l_1}{r(\theta)} \cos \theta, \quad (5.15)$$

where

$$\dot{r}(\theta) = \sqrt{\frac{2}{r(\theta)} - \frac{1}{n^2} - \frac{l_1^2}{r^2(\theta)}} \quad (5.16)$$

and $v_{x0}^{(1)}, v_{y0}^{(1)}$ are two orthogonal components of velocity in the plane of the Kepler orbit. Because of the finite duration of the excitation laser, the precise time at which this first electron is excited is not well defined in the experiment. To take this uncertainty into account, t_1 is selected accordingly to a Gaussian distribution with a FWHM of 0.7 psec equal to the temporal width of the wave packet excitation lasers added in quadrature. The durations of these pulses are extracted from experimental measurements.

Similarly, the second electron is initialized according to its energy E_2 . Assuming the first electron is far from the nucleus at the instant of its excitation, the principal quantum number of this electron is

$$N = \sqrt{\frac{-2}{E_2}}, \quad (5.17)$$

in a pure $-2/r$ potential.

The direction of the angular momentum vector for the first electron is determined by its projection onto the z axis,

$$m_1 = \vec{l}_1 \cdot \hat{z}, \quad (5.18)$$

which ranges from $-l_1$ to l_1 . The direction of the angular momentum vector is chosen at random and the position and velocity of the first electron are determined

by rotating the electron orbit coordinates into the lab frame using Euler angles [75]. Since all the excitation lasers in the experiment have the same polarization, the projection of the total electronic angular momentum along the common laser axis is zero. Therefore, the direction of the angular momentum of the second electron is constrained according to

$$m_2 = \vec{l}_2 \cdot \hat{z} = -m_1. \quad (5.19)$$

Using Eqn. 5.19, the position and velocity of the second electron are transformed into the lab frame from the electron orbit plane.

The energies of the two electrons are chosen at random from Gaussian energy distributions which match those used in the experiment. The state composition of the “ionic” wave packet is determined using the method described in the previous chapter. The two-channel quantum defect theory fit to the data and the measured bandwidth of L2 are used to determine the energy distribution of the neutral wave packet, as discussed in the previous section. Calculations are performed over a range of HCP delays, duration, and strengths. However, for direct comparison with the experimental data, the numerical results and discussion below focus on calculations performed using the laboratory HCP duration 0.6 psec FWHM, (as determined by independent measurement [34]), and impulse 0.0038 a.u., (as determined by HCP ionization of Rydberg eigenstates excited in the same apparatus [69]). Typically, 2000 two-electron trajectories are used to determine the double ionization yield at each HCP delay.

The motion of both electrons in the $2/r$ Coulomb potential in the presence of the mutual repulsive force between two electron is calculated using a fourth order Runge-Kutta routine [70]. For each electron pair, the calculation is run until at least

one electron gains sufficient energy to escape the atom. Because of the long range interaction between electrons, ionization of an electron is not well-defined at finite distances from the nucleus. The functional criteria for stopping the computation are i) at least one electron is at a radius > 20000 a.u. and ii) the separation between the electrons is greater than 95% of the largest radius of two electrons. This ensures that at least one electron will ionize and that the electron interaction energy is $< 5\%$ of the total energy of either electron. The electron which is the smallest distance from the ion is labeled the “ionic” electron. The energy of the “ionic” electron is compared to the ionization limit determined by the clearing pulse. If the energy is greater than this limit, then a double ion is counted, otherwise, only single ionization has occurred. Note that this limit depends on the angular quantum number m of the ionic electron. The classical simulations indicate a spread in the angular momentum of the final ionic Rydberg state with $N > l \geq |m| \geq 0$ as shown in Fig. 5.10.

In order to determine the correct ionization limit for each ionic electron, the role of the quantum number m in the Stark effect in non-hydrogenic ions must be taken into account. Field ionization of an electron in a hydrogen-like ion occurs if the electron energy exceeds the height of the local minimum, E_c , in the potential energy, V , associated with the “downhill” parabolic coordinate, $\eta = r - z$,

$$V(\eta) = -\frac{F}{2}\eta - \frac{2Z_2}{\eta} + \frac{|m|^2 - 1}{2\eta^2}. \quad (5.20)$$

[73] Here F is the magnitude the static field and Z_2 is the effective charge in the downhill coordinate [73]. η_c is the position of the local minimum defined by $dV/d\eta|_{\eta_c} = 0$. Note that Z_2 depends on the orientation of electron’s orbit, which is defined by the Runge-Lenz vector [74]

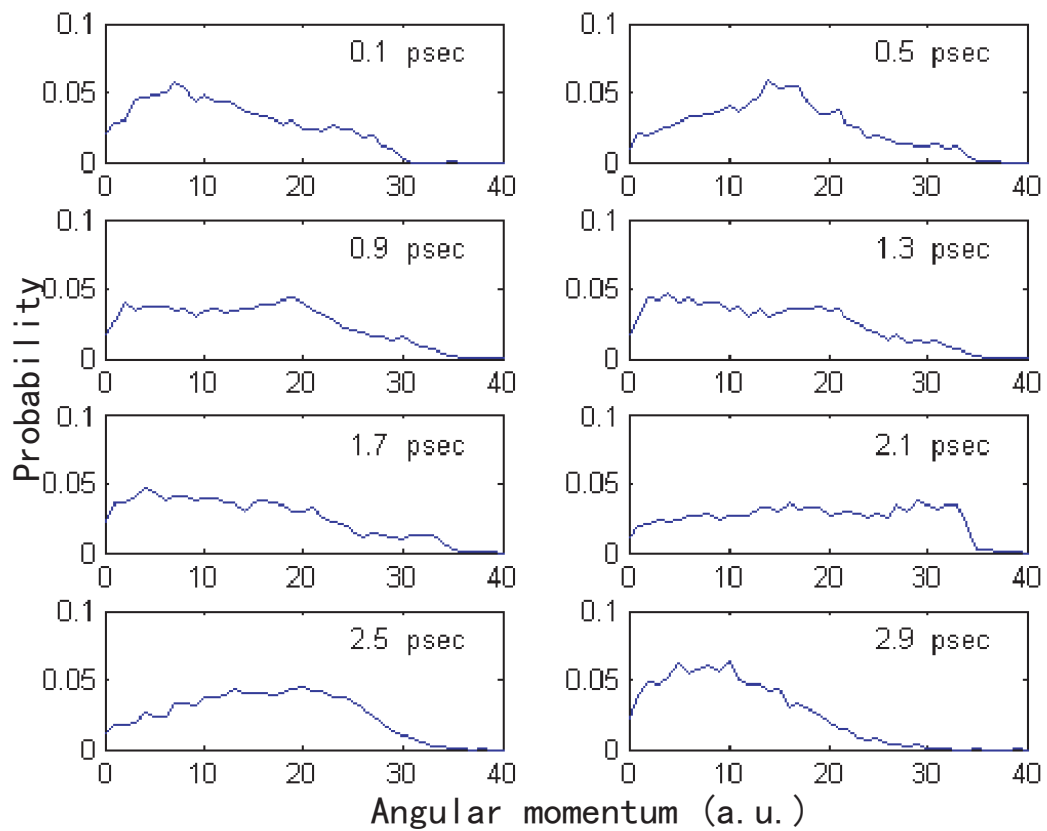


Figure 5.10: The angular momentum distribution of final ionic states after autoionization for $38g25d$ wave packets with the time delay between two electronic wave packets from 0.1 psec to 2.9 psec in absence of HCP.

$$\vec{M} = \vec{p} \times \vec{l} - Z\hat{r} + \frac{1}{2}(\vec{r} \times \vec{F}) \times \vec{r}. \quad (5.21)$$

The \hat{z} projection of \vec{M} , M_z , is related to the separation constants Z_1 , Z_2 in parabolic coordinates. M_z is a constant of the motion and its value ranges from $-Z \leq M_z \leq Z$ in a static field. Thus, the separation constant Z_2 can be written as [74]

$$Z_2 = \frac{1}{2}(Z - \langle M_z \rangle). \quad (5.22)$$

M_z and m for the ionic electron can be readily extracted from the calculation to determine the critical energy E_c for field ionization of each electron.

Of course, for non-hydrogenic ions, like Ba^+ , orbital precession occurs in the non-Coulombic potential. If the precession frequency is large enough, the critical field ionization energy, E_c , is independent of orbit orientation, M_z , and is equal to the minimum critical energy (that for the most downhill state) in hydrogen. However, for large values of m , the electron does not sample the non-Coulombic portion of the potential, orbital precession is negligible, and the static field dynamics proceed as in hydrogen. Therefore, we define a critical value of $|m| = m_c$ [26, 71]. We assume that electrons with $|m| \geq m_c$ ionize as in Hydrogen, whereas electrons with $|m| < m_c$ ionize at the standard threshold for diabatic field ionization of alkali atoms, $E_c = 3/2\sqrt{FZ}$ [15]. Typically, we set $m_c = 8$, but our results are quite insensitive to the specific value of $6 \leq m_c \leq 10$.

Simulation results

In order to compare with the experiments, we use the “wave packet” terminology to describe a classical distribution in this section. Of course, the simulation uses the

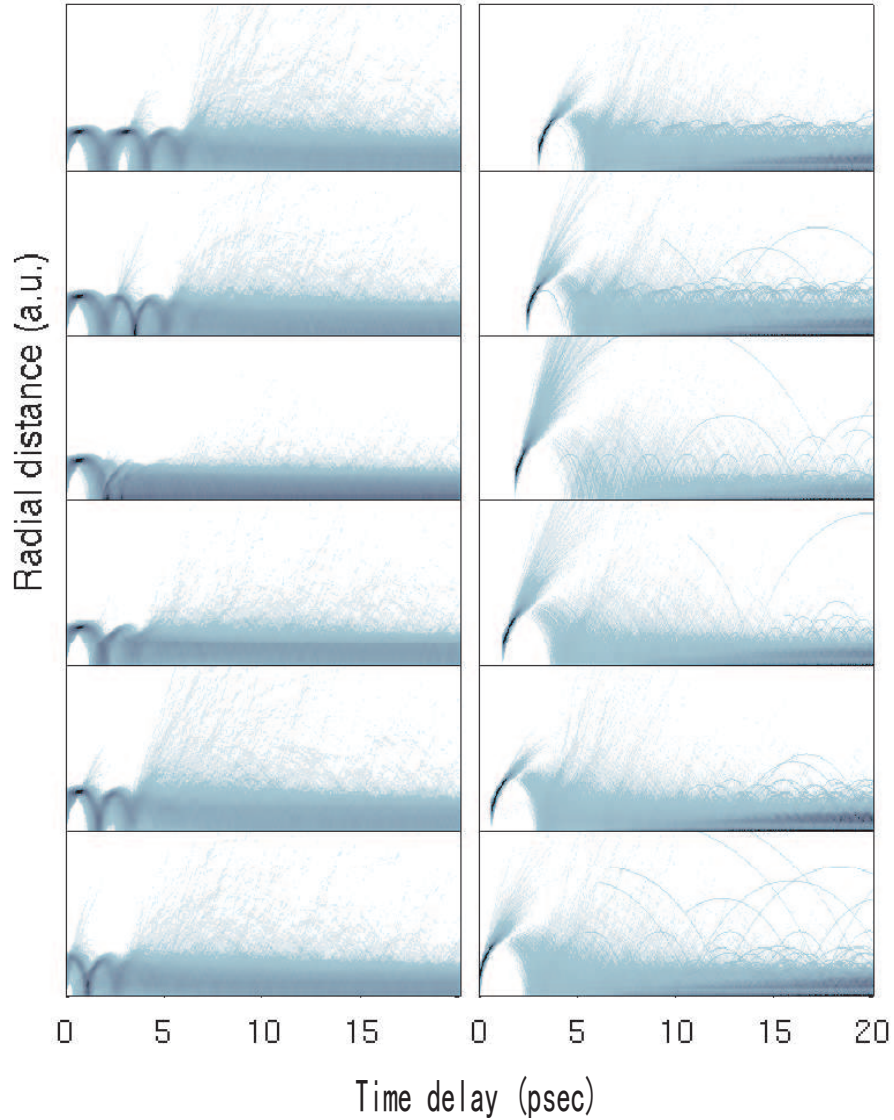


Figure 5.11: Simulated trajectories of two electrons with a neutral wave packet, $n = 25$, and the ionic wave packet, $N = 38$. The right column is the radial distance of the “ionic” electron as a function of time with respect to the excitation of the neutral wave packets. Analogous plots for the first electron are shown on the left. From top to bottom, the time delay between the excitation of the two electronic wave packets decreases from $1.3 \tau_1$ to 0 psec with a step size of $0.25 \tau_1$. The maximum radial distance is 5000 a.u for each plot. Darker regions indicate overlapping trajectories and, therefore, higher probability.

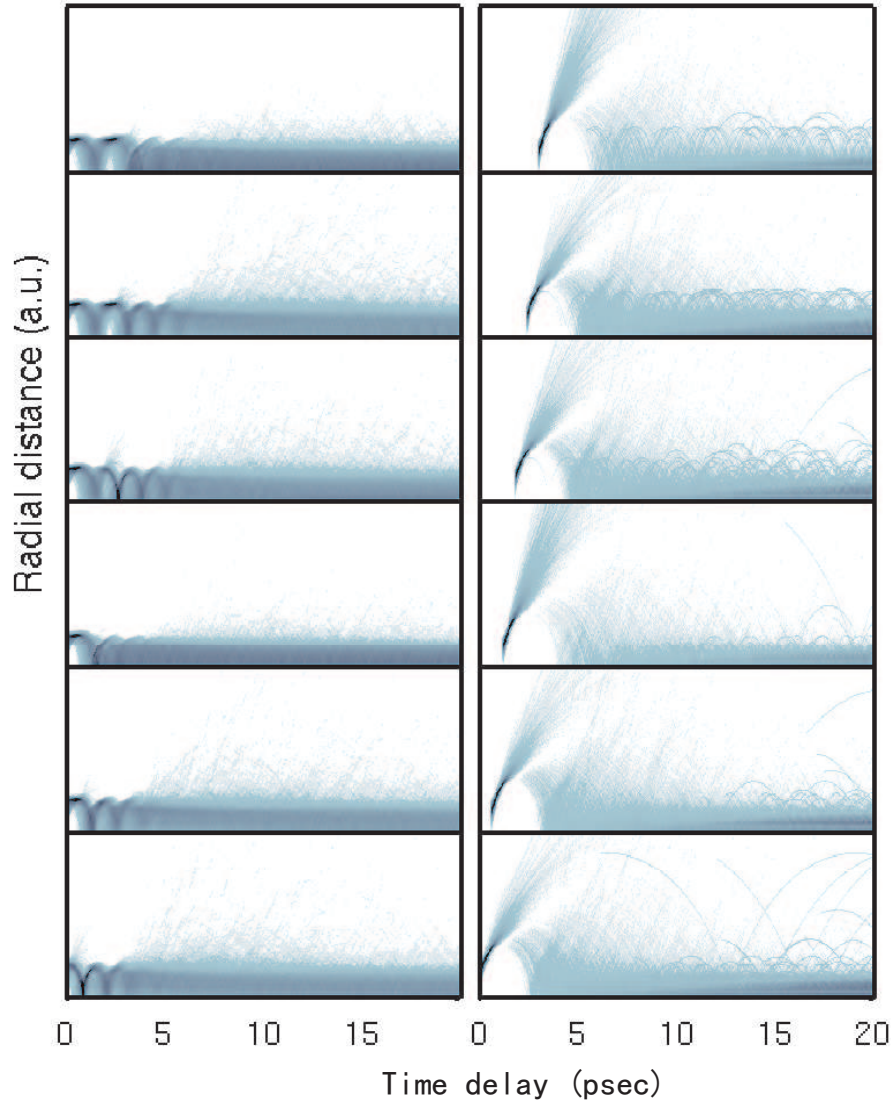


Figure 5.12: Simulated trajectories of two electrons simulation with a neutral wave packet, $n = 23$, and the ionic wave packet, $N = 38$. The right column is the radial distance of the “ionic” electron as a function of time with respect the excitation of the neutral wave packets. Analogous plots for the first electron are shown on the left. From top to bottom, the time delay between the excitation of the two electronic wave packets decreases from $1.7\tau_1$ to 0 with a step size of $0.3\tau_1$. The maximum radial distance is 5000 a.u. for each plot. Darker regions indicate the overlapping trajectories and, therefore, higher probability.

ensemble of classical electron trajectories, which is not the the coherent wave packets.

First, we examine the two wave packets' evolution without the HCP. Fig. 5.11 and Fig. 5.12 show the simulated, time-dependent radial probability distributions for selected values of t_1 for $38g25d$ and $38g23d$ double Rydberg wave packets, respectively. The simulations assume excitation pulses with durations of 400 fesc and 670 fsec, and the wave packets are composed of 6 and 3 n-states for the neutral nd and Ng^+ wave packets, respectively. Prior to the launch of the second wave packet, the first wave packet oscillates radially in a singly charged potential. Immediately following the excitation of the second electron, the radial position, r_2 , of the second wave packet is much less than that of the first wave packet, r_1 . Thus, to lowest order in the electron-electron interaction, the first wave packet and the second wave packet see ion core charges of $Z_1 = 1$ and $Z_2 = 2$, respectively, and move independently in their respective potentials. However, at some time within half a Kepler period of the second wave packet, the mean radii of the two wave packets will coincide, $r_1 = r_2 = R$ within our lowest order approximation, the two electrons exchange roles for $r_2 > r_1$, with the first wave packet providing the screening for the second wave packet. The sudden change in screening results in an energy increase, $\Delta E_2 = 1/R$ for the second wave packet and equal energy increase, $\Delta E_1 = -1/R$ for the first wave packet [27]. If ΔE_2 exceeds the initial binding energy, $-2/N^2$, of the second wave packet, then this electron is no longer bound and leaves the atom. If this sudden energy exchange occurs at too large a radius, ΔE_2 is insufficient to ionize the second wave packet. This electron then moves as a highly excited neutral wave packet and returns to the ion core at some time later to interact with the first wave packet again. Eventually, a collision occurs at sufficiently small radius, R , for ionization of one of the two electrons [49]. This qualitative picture is bore out quantitatively in the simulations.

If the ionic wave packet is excited while the neutral wave packet is near the core, the second electron acquires enough energy to leave the atom immediately, and the recognizable coherent oscillations of the first wave packet is destroyed as the strong mutual repulsive force between two electrons redistributes population over a wide range of final ionic states. However, the coherent evolution of the first electron is well-preserved for some time after the first collision if it occurs near the outer turning point of the neutral wave packet. In this case, the second electron is promoted to higher energy states which have Kepler time scales exceeding the ~ 2.1 psec of the initial $38g^+$ wave packet. This is in accord with the sudden ionization model [49]. Ionization only occurs when the collision radius is smaller than a critical radius $R_c = N^2/2$.

Fig. 5.13 shows the final ionic state distributions following the autoionization of the wave packets shown in Figs. 5.11 and 5.12. When the time delay between the two wave packets is close to an integer multiple of the Kepler period of the first electron, the location where two electrons meet is close to the ion core. Therefore, the second electron gains more energy and the first electron loses more energy than when the electrons meet far from the nucleus. Consequently, lower ionic states are produced. This is in contrast to the distribution observed when the electron shells cross near the outer turning point of the orbit of the first wave packet [27].

As described previously, the basic premise of our experimental technique is that the HCP double ionization signal reveals the time-dependent energy exchange between the two electrons. More precisely, the HCP delay dependence of the double-ionization yield is a direct measure of the rate at which ionic Rydberg states, which are too tightly bound to be ionized by the HCP and clearing pulse combination, are produced via electron-electron interactions. However, the utilization of this approach for extracting quantitative information on the energy exchange rate involves an im-

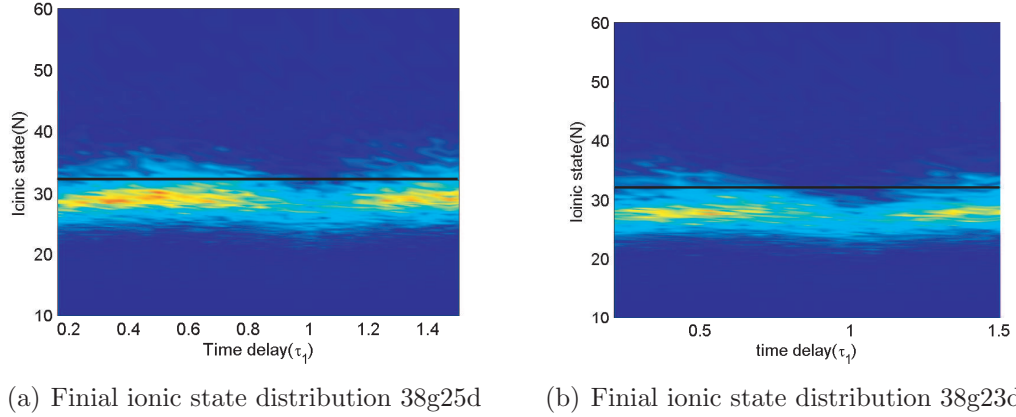


Figure 5.13: Simulated final ionic state distribution following autoionization of the 38g25d and 38g23d wave packet configurations without HCP. The warmer color denotes higher probability. The dark line indicates the ionization threshold determined by the 2400V/cm clearing pulse (assuming diabatic field ionization [15]). The x-axis is the time delay between the excitation of the two wave packets in units of the Kepler period, τ_1 , of first wave packet.

portant assumption. Namely, the double ionization signal observed for a HCP delay t_2 depends only on electron-electron interactions before the appearance of the HCP. That is, we neglect energy exchange between the electrons following the HCP. These assumptions are clearly violated at some level.

First, “post-collision interaction” (PCI) between two continuum electrons can result in the re-capture of one electron [50]. The exposure of the atom to a HCP, after a delay t_2 , might promote both electrons into the continuum such that a high double ionization yield would be expected. However, strong PCI following the HCP might result in the recapture of one electron, thereby reducing the double ionization yield.

Second, significant energy exchange between the electrons prior to their exposure to the HCP, should be reflected by a small double ionization yield. However, the HCP might actually reverse the direction of an exiting electron, resulting in a re-collision of the two electrons and the creation of states that ionize in the clearing pulse.

It is worth noting that such “final-state” interactions are a fundamental obstacle to any time-dependent probe of multi-particle dynamics. It is important that the influence of these effects is quantified when using any probe schemes. We use the classical trajectory Monte Carlo simulations to gauge the impact of the final state interactions on our experimental results.

We define a time-dependent variation, $\sigma_{ee} = \sqrt{\frac{\sum_N (V_{ee}^2 - 1/r_0^2)}{N}}$ of the interaction energy $V_{ee} = 1/|\vec{r}_1 - \vec{r}_2|$ relative to the lowest order screening term $1/r_0$, where r_0 is the radius of the outer most electron, and N is the number of trajectories. As noted previously, approximating V_{ee} by $1/r_0$ results in independent motion of two electrons in singly- and doubly-charged Coulomb potentials, respectively. These σ_{ee} specifies the typical deviation of V_{ee} from the independent particle interaction energy, and this quantifies the magnitude of energy exchange between two electrons as a function of time. In Fig. 5.14, σ_{ee} is shown as a function of time for several HCP delays and distinct double Rydberg wave packet configurations. In particular, simulated results are shown for the second electron excitation occurring when the first electron is at either the inner or the outer turning points of its motion for both the $38g23d$ and $38g25d$ initial configurations. For comparison, the expectation values for the radial positions of the two electrons are shown on the same time axis. The instant at which the double Rydberg wave packets are exposed to the 7500V/cm HCP is labeled by vertical lines. Notably, σ_{ee} drops steadily, but not always monotonically after the excitation of the second wave packet. Not surprisingly, the decrease in interaction energy is accompanied by an increase in the difference between the expectation values for the radial locations of the two electrons. The small delayed peaks in σ_{ee} in (a) and (c) show that the second electron does not gain sufficient energy to ionize during the first collision with the first electron, but does ionize when it returns to interact

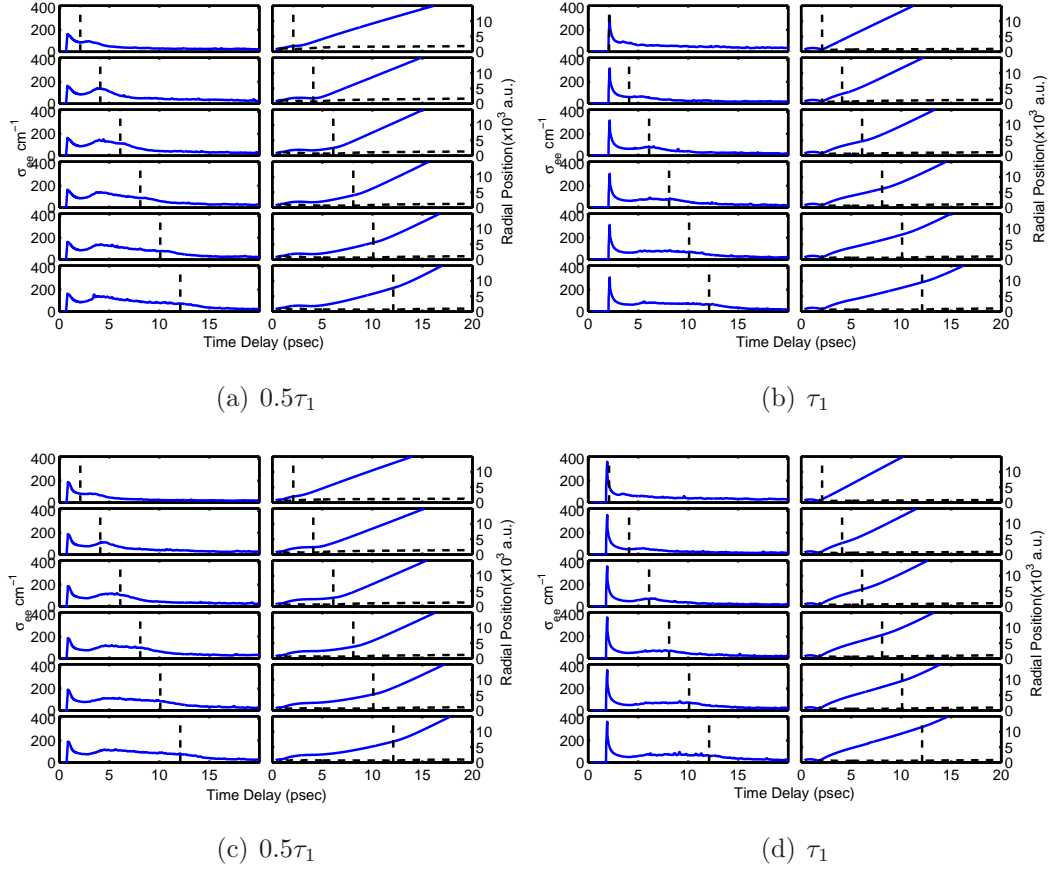


Figure 5.14: Time-dependent variation σ_{ee} (left plot in each pair) and the expectation values of radial position of two electrons (right plot in each pair) as a function time for 38g25d(a)(b) and 38g23d(c)(d), where $\sigma_{ee} = \sqrt{\frac{\sum_N (V_{ee}^2 - 1/r_0^2)}{N}}$. Each curve corresponds to the specific launch time of HCP indicated by vertical dash line. The y axis varies from 0 to 400 cm^{-1} for each left plot. The radial distance varies from 0 to 15000 a.u. for each right plot. The vertical line indicates the instant that the double Rydberg wave packets are exposed to the HCP. In the radial position plots, the blue solid line is for the outer electron which sees a $-1/r$ potential, and the black dashed line is for the inner electron which experiences a $-2/r$ potential.

with the electron a second time.

It is clear from Fig. 5.14 that while the interaction energy does not drop instantly to zero during the HCP, there are no periods of significant energy exchange following the HCP. Indeed, the HCP effectively eliminates further interaction between the two electrons. The reduction in electron interactions is particularly evident in Fig. 5.14 (a) and (c) when the presence of the HCP, prior to the second interaction between electrons, substantially reduces those interactions. Thus, the simulations suggest that the assumption of negligible electron-electron interaction following the HCP probe is reasonable for current experiments.

The simulated double ionization probability vs. t_1 and t_2 , obtained using the experimental conditions, are shown as density plots in Fig. 5.15. The same normalization procedure used for the experimental data is applied and the normalized double ionization probability are shown in Fig. 5.15. The simulated double ionization probabilities for different t_1 are normalized to the double ionization probability for the corresponding simulation when the second wave packet is excited 9.3 psec after the first wave packet.

Several features observed in the experiment are apparent. First, the double ionization yield decreases as a function of time and levels out at large times. Second, oscillations in the double ionization yield are clearly observed. These oscillations are due to the evolution of the ionic wave packets resulting from the first exchange of energy between two electrons (see 5.11 and 5.12.) In the $38g25d$ case, the ionic wave packets produced during this first “hard” collision have an average principle quantum number $N' \sim 32$ with Kepler period ~ 1.2 psec. The ionic wave packets for the $38g23d$ configuration have a characteristic period ~ 1 psec, which is comparable to the duration of the HCP. Therefore, the modulations in the double ionization signal

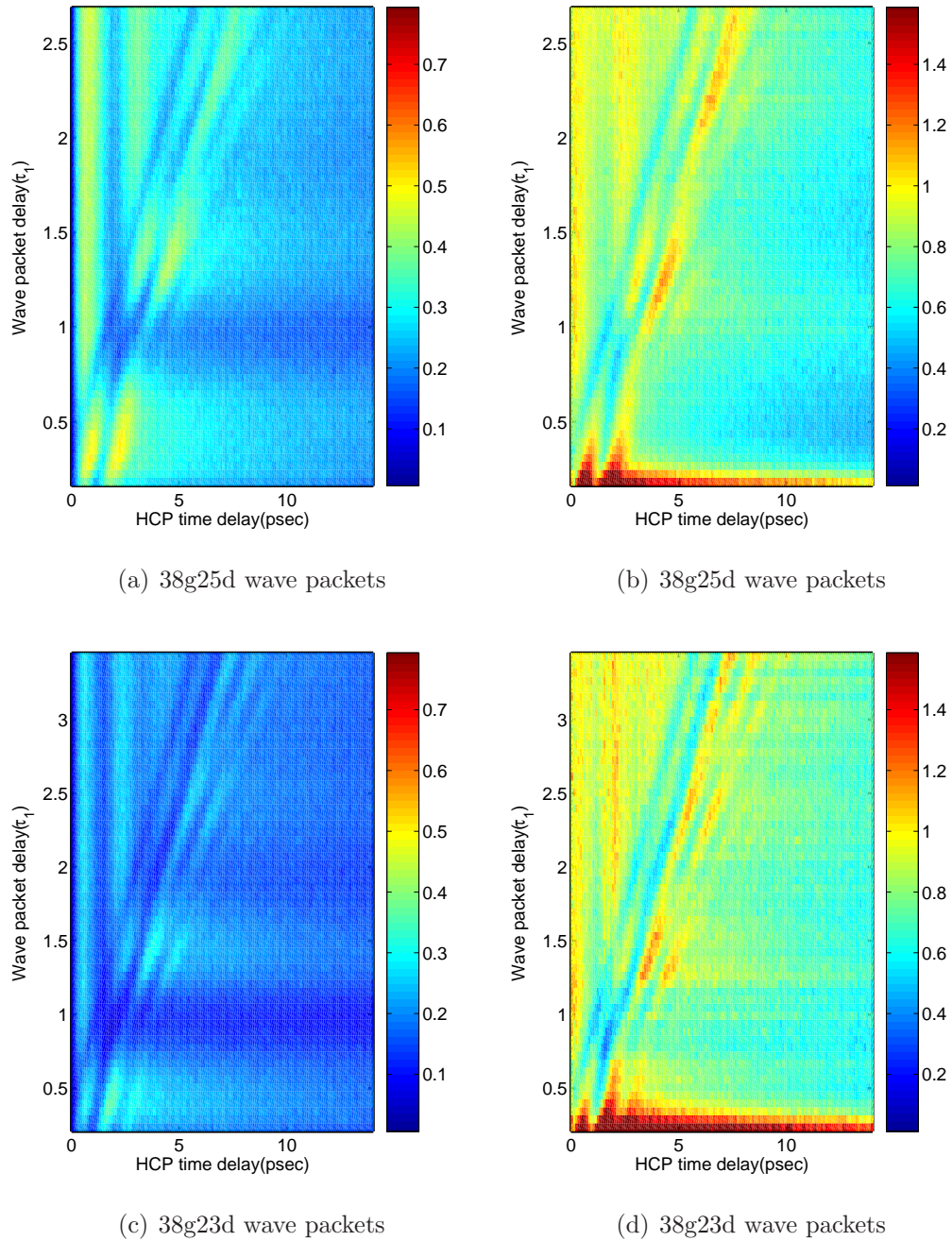


Figure 5.15: Density plots for unnormalized (a,c) and normalized (b,d) HCP double ionization probability of $38g25d$ and $38g23d$ wave packets from classical simulation. Zero delay corresponds to the excitation of the first wave packet.

are more obvious in the $38g25d$ case as compared to the $28g23d$ case.

While some aspects of the classical simulation are in qualitative agreement with the experimental observations, the numerical results fail to quantitatively reproduce the experimental data. Line outs from the density plots of Fig. 5.15 are shown in Fig. 5.16. The background signal levels are consistently higher in simulation than those of the experimental data and the initial rapid signal decrease is absent. Furthermore, the normalized simulated signals consistently show a small minimum during the excitation of the second wave packet. The failure of the classical simulation to provide a quantitative description of the experiments might be attributed to the assumption of perfect ICE. The second electron is assumed to be launched as a perfect ionic wave packet in a pure $Z=2$ Coulomb potential. This is only an approximation, and in experiments some influence from the outer electron is present. A fully quantum or semi-classical treatment of the laser excitation on subsequent dynamics may be required to quantitatively reproduce the data.

5.4 Summary

This chapter presents the first experimental results on the direct probing of time-dependent energy exchange between electrons in a double Rydberg atom. Following the measurement of the ionic radial wave packets as described in chapter 4, the $5d_{5/2}nd$ wave packet was characterized by comparing the double ionization yields with two-channel quantum defect theory calculations. The evolution of the double Rydberg wave packets was probed using a time delayed HCP to influence the double ionization yield, both experimentally and by CTMC. We observe experimentally that the excitation of the second wave packet results in rapid energy exchange between the

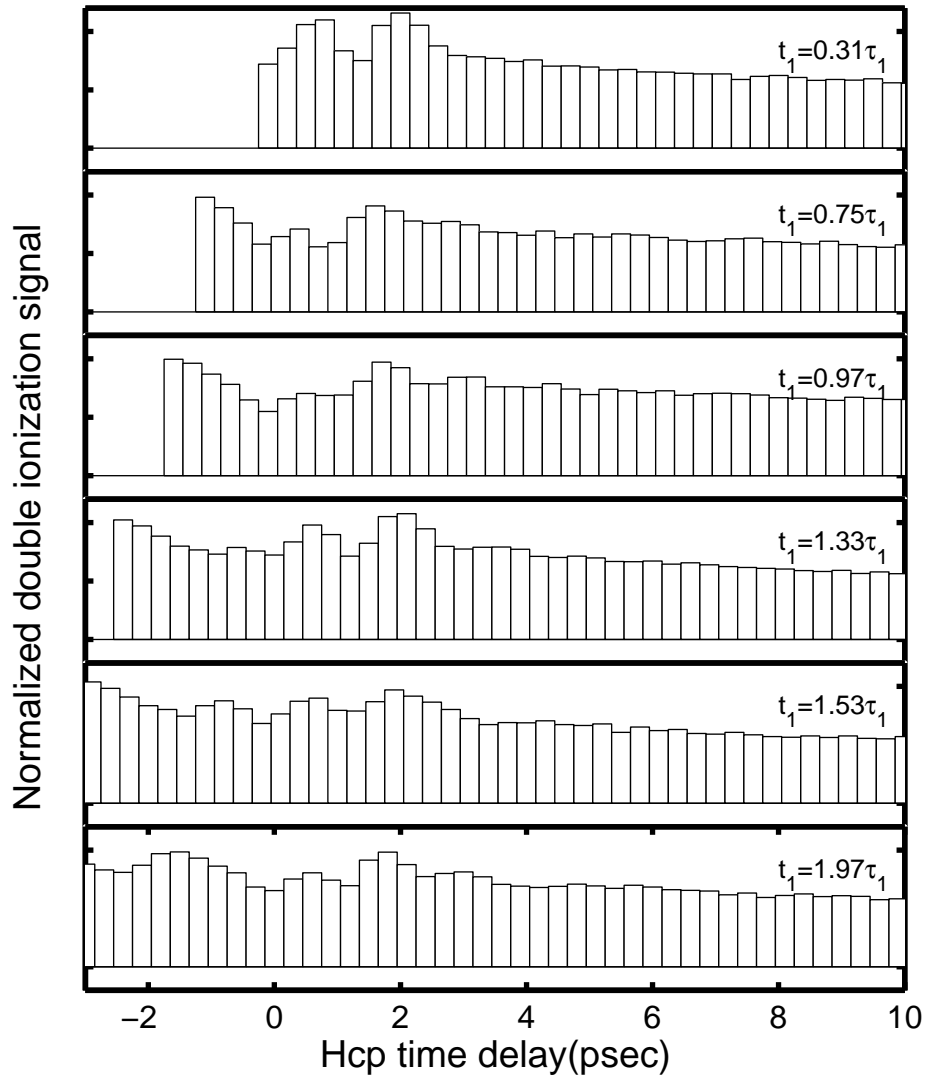


Figure 5.16: The calculated normalized double ionization signal of Ngn double Rydberg wave packets, where $n \sim 25$ and $N \sim 38$, as a function of delay t_2 with respect to the ionic wave packet excitation. Each data set corresponds to a different time delay, t_1 , in terms of the Kepler period of the first wave packet. The simulated data are integrated over (230 fsec) time bins as in the experiment.

two electrons, nearly independent of the initial distance of the initial neutral wave packet. The rate at which energy is redistributed between electrons varies somewhat as the function of time delay between two wave packets, but the temporal resolution of the experiment is insufficient to make a quantitative analysis of the rates. Following autoionization, the HCP probes the evolution of the resulting ionic wave packet. The CTMC qualitatively reproduces some features of the experiment, however it fails to quantitatively reproduce the observed dynamics in this two-electron system.

Chapter 6

Conclusion

This dissertation has described a series of experiments leading to the first direct measurement of time-dependent energy exchange in double Rydberg wave packets (DRWs). Several preliminary experiments paved the way for the primary measurements. The first experiment characterized the field dependence of HCP ionization of ionic Rydberg states. The second experiment explored the time-dependent evolution of Rydberg ion wave packets via HCP ionization and a method for determining the quantum states of these wave packets was demonstrated. Finally, HCP aided double ionization was used as a probe of time-dependent energy exchange in DRWs. The following sections summarize the experiments, highlight their major results, and conclude with suggestions for future work.

6.1 HCP ionization of ionic Rydberg states

Sub-picosecond HCP ionization of ionic Rydberg states was investigated to verify the validity of the impulsive approximation for the ionization of ionic Rydberg states. The measured double ionization yields as a function of the HCP strength for $Ba^+ ng^+$

ions and Ba $6snd$ Rydberg states with approximately the same binding energies were compared and found to be essentially identical within experiment noise. Furthermore, we observed reasonable agreement between the experimental data and the prediction of both in the impulsive ionization model and classical Monte-Carlo simulations. Following these measurements, the HCP impulse delivered to a Rydberg ion can be calibrated using known HCP ionization threshold for neutral Rydberg atoms.

6.2 Ionic Rydberg wave packets

The time-dependent characteristics of Rydberg ion wave packets were examined before implementing the double excited wave packet experiments. The evolution of these ionic wave packets was monitored for the first time using impulsive HCP ionization. The radial beating dephasing, and revivals of the wave packets were observed in analogous fashion to radial wave packets in the neutral Rydberg atoms. Using a complex-phase retrieval method, the constituent states and relative phases between these states were extracted from the time-dependent double ionization probability. These parameters, along with the known Rydberg wave functions are sufficient to completely reconstruct the evolution of the ionic wave packets in both position and momentum space. Accurate characterization of neutral and ionic wave packets is crucial for the interpretation of the double wave packet experiments.

6.3 Time-dependent energy exchange of DRW

After demonstrating a method to characterize ionic Rydberg wave packets, the first direct time-dependent measurement of the dynamics of double Rydberg wave packets was conducted utilizing impulsive HCP ionization both in the laboratory

and in numerical CTMC simulation . Experimentally, energy exchange between the two wave packets is observed almost at the instant of the excitation of ionic wave packets. However, the rate at which autoionization occurs depends on the relative initial positions and velocities of the two wave packets. Following autoionization, the evolution of remaining “ionic” wave packet is reflected in modulations in the HCP aided double ionization yield. This feature is more visible in the CTMC simulations than in the experimental results. The CTMC simulation supports our assumption that significant electron-electron interactions do not occur following the HCP. The elimination of such final states interactions is critical for time-resolved probes of multi-particle dynamics in general.

6.4 Future directions

It is suggested in the experiments described in this dissertation and previous experiments [49, 50] that the energies of two electrons exchange when two electrons are close. Therefore, a possible experiment can be proposed to measure the angular distribution of ionic Rydberg wave packets using HCP. The HCP ionization of Rydberg states corresponds to the momentum distribution of these states, which is not possible to use it solely to measure the angular dependence of Rydberg states unless the Rydberg states are oriented in the static electric field [72]. If we excite the first electron into a wave packet, which has well defined orientation, for example, the quasi-1D Rydberg atom, we can establish a z-axis. One way to generate quasi-1D Rydberg atoms is to excite atoms to a Stark state with the presence of static electric field, then use a HCP or a HCP train to produce a wave packet with a specific orientation [76]. Once this electron is positioned. The ionic Rydberg wave packets can

be prepared using ICE method with the electric field off. The large double ionization signal will be found at where two electrons have large spatial overlap. Thus, a HCP can be used to retrieve the angular variation of ionic wave packets by changing the relative angle between the orientation of quasi-1D wave packet and the polarization of the excitation laser of ionic wave packets.

The 3-body Coulomb system, double Rydberg wave packets, used in this dissertation and previous studies is controlled by changing initial energies of excited wave packets and the relative time delay, phase difference, between two wave packets. However, these systems are constrained to the low initial angular momentum by optical selection rules. The angular momentum dependent dynamics of two-electron system is worth being investigated. One way is utilizing the Stark switching technique [77], which can be applied to the excitation of the first wave packet. Atoms are excited into a given level of a Stark manifold with the presence of an electric field. The field is then reduced adiabatically to zero. Therefore, the excited state now only has the character of a single angular momentum eigenstate. Another laser pulse further promotes this electron to a Rydberg wave packet, which will have higher angular momentum characters. Last, the second Rydberg wave packet can be produced by ICE method similar to the experiments described here. However, this proposal may require finding a new excitation scheme instead of the one used in this dissertation for Ba atoms. Another approach relies on the oscillation of the angular momentum of Stark wave packets. This oscillation starts from the initial value determined by laser excitation, to the maximum value $l = n - 1$ and back to 0. The period of the oscillation is $\tau_s = 2\pi/3Fn$, where F is the static field and n is the principal quantum number. Therefore, the relative delay between the excitation of two wave packets corresponds to the difference of angular momenta. Consequently, the effect of angular momenta

of two electrons can be studied [12].

In this dissertation, CTMC simulations are used to aid our understanding of energy exchange in the 3-body Coulomb system. Though, some features of the data are reproduced by this classical simulation, more work will be required to achieve quantitative agreement between the experimental data and simulations. Quantum or semi-classical techniques to treat the excitation and evolution of the double Rydberg wave packets may be needed to further the understanding of such systems.

Appendix A

Runge-lenz vector

The Runge-lenz vector \vec{M} is a constant for a particle moving under the central force, $F = mk/r$. It is defined as

$$\vec{M} = \vec{p} \times \vec{L} - mk\hat{r}. \quad (\text{A.1})$$

where \vec{p} is the momentum; \vec{L} is angular momentum; m is the mass of the particle; k is the parameter to describe the strength of central force; \hat{r} is unit position vector, i.e., $\hat{r} = \frac{\vec{r}}{r}$ where r is the magnitude of \vec{r} . Here we follow the notation used in Ref. [75]. The Runge-lenz vector defines the shape and orientation of the orbit of particle. This can be seen by looking $\vec{M} \cdot \vec{r}$

$$\vec{M} \cdot \vec{r} = \vec{r} \cdot (\vec{p} \times \vec{L}) - mkr \quad (\text{A.2})$$

$$= (\vec{r} \times \vec{p}) \cdot \vec{L} - mkr \quad (\text{A.3})$$

$$= L^2 - mkr \quad (\text{A.4})$$

$$= Mr \cos(\theta), \quad (\text{A.5})$$

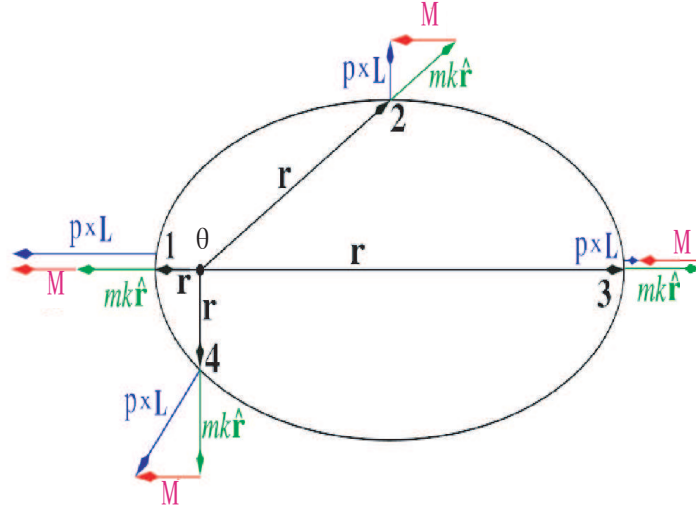


Figure A.1: Schematic diagram of Runge-Lenz vector at four different points on a ellipse orbit(Adapted from Ref. [78]).

where we use the relationship $\vec{A} \cdot (\vec{B} \times \vec{C}) = (\vec{A} \times \vec{B}) \cdot \vec{C}$ and the θ is the angle between \vec{M} and \vec{r} . Therefore, we can derive

$$\frac{1}{r} = \frac{mk}{L^2} \left(1 + \frac{M}{mk} \cos(\theta)\right). \quad (\text{A.6})$$

By comparing with the equation of motion in the central force potential [75]

$$\frac{1}{r} = \frac{mk}{L^2} (1 + \epsilon \cos(\theta)) \quad (\text{A.7})$$

the eccentricity of the orbit is then

$$\epsilon = \frac{M}{mk}. \quad (\text{A.8})$$

Furthermore, the magnitude of \vec{M} can be written in terms of the energy, E , and the angular momentum, L , of the particle,

$$M = mk\sqrt{1 + \frac{2EL^2}{mk^2}}. \quad (\text{A.9})$$

Consider an electron is moving in a Coulomb potential, $-Z/r$. If atomic units are used, the magnitude of Runge-Lenz vector is then

$$M = Z\sqrt{1 + \frac{2EL^2}{Z^2}} \quad (\text{A.10})$$

$$= Z\sqrt{1 - \frac{2L^2(Z^2/2n^2)}{Z^2}} \quad (\text{A.11})$$

$$= Z\sqrt{1 - \frac{L^2}{n^2}} \quad (\text{A.12})$$

where the energy $E = -Z^2/2n^2$ and $k = Z$ are used. n is the principle quantum number and $L^2 = l(l+1)$.

Bibliography

- [1] G. Tanner, K. Richter, J.-M. Rost, *Rev. Mod. Phys.* **72**,497 (2000).
- [2] K. Richter, G. Tanner, D. Wintgen, *Phys. Rev. A.* **48**,4182 (1993).
- [3] W. Huang, U. Eichmann, W. Sandner, *Phys. Rev. A.* **59**,2744 (1999).
- [4] J. A. West, Z. D. Gaeta, C. R. Stroud, Jr., *Phys. Rev. A.* **58**, 186 (1998).
- [5] M. Kalinski, J. H. Eberly, J. A. West, C. R. Stroud, Jr., *Phys. Rev. A.* **67**, 032503 (2003).
- [6] R. P. Madden, K. Codling *Phys. Rev. Lett.* **10**, 516(1963).
- [7] W. E. Cooke, R. M. Jopson, L. A. Bloomfield, R. R. Freeman, J. Bokor, *AIP Conf. Proc.*, **vol.119**, 91 1984; R. van Leeuwen, W. Ubachs, P. Camus, W. Hogervorst, *Phys. Rev. A* **54**, R17(1996); R. R. Jones, Panming Fu, T. F. Gallagher, *Phys. Rev. A* **44**, 4265 (1991); U. Eichmann, V. Lange, W. Sandner, *Phys. Rev. Lett.* **68**, 21 (1992).
- [8] L. A. Bloomfield, R. R. Freeman, W. E. Cooke, J. Bokor, *Phys. Rev. Lett.* **53**,2234 (1984);R. R. Jones, T. F. Gallagher, *Phys. Rev. A* **42**, 2655 (1990);P. Camus, T. F. Gallagher, J.-M. Lecomte, P. Pillet, L. Pruvost, J. Boulmer, *Phys. Rev. Lett.*

- 62**, 2365 (1989); U. Eichmann, V. Lange, W. Sandner, *Phys. Rev. Lett.* **64**, 274 (1990).
- [9] M. J. Seaton, *Rep. Prog. Phys.*, **46**, 167, (1983); U. Fano, *Phys. Rev. A* **2**, 353 (1970); U. Fano, *J. Phys. B* **7**, L401 (1974). W. E. Cooke and C. L. Cromer, *Phys. Rev. A* **32** 2725 (1985); P. Camus, P. Pillet, J. Boulmer, *AIP Conf. Proc.*, vol. **146**, 480 (1986); J. Boulmer, P. Camus, P. Pillet, *J. Opt. Soc. Am. B* **4**, 805 (1987).
- [10] D. W. Schumacher, B. J. Lyons, T. F. Gallagher, *Phys. Rev. Lett.* **78**, 4359 (1997); R. van Leeuwen, K. Vijayalakshmi, R. R. Jones, *Phys. Rev. A* **63**, 033403 (2001); H. N. Ereifej, J. G. Story, *Phys. Rev. A* **62**, 023404 (2000); *Phys. Rev. A* **62**, 033405 (2000); J. G. Story, H. N. Ereifej, *Phys. Rev. Lett.* **86**, 612 (2001).
- [11] R. R. Jones and L. D. Noordam, *Adv. At. Mol. Opt. Phys.* **38**, 1 (1997); T. C. Weinacht, J. Ahn, P. H. Bucksbaum, *Nature* **397**, 233 (1999); L. D. Noordam and R. R. Jones, *J. Mod. Opt.* **44** 2515 (1997).
- [12] R. R. Jones, NSF proposal
- [13] R. R. Jones *Proceedings ICPEAC XXIV*, World Scientific (2005)
- [14] J. R. Rydberg *phil. Mag* **29**, 331, (1890).
- [15] T. F. Gallagher, *Rydberg Atoms*, 1st ed., Cambridge University Press, Cambridge, (1994) and references therein.
- [16] M. Drescher, M. Hentschel, R. Kienberger, M. Uiberacher, V. Yakovlev, A. Scrinzi *et. al. Nature* **419** 803 (2002); Olga Smirnova, Vladislav S. Yakovlev, and Armin

- Scrinzi, *Phys. Rev. Lett.* **91** 253001(2003);S. X. Hu and L. A. Collins *Phys. Rev. Lett.* **96** 073004(2006);Olga Smirnova, Sergei Patchkovskii, and Michael Spanner,*Phys. Rev. Lett.* **98** 123001(2007);Toru Morishita,Shinichi Watanabe, and C. D. Lin *Phys. Rev. Lett.* **98** 083003(2007).
- [17] E.Schrodinger, *Naturwissenschaften*,**2**, 664(1926).
- [18] T.F.Gallgher *Physica Scripta*, **76**, C145 (2007).
- [19] D. Strickland and G. Mourou,*Opt. Commum.* **56**,219(1985), G.Mourou, C.P.J. Barty and M.D.Perry, *Phys. Today* **51**,22(1998).
- [20] Taken from <http://en.wikipedia.org/>.
- [21] W.T. Silfvast, *Laser Fundamentals*, Cambridge University Press, New York,(1996).
- [22] Model MTS Mini Ti:Sapphire laser Kit instruction manual, Kapteyn-Murnane Laboratories Inc.
- [23] M.B. Campbell,Ph.D Thesis,University of Virginia(2000).
- [24] O.E.Martinez, J.P.Gordon and R.L.Fork, *J. Op. Soc. Amer. A* **1**,1003(1984).
- [25] O.E.Martinez, *IEEE J. Quantum Electron* **QE-23**,59(1987).
- [26] J.G.Zeibel,Ph.D Thesis,University of Virginia(2003).
- [27] S.N.Pisharody,Ph.D Thesis,University of Virginia(2003).
- [28] J.-C. Diels and W. Rudolph, "Ultrashort Laser Pulse Phenomena," Academic Press, San Diego, CA (1996).

- [29] M. Jeremy, Ph.D Thesis, University of Virginia (2007)
- [30] J. Parker, and C.R. Stroud Jr., *Phys. Rev. Lett.* **56**, 716 (1986).
- [31] T. W. Hansch, *Applied Optics* **11**, 4 (1972).
- [32] M. G. Littman, *Opt. Lett.* **3**, 138 (1978).
- [33] John H. Moore, Christopher C. Davis, Michael A. Coplan, Sandra C. Greer, *Building Scientific Apparatus*, 3rd edition, Westview Press.
- [34] D. You, R.R. Jones, P.H. Bucksbaum, and D.R. Dykaar, *Opt. Lett.* **18**, 290 (1993).
- [35] R.R. Jones, D. You, and P.H. Bucksbaum, *Phys. Rev. Lett.* **70**, 1236 (1993).
- [36] C.O. Reinhold, M. Melles, H. Shao, and J. Burgdörfer, *J. Phys. B* **26**, L659 (1993); C.O. Reinhold, H. Shao, and J. Burgdörfer, *J. Phys. B* **27**, L469 (1994).
- [37] C.D. Schwieters and J.B. Delos, *Phys. Rev. A* **51**, 1023 (1995); G. Alber and O. Zobay, *Phys. Rev. A* **59**, R3174 (1999); O. Zobay and G. Alber, *Phys. Rev. A* **60**, 1314 (1999); K.J. LaGattuta and P.B. Lerner, *Phys. Rev. A* **49**, R1547, (1994); K.J. LaGattuta, *Phys. Rev. A* **53**, 1762 (1996); P. Krstic and Y. Hahn, *Phys. Rev. A* **50**, 4629 (1994); C. Rangan, K.J. Schafer, and A.R.P. Rau, *Phys. Rev. A* **61**, 053410 (2000).
- [38] A. Bugacov, B. Piraux, M. Pont, and R. Shakeshaft, *Phys. Rev. A* **51**, 1490 (1995); A. Bugacov, B. Piraux, M. Pont, and R. Shakeshaft, *Phys. Rev. A* **51**, 4877 (1995).
- [39] F. Robicheaux, *Phys. Rev. A* **56**, R3358 (1997); F. Robicheaux, *Phys. Rev. A* **60**, 431 (1999).

- [40] R.R. Jones, N.E. Tielking, D. You, C. Raman, and P.H. Bucksbaum, *Phys. Rev. A* **51** R2687 (1995); N.E. Tielking and R.R. Jones, *Phys. Rev. A* **52**, 1371 (1995); R.R. Jones and P.H. Bucksbaum, *Comments At. Mol. Phys.* **30**, 347 (1995); T.J. Bensity, G. Haeffler, and R.R. Jones, *Phys. Rev. Lett.* **79**, 2018 (1997).
- [41] N.E. Tielking, T.J. Bensity, and R.R. Jones, *Phys. Rev. A* **51**, 3370 (1995).
- [42] M.T. Frey, F.B. Dunning, C.O. Reinhold, and J. Burgdörfer, *Phys. Rev. A* **53**, R2929 (1996); B.E. Tannian, R.A. Popple, F.B. Dunning, S. Yoshida, C.O. Reinhold, and J. Burgdörfer, *J. Phys. B* **31** L455 (1998); S. Yoshida, C.O. Reinhold, J. Burgdörfer, B.E. Tannian, R.A. Popple, and F.B. Dunning, *Phys. Rev. A* **58**, 2229 (1998).
- [43] C. Wesdorp, F. Robicheaux, and L.D. Noordam, *Phys. Rev. Lett.* **87**, 083001 (2001); A. Wetzels, A. Gürtler, L.D. Noordam, F. Robicheaux, C. Dinu, H.G. Muller, M.J.J. Vrakking, and W.J. van der Zande, *Phys. Rev. Lett.* **89**, 273003 (2002).
- [44] C. Raman, C.W.S. Conover, C.I. Sukenik, and P.H. Bucksbaum, *Phys. Rev. Lett.* **76**, 2436 (1996); C. Raman, T.C. Weinacht, and P.H. Bucksbaum, *Phys. Rev. A* **55**, R3995 (1997); J. Ahn, D.N. Hutchinson, C. Rangan, and P.H. Bucksbaum, *Phys. Rev. Lett.* **86**, 1179 (2001); C. Rangan and P.H. Bucksbaum, *Phys. Rev. A* **64**, 033417 (2001).
- [45] R.R. Jones, *Phys. Rev. Lett* **76**, 3927 (1996); J.G. Zeibel and R.R. Jones, *Phys. Rev. A* **68**, 023410 (2003).

- [46] . M.B. Campbell, T.J. Bensity, and R.R. Jones, *Phys. Rev. A* **58**, 514 (1998);
M.B. Campbell, T.J. Bensity, and R.R. Jones, *Phys. Rev. A* **59**, R4117 (1999);
T.J. Bensity, M.B. Campbell, and R.R. Jones, *Phys. Rev. Lett.* **81**, 3112 (1998).
- [47] C.O. Reinhold, J. Burgdörfer, *Phys. Rev. A* **54** R33 (1996); D.G. Arbo, C.O. Reinhold, J. Burgdörfer, *Phys. Rev. A* **67** 063401 (2003).
- [48] H. Wen, S.N. Pisharody, J. M. Murray, and P.H. Bucksbaum, *Phys. Rev. A*, **73**, 052504 (2006); J.M. Murray, S.N. Pisharody, H. Wen, C. Rangan, and P.H. Bucksbaum, *Phys. Rev. A* **74**, 043402 (2006); J.M. Murray, S.N. Pisharody, H. Wen, and P.H. Bucksbaum, *Phys. Rev. A*, **71**, 023408 (2005); H.. Wen, S. N. Pisharody, J. M. Murray, P. H. Bucksbaum, *Phys. Rev. A*, **71**, 013407 (2005).
- [49] S.N. Pisharody and R.R. Jones, *Science* **303** 813 (2004);
- [50] S.N. Pisharody and R.R. Jones, *Phys. Rev. Lett* **91**, 203002 (2003).
- [51] J. Bromage and C.R. Stroud, *Phys. Rev. Lett.* **83**, 4963 (1999).
- [52] A. Rice, Y. Jin, X. F. Ma, X.-C. Zhang, D. Bliss, J. Larkin, and M. Alexander, *Appl. Phys. Lett.* **64**, 1324 (1994);
- [53] Adapted from the material of "Terahertz technology" short class, CELO, Baltimore ,(2007).
- [54] P. H. Bucksbaum, "Wave packets and Half-cycle Pulses", in *Wavepackets*, ed. by J. Yaezell, New York: John Wiley (1999).
- [55] Thomas Bensity, Ph.D Thesis, University of Virginia (1998)
- [56] J.G. Zeibel and R. R. Jones, *Phys. Rev. A* **68**, 023410 (2003).

- [57] R.R. Jones, and M.B. Campbell, *Phys. Rev. A* **61**, 013403 (1999).
- [58] J.A. Yeazell, M.Mallalieu, J. Parker and C.R. Stroud *Phys. Rev. A*, **40**, 5040(1989);J.A. Yeazell, M.Mallalieu and C.R. Stroud *Phys. Rev. Lett.*, **64**,2007(1990).
- [59] Xin Chen and John A. Yeazell,*Phys. Rev. A* **56**,2316(1997).
- [60] W. E. Cooke and C. L. Cromer, *Phys. Rev. A* **32**, 2725 (1985).
- [61] X. Wang and W. E. Cooke, *Phys. Rev. Lett.* **67**, 976 (1991); *Phys. Rev. A* **46**, 4347 (1992).
- [62] J. E. Thoma and R. R. Jones,*Phys. Rev. Lett.* **83**, 516 (1999).
- [63] S.N. Pisharody and R.R. Jones *Phys. Rev. A* ,**65**, 033418 (2002).
- [64] J.G. Dtory, D.I Duncan and T.F. gallagher, *Phys. Rev. Lett*, **71** 3431(1003); R. R. Jones *Phys. Rev. A*,**57**,446(1998).
- [65] H. Stapelfeldt, D. G. Papaioannou, L. D. Noordam, T. F. Gallagher, *Phys. Rev.Lett.*, **67**, 3223 (1991);R. R. Jones, P. H. Bucksbaum, *Phys. Rev. Lett.*, **67**, 3215 (1991); D. A. Tate, T. F. Gallagher, *Phys. Rev. A*, **58**, 3058 (1998); H. Maeda, W. Li, T. F. Gallagher, *Phys. Rev. Lett.*, **85**, 5078 (2000); H. Maeda,T. F. Gallagher, *Phys. Rev. A*, **65**, 053405 (2002).
- [66] F. Robicheaux and R. C. Forrey *J. Phys. B*, **38** (2005)
- [67] N. Bohr, *Philos. Mag.*, **26**, 476 (1913); I. Langmuir, *Phys. Rev.*, **17**, 339 (1921); J. H. Van Vleck,*Philos. Mag.*,**44**, 842 (1922); J. G. Leopold, I. C. Percival, *J. Phys. B* , **13**, 1037 (1980);W. Huang, U. Eichmann, W. Sandner, *Phys. Rev. A.*,

- 59**, 2744 (1999); J. A. West, Z. D. Gaeta, C. R. Stroud, Jr., *Phys. Rev. A.*, **58**, 186 (1998); M. Kalinski, J. H. Eberly, J. A. West, C. R. Stroud, Jr., *Phys. Rev. A.*, **67**, 032503 (2003); S. Watanabe, C. D. Lin, *Phys. Rev. A.*, **34**, 823 (1986); J. M. Feagin, J. S. Briggs, *Phys. Rev. A.*, **37**, 4599 (1988); G. Handke, M. Draeger, H. Friedrich, *Physica A* **197**, 113 (1993).
- [68] W. E. Cooke, T. F. Gallagher, S. A. Edelstein, and R. M. Hill, *Phys. Rev. Lett.*, **40**, 178 (1978).
- [69] X. Zhang and R. R. Jones *Phys. Rev. A* **73** 035401 (2006).
- [70] W. H. Press, S. A. Teukolsky, W. T. Vetterling, B. P. Flannery, *Numerical Recipes in C: The Art of Scientific Computing, 2nd ed.*, Cambridge University Press, New York, (1995).
- [71] J. G. Zeibel and R. R. Jones *Phys. Rev. Lett.* **89**, 093204 (2002).
- [72] R. R. Jones, N. E. Tielking, D. You, C. Raman, and P. H. Bucksbaum *Phys. Rev. A*, **51**, R2687 (1995).
- [73] H. A. Bethe and E. E. Salpeter *Springer* 1 edition (April 30, 1977)
- [74] T. P. Hezel, C. E. Burkhardt, M. Ciocca, and J. J. Leventhal, *Am. J. Phys.*, **60**, 324 (1992); E. Luc-Koenig and A. Bachelier, *J. Phys. B*, **13**, 1743 (1980); L. D. Landau and E. M. Lifshitz, *Quantum Mechanics (Non relativistic Theory)*, 3rd ed., Pergamon Press, Oxford, (1976).
- [75] H. Goldstein, *classical mechanics* Addison-Wesley Press, Cambridge, (1950)
- [76] W. Zhao, J. J. Mestayer, J. C. Lancaster, F. B. Dunning, C. O. Reinhold, S. Yoshida, and J. Burgdorfer, *Phys. Rev. Lett.*, **95**, 163007 (2005).

[77] R. R. Jones and T. F. Gallagher, *Phys. Rev. A*, **38**, 2846 (1988).

[78] Taken from <http://en.wikipedia.org/>